UNIVERSITY OF OKLAHOMA

GRADUATE COLLEGE

DISCOVERY AND CLASSIFICATION OF NEW CIRCUMSTELLAR DISK CANDIDATES FROM THE ALLWISE CATALOG WITH DISK DETECTIVE

A DISSERTATION

SUBMITTED TO THE GRADUATE FACULTY

in partial fulfillment of the requirements for the

Degree of

DOCTOR OF PHILOSOPHY

By

Steven M. Silverberg
Norman, Oklahoma
2019

DISCOVERY AND CLASSIFICATION OF NEW CIRCUMSTELLAR DISK CANDIDATES FROM THE ALLWISE CATALOG WITH DISK DETECTIVE

A DISSERTATION APPROVED FOR THE
HOMER L. DODGE DEPARTMENT OF PHYSICS AND ASTRONOMY

BY

Dr. John Wisniewski, Chair

Dr. Marc Kuchner

Dr. Mukremim Kilic

Dr. Bruce Mason

Dr. Charles Rice

Acknowledgements

There are many people without whom this dissertation could not have been achieved. My heartfelt gratitude goes to them.

First, to Dr. John Wisniewski: thank you for mentioning M dwarfs in your research presentation my first month at OU, thank you for coming by my office and asking if I wanted to work at NASA for a summer, and thank you for having thoughts on next steps every time I came to you with a new result or conundrum. To Dr. Marc Kuchner: thank you for taking me on for a summer to start, thank you for the questions that bred more questions, and thank you for the patience and commentary along the way.

Thank you to my committee and my department for allowing me the opportunity to achieve this work.

Thank you to Evan Rich, Kyra Dame, Mike Malatesta, Kellen Lawson, and all of my fellow graduate students, for their company on sleepless nights when I needed to be awake with a telescope and they did not; for their advice on how to attack specific problems; and for their friendship.

Thank you to Jessica, for being by my side from here on out.

Thank you to my family: Dad, for giving me your copy of H.A. Rey's "The Stars" when I was five; Mom, for introducing me to Robert A. Heinlein and "Star Trek" and further nurturing my love of exploring the stars; Geeg, for my first telescope; and Sarah, for enjoying space as much as I do, helping me get back on track when I needed to, and being someone I can talk to for three hours at the drop of a hat with no prompting.

Thank you to the instrument and telescope support staff who helped me collect the data presented here: Sean Points, Todd Henry, Russet McMillan, and the support staff at Palomar, Las Campañas, CTIO, APO, and IRTF.

The work contained herein would not have been accomplished without the advice, support, and input of several colleagues and collaborators along the way: Alissa Bans, John Debes, Jonathan Gagné, Shambo Bhattacharjee, Scott Kenyon, Christoph Baranec, Reed Riddle, Nicholas Law, Johanna Teske, and Kellen Lawson. Their contributions were invaluable to this work.

Finally, and most importantly, a heartfelt thanks to the thousands of people who have taken the time to classify objects on DiskDetective.org. In particular, I acknowledge the invaluable contributions of Hugo A. Durantini Luca, Milton K.D. Bosch, Tadeas Cernohaus, Katharina Doll, Michiharu Hyogo, Lily Lau, Joseph R. Biggs, Emily Burns-Kaurin, Alexandru Enachioaie, Philip Griffith, Sr., Johanna J.S. Finnemann, Joshua Hamilton, and Fernanda Piñiero. Without the more than three million classifications made by citizen scientists on the Disk Detective website, quite literally none of the science presented in this paper would have happened. This dissertation is a testament to their efforts on this project.

Table of Contents

List of Tables

List of Figures

Abstract

In its five years since launch, DiskDetective.org has led to many new discoveries in the field of circumstellar disks. In my dissertation, I present two major emphases of the project: statistical characterization of infrared excess sources from AllWISE, and identification of unexpected populations of circumstellar disk. We show that at most 7.9% of all WISE-detected infrared excesses are primordial or debris disks, and find that some published excess searches have false positive rates greater than 70%. We present WISEA J080822.18-644357.3, an M5 member of the 45-Myr Carina association, that hosts a disk with an unusually strong excess for its age. We use J0808 as the prototypical example of "Peter Pan" disks, long-lived primordial disks around mid-M or later stars. We identify two new Peter Pan disk candidate systems, each an apparent visual double with WISE excess after both stellar components are accounted for. In follow-up observations of J0808, we find accretion rates of $10^{-12} - 10^{-10} M_{\odot}$/yr, variable on 24-hour timescales, based on near-IR spectroscopy. We also note flare activity and star-disk interactions in nine nights of ground-based high-cadence optical photometry, and one month of high-cadence optical photometry from TESS. Using these characteristics, we explore possible origin scenarios for Peter Pan disks, including longer lives for primordial disks around mid-M stars than previously thought, and discuss methods of testing their validity. If Peter Pan disks are shown to be long-lived primordial disks, and a typical phenomenon around mid-M stars, the timescale for planet formation around these stars would also be greatly increased, affecting our expectations for planet yields and UV input onto the newly formed planets. Such disks would also potentially explain the near-circular resonant orbits of the TRAPPIST-1 system.

Chapter 1

Introduction

All-sky surveys at mid-infrared (IR) wavelengths revolutionized the study of planetary system formation by identifying populations of young and main-sequence stars with excess infrared radiation. These infrared excesses indicate the presence of dusty circumstellar disks, which serve as signposts for planet formation and planetary system evolution (e.g. Kenyon & Bromley, 2002). Circumstellar disk systems have provided valuable insights into the nature of planet formation (e.g. Wyatt & Jackson, 2016) and the properties of present-day planetary systems (e.g. Nesvold & Kuchner, 2015; Tabeshian & Wiegert, 2017). They also indicate systems to be targeted in searches for extrasolar planets; many exoplanets identified via direct imaging are in systems that also include debris disks, such as β Pictoris b (Lagrange et al., 2010), a gas giant in orbit around a known disk host (Smith & Terrile, 1984), and the planetary system (Marois et al., 2008) around known disk host HR 8799 (Su et al., 2009).

The first debris disks were identified from the *IRAS* all-sky survey (Aumann et al., 1984), which surveyed the full sky at 12, 25, 60, and 100 μm. This search yielded a large sample of protoplanetary and debris disks, and allowed for the first statistical studies of disk occurrence (Strom et al., 1989). The AKARI mission later surveyed the full sky at 9 and 18 μm with improved sensitivity over *IRAS*, and itself found a sizable collection of disks (Ishihara et al., 2010). Additional disk discoveries came from pointed surveys with *Spitzer* (e.g. Carpenter et al., 2009). However, many disks, including some of the most well-studied (e.g. Fomalhaut, TW Hydra, AU Mic) are isolated on the sky. As such, a full-sky survey with increased sensitivity is necessary to identify as many disks as possible.

The *Wide-field Infrared Survey Explorer* (WISE) surveyed the full sky in four bandpasses, centered on 3.4, 4.6, 12, and 22 μm (bands W1, W2, W3, and W4), with an $\sim$ 80-fold gain in sensitivity over AKARI (Wright et al., 2010). The AllWISE catalog (Cutri & et al., 2013) combined data from both the WISE cryogenic mission and its first post-cryogenic mission, NEOWISE, identifying over 747 million sources across the sky.

Many teams have used WISE data to identify stars that exhibit infrared excess, indicative of new debris and YSO disks. McDonald et al. (2012) cross-matched WISE with *Hipparcos* and other catalogs to identify more than 86,000 potential excess sources. Kennedy & Wyatt (2013), Wu et al. (2013), and Patel et al. (2014) each performed more detailed searches in the WISE cross-match with *Hipparcos*, respectively identifying 6, 70, and 108 disk candidates. Cotten & Song (2016) assembled a list of WISE debris disks by combing the literature for other disks, and inspecting targets in the cross-match between WISE and *Tycho*. Patel et al. (2017) evaluated candidates from *Hipparcos* based on their unblurred coadded images from unWISE (Lang, 2014).

Confusion and contamination limit every search for disks with WISE (e.g. Kennedy & Wyatt, 2012). The point spread function (PSF) for the W4 band has a full-width at half-maximum of $12''$, allowing emission from multiple point sources within that radius to blend and produce a false-positive excess detection. Additionally, the color locus of debris disks overlaps the color loci of several other astronomical phenomena, including background galaxies and stars embedded in the interstellar medium (Koenig et al., 2012). Color cuts based solely on the recorded photometry at different wavelengths can provide a first stage of vetting (ensuring that the system in question exhibits an excess), but the resulting catalogs are filled with false-positive disk identifications (Kennedy & Wyatt, 2012)

because such cuts naturally include these similarly-colored phenomena. To eliminate these false-positives, objects must be examined in visible and near-infrared images along with WISE images. Most published searches have utilized visual inspection of the WISE images (e.g. Debes et al., 2012; Kennedy & Wyatt, 2012; Wu et al., 2013; Cruz-Saenz de Miera et al., 2014; Patel et al., 2014) to address these issues. However, these surveys have primarily focused on targets cross-matched with optical-magnitude-limited surveys, limiting the number of potential targets to only those which were bright enough at visible wavelengths to be observed by *Hipparcos* and *Tycho*. This ignores a sizable swath of both distant targets and nearby targets with high extinction for potential evaluation, and biases their selection to bluer early-type stars, which are more intrinsically bright at optical wavelengths than later-type stars.

1.1 Evolution of Protoplanetary Disks

Disks related to planetary system formation and evolution fall into two broad categories, within which there are several sub-categories. Primordial disks are gas-rich disks around young stellar objects (YSOs), while debris disks are dusty, generally gas-poor disks made of the material from collisions and outgassing of second-generation material. Objects are generally classified as one or the other based on their fractional infrared luminosity ($L_{\rm ir}/L_\star$), the fraction of their host star's light which is re-processed and re-radiated by the disk material. Disks with $L_{\rm ir}/L_\star < 10^{-3}$ are generally classified as debris disks, while brighter disks are classified as primordial (Williams & Cieza, 2011).

In the generally-accepted model of primordial disk evolution, stars begin as young stellar objects (YSOs) with optically-thick, gas-rich protoplanetary disks, single-component disks that radiate from near-IR to sub-millimeter wavelengths

(Williams & Cieza, 2011, and references therein). These disks form from the same molecular cloud as their host star. Transitional disks, disks with inner clearings or radial gaps in the gas and dust that otherwise resemble protoplanetary disks, begin to appear at similar ages to protoplanetary disks, and can last to age ~ 10 Myr (Williams & Cieza, 2011). There are multiple potential explanations for this variety of disk, including dynamical effects of an orbiting massive planet (Kim et al., 2009), photoevaporation from the central star (Williams & Cieza, 2011), dust grain growth (e.g. Andrews & Williams, 2005; McClure et al., 2010), and potentially photoelectric instability (Richert et al., 2018). Observations with the *Spitzer* space telescope have also identified a class of "pre-transitional" disks around T Tauri stars (Espaillat et al., 2007, 2010). These systems exhibit mid-IR flux deficits, but substantial excess at near-IR (2-5 μm) wavelengths, and at far-IR ($> 20\mu$m) and sub-millimeter wavelengths. These disks generally appear at ages 5-8 Myr, but have appeared at younger ages in Taurus.

Debris disks are the expected final form of these disks, made up of rock and second-generation dust produced by collisions and outgassing of planetesimals after primordial gas has photoevaporated and primordial small grains have been removed by radiation pressure and Poynting-Robertson drag. Unlike their protoplanetary predecessors, which appear to be continuous when resolved and have spectral energy distributions (SEDs) that can be treated with power-law prescriptions, debris disk systems generally consist of one or more discrete rings, as seen in images of the resolved disk around Fomalhaut (Kalas et al., 2008). The SEDs of unresolved disks are generally fit well by one or more blackbody functions. These systems can be thought of as consisting of "warm" and "cold" disks depending on the blackbody temperature, which could potentially be analogous to our asteroid belt and Kuiper belt, respectively (e.g. Ballering et al., 2013; Chen et al., 2014).

The shape of the SEDs of disk systems can be used to classify the system as a whole. The slope of an infrared power law describing the disk is used to classify YSOs: Class I YSOs exhibit power-law SEDs from near-IR to sub-mm wavelength with a positive spectral index $\alpha_{\rm IR} > -0.3$, while Class II YSOs have a spectral index $-1.6 < \alpha_{\rm IR} < -0.3$, and Class III YSOs have $\alpha_{\rm IR} < -1.6$ (Lada, 1987). As expected given the plethora of potential causes, transitional disks exhibit a variety of SED structures, as seen in Figure 1.1. Debris disks, meanwhile, can be most simply characterized as a combination of one or two blackbody functions, where each function is constrained by two observables: the disk temperature $T_{\rm disk}$, and the fractional infrared luminosity $L_{\rm ir}/L_\star$, the fraction of the star's light reprocessed (absorbed and re-emitted) by the disk. An illustration of two observables constraining a single-component disk is depicted in Figure 1.2.

Primordial disks have been shown to dissipate fairly quickly over time in *Spitzer* disk surveys. The c2d project, observing 188 T Tauri stars spanning spectral types G5-M5 in the Taurus, Lupus, Ophiochus, and Chamaeleon star-forming regions (Padgett et al., 2006) found no studied weak-lined T Tauri stars exhibited a disk beyond an age of 10 Myr (Wahhaj et al., 2010), while the FEPS project, surveying ~ 328 solar-mass $(0.7 - 2.2 M_\odot)$ stars from ages 3 Myr to 3 Gyr, found that only $\sim 12\%$ of stars surveyed younger than 10 Myr exhibited a primordial disk, and only $\sim 2\%$ of stars surveyed between 10 and 30 Myr exhibited such a disk (Carpenter et al., 2009), suggesting that the timescale for dissipation of gas-rich disks is ~ 10 Myr. However, studies of large young clusters and associations also that high-mass star disks dissipate more quickly than those around solar-mass stars (Carpenter et al., 2006). Pecaut & Mamajek (2016) found a $\sim 9\%$ occurrence rate for primordial disks around K stars in the 10-Myr Upper Scorpius association, and $\sim 4\%$ in the ~ 15-Myr Upper Centaurus-Lupus and Lower Centaurus-Crux associations. From these, they determined an e-folding timescale for the disk

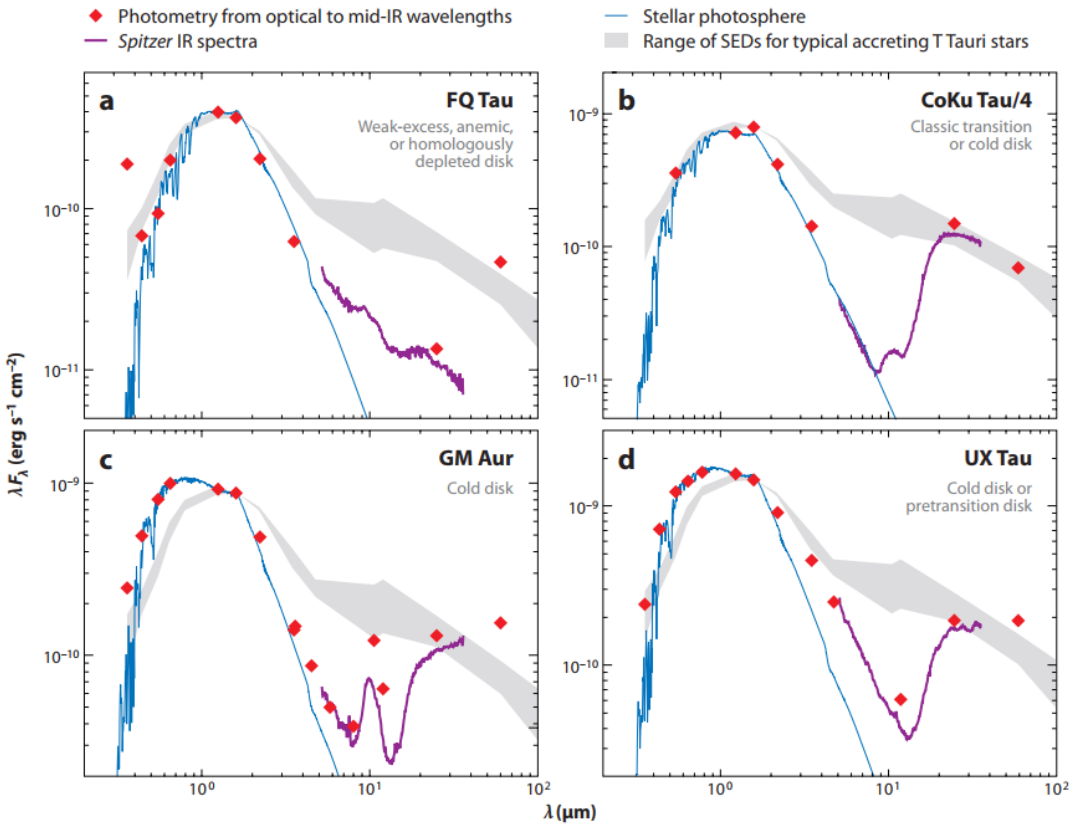

Figure 1.1: The diversity of transition disk SEDs. A weak-excess disk (a) has a significant flux decrement relative to a T Tauri SED at all mid-IR wavelengths. A classical transition disk (b) exhibits excess emission only at mid-IR wavelengths and beyond. (c) A cold disk with little near-IR emission and a strong silicate feature at 10 μm. (d) A cold disk with near-IR excess emission; alternatively, a pre-transitional disk. Figure from Williams & Cieza (2011), adapted from Najita et al. (2007).

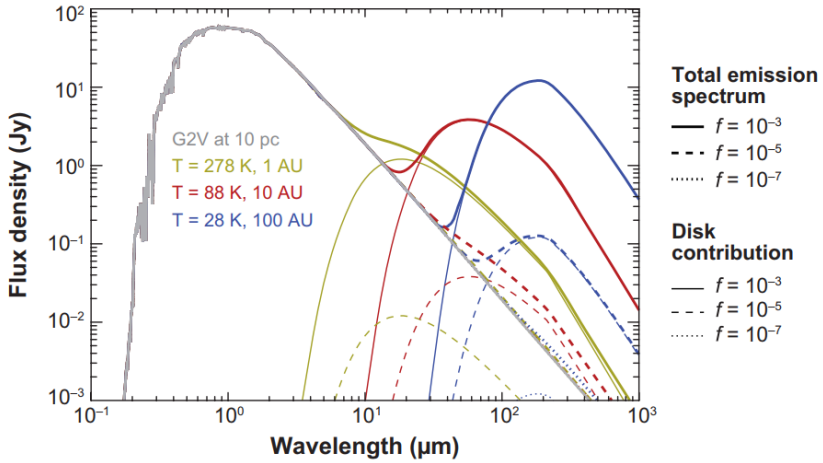

Figure 1.2: Emission spectrum of a Sun-like star at distance 10 pc with a debris disk, comprised of dust at possible temperatures $T_{\rm disk}$ = 278 K, 88 K, and 28 K (yellow, red, blue, respectively). The debris disk spectrum has been added at levels of $L_{\rm ir}/L_\star = 10^{-3}, 10^{-5}$, and 10^{-7} (solid, dashed, and dotted lines, respectively). Thick lines show the total (star+disk) emission spectrum, while thin lines denote the disk contribution. Adapted from Wyatt (2008).

frequency around K stars of $\sim$ 4.7 Myr, indicating that most K dwarf primordial disks dissipate in that timeframe. As K star disks are more prevalent than disks around solar-type stars at the same age, one would expect M stars and brown dwarfs to be even more prevalent. Indeed, studies of brown dwarfs indicate that their primordial disks persist for at least as long as those around solar-mass stars, and potentially longer (e.g. Riaz & Gizis, 2008). The most recent detailed study of disks in Upper Scorpius (Esplin et al., 2018) showed a primordial disk fraction for M stars more than three times that of all higher-mass stars combined. Further study of the lifetime of M star primordial disks, however, requires the identification of additional disks around M stars for evaluation.

1.2 Debris Disks Around M Dwarfs

WISE is much better suited than its full-sky predecessors to the search for debris disks around M dwarfs, which could yield valuable insights into the planetary sys-

tems around these stars. However, the current sample of M dwarf debris disks has significant shortcomings, limiting their utility as signposts of planetary systems. Only $\sim 2\%$ of M stars studied are currently thought to host debris disks (Deacon et al., 2013; Theissen & West, 2014; Boucher et al., 2016; Silverberg et al., 2016; Binks & Jeffries, 2017; Theissen & West, 2017), much less than the 14% expected from the mass distribution of primordial disks and the 20% fraction of A dwarfs with known disks (Greaves, 2010). Only two disks around M dwarfs have been spatially resolved, GJ 581 (Lestrade et al., 2012) and AU Mic (Kalas et al., 2004). While exoplanets have not been detected in GJ 581, recent results indicate the presence of at least one Jovian planet around AU Mic (Plavchan et al., 2017). While a cold debris disk has been reported around Proxima Centauri (Anglada et al., 2017), our nearest neighbor and a known M dwarf exoplanet host (Anglada-Escudé et al., 2016), re-analysis of the data indicates that most of the flux previously attributed to dust emission can instead be attributed to a strong millimeter flare (MacGregor et al., 2018).

Despite the dearth of M dwarf debris disk systems detected, survival models indicate that these should be common (Heng & Malik, 2013). These models suggest that this apparent absence could arise from blackbody-like dust orbiting close to the host star, making the dust difficult to detect due to its small orbit. Alternatively, this could arise from a smaller amount of dust being distributed over a large orbital separation, which would lead to dust emitting at or near detection limits (Heng & Malik, 2013). However, the possibility remains that such systems do exist, but have not yet been discovered. Testing these predictions requires a large-scale, robust search for these disks.

The search for M dwarf debris disks has become more critical in recent years, as M dwarf planetary systems have taken center stage in the search for potentially-habitable exoplanets. The lower temperature and mass of M dwarfs relative to

Sun-like stars lead to a closer-in habitable zone, the range of orbits around a star that could allow liquid water on the surface of a planet with sufficient atmospheric pressure. This smaller habitable zone radius makes exo-Earths in the habitable zone easier to detect both by the radial-velocity (e.g. Anglada-Escudé et al., 2016) and transit methods (e.g. Gillon et al., 2017). Half of M dwarfs are expected to host a $0.5 - 1.4 R_{\oplus}$ planet with an orbit in the habitable zone (Dressing & Charbonneau, 2013), a rate higher than around higher-mass stars (Bonfils et al., 2011; Howard et al., 2012). With the recent launch of the *Transiting Exoplanet Survey Satellite* (TESS; Ricker et al., 2014), designed in part with detection of planets around early-M stars in mind, the number of known planets around M dwarfs in the solar neighborhood is expected to drastically increase (e.g. Barclay et al., 2018). In concert with these exoplanet detections, M dwarf debris disks should have the same informative powers as their higher-mass cousins, if these disks can be identified.

There has yet to be a robust full-sky search for M dwarfs with significant excess at 22 μm. The largest scale searches for M dwarf debris disks at 22 μm have been limited to the SDSS footprint (Theissen & West, 2014, 2017), cross-matching targets with 2MASS and WISE. These searches, however, focused on excess at 12 μm (the W3 band) rather than 22 μm, due to the low signal-to-noise of their sources at W4. Most M dwarf debris disk searches begin with a sample of M dwarfs, and then search for evidence of a disk (e.g. Schneider et al., 2012b; Theissen & West, 2014, 2017; Binks & Jeffries, 2017). While this approach guarantees that any disks found will be M dwarf disks, it limits the search to known targets only. Alternatively, one could begin with identification of likely disk candidates, and then determine which candidates were M dwarfs.

1.3 Disk Detective: Identifying New Circumstellar Disks with Citizen Science

The Disk Detective project (Kuchner et al., 2016), a member project of the Zooniverse network of Citizen Science Alliance projects (Lintott et al., 2008), performs the required visual inspection of infrared excesses from WISE via the contributions of citizen scientists. These participants ("users") visit a website, DiskDetective.org, to examine "flipbooks" of images of the same target from WISE, the Two-Micron All-Sky Survey (2MASS), the Digitized Sky Survey (DSS) and the Sloan Digital Sky Survey (SDSS). Images are independently scaled to match color to the full range of data in each image. Each flipbook is overlaid with a red circle of radius 10.5 arc-seconds, a conservative choice (given the 12″ FWHM) to indicate the approximate area that must be free of contamination for the photometry to be reliable. A cross indicating the central position of the object at W1 (3.4 μm emission) is also overlaid, to aid the eye in detecting positional shifts from image to image.

Users view the flipbook by clicking an arrow-shaped "play" button; alternatively they can scroll through the flipbook frame-by-frame using a scrub bar beneath the display. Each frame is labeled with the wavelength and source of the image (e.g. "2MASS J (1.235 μm)"). After viewing the full flipbook, a user answers a multiple-choice question, "What best describes the object you see?," by selecting one or more of six options given: "Multiple objects in the Red Circle," "Extended beyond circle in *WISE* Images," "Empty Circle in *WISE* images," "Not Round in DSS2 or 2MASS images," and "None of the Above/Good Candidate." Except for the "Good Candidate" option, users can choose more than one description per flipbook. After at least one option is selected, a "Finish" button becomes active; clicking this button records the user's choice(s) for interpretation

by the project science team and causes the website to present another source for classification. This approach leverages the human eye's capability of detecting moving objects camouflaged by noise to identify and select clean point sources from a metaphorical haystack of galaxies, ISM, image artifacts, etc. (Kuchner et al., 2016)

Since launch in January 2014, over 30,000 users have made over 3.1 million classifications of WISE-detected excesses via the website. However, a plurality of website classifications come from a group of highly-dedicated volunteers. Shortly after project launch, this group began their own email discussion group for the project to work together on interesting problems they found in the course of their classifications, and to better interface with the science team. Since then, members of this "advanced user group" have helped train other users and researched follow-up targets in the literature. They are a critical extension of the Disk Detective science team (Kuchner et al., 2016).

In addition to the website-based classification to evaluate false positives, Disk Detective has a robust follow-up process to ensure the quality of disk candidates that are published. This follow-up includes a literature review of targets driven by the advanced user group, which flags previously-identified disks and known non-disk false-positives (e.g. active galactic nuclei, M giants that produce their own dust). Targets that survive this review then are followed up with high-resolution imaging at red-optical and near-IR wavelengths to identify background objects that could contribute to a potential blend at W4. In the Northern Hemisphere, follow-up is done in the red-optical/near-IR Sloan i band with the ROBO-AO instrument (Baranec et al., 2013), both on the 60-inch telescope at Mt. Palomar, and on the 2.1-m telescope at Kitt Peak National Observatory. In the Southern Hemisphere, follow-up imaging has been done in the near-infrared Yc and Hc bands with the RetroCam instrument on the 100-inch Ireneé R. Dupont tele-

scope at Las Campanas Observatory (Rheault et al., 2014). These targets also receive follow-up medium-resolution spectroscopy to determine spectral types and luminosity classes, as many of these targets have not been previously studied.

Disk Detective is uniquely positioned to answer three key questions in the search for circumstellar disks with WISE: evaluation of false positive rates for disk detection from AllWISE and individual disk searches in WISE; discovery of new forms of circumstellar disk, including further evaluation of the potential for primordial disks around M stars to survive > 10 Myr; and identification of M dwarf disks. Disk Detective's large input catalog ensures that with some exceptions, it will identify any disks with significant ($[W1]-[W4] > 5\sigma_{[W1]-[W4]}$) excess at 22 μm, such that the expected yield of disks from Disk Detective is functionally equivalent to the expected yield of disks with 22 μm excess from AllWISE. Disk Detective can apply false-positive rate statistics based on its high-resolution follow-up imaging to other published disk searches to estimate their false-positive rates. Because it encompasses the full sky, Disk Detective is also uniquely positioned to identify potential new types of disk; its increased sensitivity also allows it to probe dust around stars that were too faint for previous full-sky searches. In some respects, the Disk Detective input catalog is better suited to detection of M dwarfs than other large-scale searches for disks in WISE because it does not limit itself to cross-matches with V-band-limited surveys like *Tycho* (Cotten & Song, 2016) or *Hipparcos* (Wu et al., 2013; Patel et al., 2014), making it more sensitive to late-type stars that are intrinsically fainter in V than early-type stars.

The following chapters explore each of these concepts. In Chapter 2, we present the results of Silverberg et al. (2018), in which we statistically characterize the classification of subjects in the Disk Detective input catalog, from website classification to high-resolution follow-up imaging, to estimate the rate of false positive

disk detections from AllWISE and the expected number of disks in AllWISE; we then apply our derived false-positive rates to other published WISE-based disk searches, and present 244 new disk candidates. In Chapter 3, we present the results of Silverberg et al. (2016), in which we describe our identification of WISEA J080822.18-644357.3 (J0808), a disk with infrared excess indicative of substantial amounts of gas at an age well beyond the expected age for a primordial disk, using pre-*Gaia* astrometry. In Chapter 4, we present high-cadence optical imaging and near-infrared spectroscopy of J0808, and update its kinematics with data from *Gaia*; introduce the concept of"Peter Pan" disks, a class of extremely long-lived primordial disks, of which WISEA J080822.18-644357.3 is a member; present four new identifications of Peter Pan disk candidates using *Gaia astrometry*; and discuss possible mechanisms that could allow a gas-rich disk to survive so far beyond its expected lifetime. Finally, we summarize our findings in Chapter 5.

Chapter 3 was published in 2016, and reflects the release of *Gaia* DR1, but not DR2. The results from *Gaia* DR2 are reflected in Chapter 4. Throughout Chapters 2-4, in cases where previously-published text has been superseded by new information, I present this new information in a footnote.

Chapter 2

Follow-Up Imaging of Disk Candidates from the Disk Detective Citizen Science Project: New Discoveries and False-Positives in WISE Circumstellar Disk Surveys*

2.1 Introduction

With higher sensitivity than any previous full-sky infrared survey instrument, the *Wide-field Infrared Survey Explorer* (WISE; Wright et al., 2010) detected over 747 million sources in its all-sky survey. Many teams have searched for new circumstellar disks in the WISE data based on infrared excess at W4 (22 μm emission) compared to W1 (3.4 μm emission), discovering thousands of candidate debris disks (see e.g. Kennedy & Wyatt, 2013; Wu et al., 2013; Patel et al., 2014; Cotten & Song, 2016; Patel et al., 2017) and YSO disks (Liu et al., 2011; Rebull et al., 2011; Liu et al., 2014; Koenig & Leisawitz, 2014; Koenig et al., 2015). In particular, because of its sensitivity and full-sky scope, the WISE mission is uniquely suited to the search for M dwarf debris disks, which are of particular interest due to the relative lack of detected disks around these stars in comparison to higher-mass stars (e.g. Plavchan et al., 2005, 2009; Lestrade et al., 2009; Avenhaus et al., 2012; Theissen & West, 2014; Morey & Lestrade, 2014; Binks & Jeffries, 2017).

However, confusion and contamination limit every search for disks with WISE. The point spread function (PSF) at W4 has a full-width at half-maximum of 12″. This wide PSF can allow emission from multiple point sources (e.g., background

*The contents of this chapter were previously published in Silverberg et al. (2018).

stars) or image artifacts to contribute to the W4 photometry, producing a false-positive [W1]-[W4] excess. Additionally, the color loci of debris disks and YSOs overlaps the color loci of several other astronomical phenomena, including background galaxies and stars embedded in nebulosity (Koenig et al., 2012). To eliminate these false-positives, objects must be examined in visible and near-infrared images along with the WISE images. Most published searches have utilized visual inspection of the WISE images (see e.g. Debes et al., 2011; Kennedy & Wyatt, 2012; Wu et al., 2013; Cruz-Saenz de Miera et al., 2014; Patel et al., 2014) to address these contamination and confusion problems.

Kennedy & Wyatt (2012) produced a study of these confusion and contamination issues, focusing on infrared excesses around stars observed by *Kepler* (Borucki et al., 2010), with the goal of expanding the number of known stars that host both planets and debris disks. They searched for infrared excesses in a cross-match of the Kepler Input Catalog (KIC) to 2MASS and WISE, finding 7965 disk candidates. However, they argued that all but 271 (3.4%) of these objects were coincident with Galactic dust emission, as identified by the IRAS 100 μm background, and therefore false positives.

The Disk Detective citizen science/crowdsourcing project (Kuchner et al., 2016, hereafter Paper 1) uses citizen science to examine infrared excess candidates from WISE, beginning with a website, http://www.diskdetective.org, where volunteers examine images from WISE, the Two-Micron All-Sky Survey (2MASS), the Digitized Sky Survey (DSS), and the Sloan Digital Sky Survey (SDSS) to check for false positives. Since launch in January 2014, over 30,000 users have made over 2.6 million classifications via this Zooniverse website. Shortly after project launch, a group of highly-dedicated volunteers began their own email discussion group for the project. Since then, members of this "advanced user group" have helped train

other users and research follow-up targets in the literature, and now form a crucial extension of the Disk Detective science team (Paper 1).

In this paper, we address two specific forms of false positive that occur in the Disk Detective input catalog and other searches for circumstellar disks with WISE:

1. **Confusion in the WISE images:** the contribution to noise in an image due to superposed signals from faint unresolved sources that cluster on the scale of the observing beam.

   (a) We use data from the Digitized Sky Survey (DSS), the Sloan Digital Sky Survey (SDSS), and the 2-Micron All-Sky Survey (2MASS) to search for background sources via the Disk Detective website.

   (b) We use high-resolution imaging on small telescopes (the 1.5-m Telescope at Mt. Palomar and the Du Pont Telescope at Las Campanas) to identify background sources that are too faint for SDSS and 2MASS or unresolved by these surveys.

2. **Contamination of the WISE images:** the presence of image artifacts (e.g. diffraction spikes, latent images, or optical ghosts) within the WISE beam. We search for these contaminants by examining the WISE images via the Disk Detective website.

We present the first results from our follow-up imaging campaigns with the Robo-AO adaptive optics instrument on the 1.5-m telescope at Palomar Observatory (Baranec et al., 2014) and the RetroCam instrument on the Du Pont telescope at Las Campanas Observatory in Chile (e.g. Rheault et al., 2014). These instruments provided an angular resolution of $0\farcs15$ and $< 1''$ respectively, improving on the

5″ effective resolution of the 2MASS Point Source Catalog[1]. We combine these observations with the results of the website-based evaluation to estimate the fraction of WISE excesses that are true disk candidates. In Section 2.2, we review our website classification procedure, analyze the distribution of clean sources and false positives, and consider the results of an advanced-user-driven literature review. In Section 2.3, we review our procedure for selecting these particular targets for further examination, and discuss our methodology for collecting high-resolution images of these targets. In Section 2.4, we describe our method for identification of contaminated targets. In Section 2.5, we present the results of our follow-up observations, estimate the presence of further unresolved sources, and combine these with the results from website analysis to estimate the ultimate yield of the Disk Detective input catalog. We apply these findings to other surveys in Section 2.6, including re-analysis of the M dwarf disk search of Theissen & West (2014). In Section 2.7, we present our list of uncontaminated disk candidates. Finally, in section 2.8 we summarize our results and discuss future plans for these targets and high-resolution follow-up imaging.

2.2 Rejection of False Positives Via the DiskDetective.org Website and Literature Review

The online engine of our citizen science disk search is DiskDetective.org, where users view sets of images showing the same WISE point source in several bands. In this section, we review our online classification method (discussed in more depth in Paper 1), and analyze the latest online classification results.

[1]As listed here: `https://www.ipac.caltech.edu/2mass/releases/allsky/doc/sec2_2a.html`

2.2.1 DiskDetective.org: Identification of WISE Debris Disk Candidates with Citizen Science

The selection of our input catalog is detailed in Table 1 of Paper 1. Briefly, we selected objects from the AllWISE Source Catalog with significant [W1]-[W4] excess ($[W1]-[W4] > 0.25, [W1]-[W4] > 5\sigma_{[W1]-[W4]}$) and high signal-to-noise (SNR > 10) at W4 that were not flagged as being contaminated in any way as part of the AllWISE source processing. These objects become "subjects" as part of our input catalog.[2] For each subject, we generated a "flipbook" of 9-15 1-arcminute-square images of the subject from the Digitized Sky Survey (DSS), the seventh data release of the Sloan Digital Sky Survey (SDSS DR7), 2MASS, and AllWISE. Images were overlaid with a red circle of radius 10.5 arcsec, the area that must be clear of contamination for the AllWISE photometry to be trustworthy, and small crosshairs indicating the center of the W1 source. Users view each flipbook as an animation, or scroll through frame-by-frame using a scrub bar. Users then choose from six classification buttons, labeled "Multiple objects in the Red Circle," "Object Moves off the Crosshairs," "Extended beyond circle in WISE Images," "Empty Circle in WISE Images," "Not Round in DSS2 or 2MASS images," and "None of the Above/Good Candidate." Users can choose either "None of the Above," or as many of the other descriptions as apply to a target. This classification method robustly identifies type-1a and type-2 false positives, as described above.

In this paper we focus only on subjects that have been retired from active classification, which we refer to as "complete." In Paper 1, we defined this cutoff as 15 classifications. After the publication of Paper 1, we put into place a new retirement scheme, and corrected some objects for saturation effects at W1. The

[2]The full input catalog is available via the MAST archive, `https://mast.stsci.edu`.

new retirement scheme is described in Appendix A.1.1, and our correction for W1 saturation is treated in Appendix A.1.2. As of 2018 January 5, 62% of subjects were complete, providing the large sample of 149,273 subjects we analyze here.

We define a "good" subject as one where the majority of classifiers of a subject label it "None of the Above/Good Object." We refer to a subject as "multiple" if a majority of classifiers labels that subject as having "Multiple objects in the Red Circle;" these "multiple" subjects are the dominant false positive rejected by our volunteers. We choose this definition (based on a majority of classifiers rather than a majority of votes) because users can select more than one option with each classification; this metric shows us subjects that most users agree have "multiple objects in the red circle," even if they also have other flaws. For convenience, we refer to all subjects that do not meet these definitions of "good" or "multiple" as "other" in this paper.

2.2.2 False Positive Rates in Website Classifications

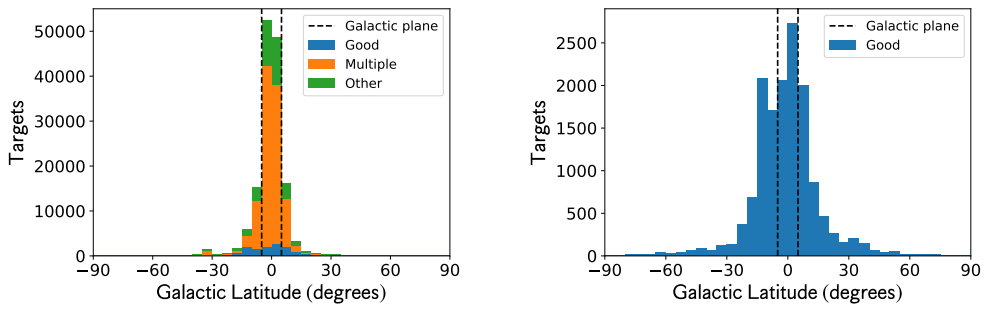

Figure 2.1: Left: distribution of complete subjects as a function of Galactic latitude. Right: distribution of complete "good" subjects. "Good" subjects were classified as "None of the above–good candidate" by more than 50% of classifiers."Multiple" subjects were classified as "Multiple objects in the red circle" by more than 50% of classifiers. All other complete subjects were labeled "other."

Figure 2.1 shows the distribution of raw numbers of complete subjects broken down by category ("good," "multiple," or "other") as a function of Galactic

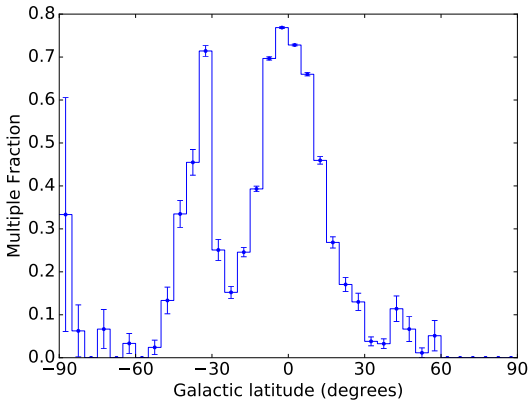

Figure 2.2: Rate of "multiple" subjects as a fraction of all complete subjects as a function of Galactic latitude. "Multiple" subjects are most common in the Galactic plane, and in the Large Magellanic Cloud (LMC).

latitude, and the distribution of "good" objects alone as a function of Galactic latitude. Most of the complete subjects are false-positives; only 9.80% (±0.08%) of the complete subjects are labeled "good" by a majority of volunteers. "Multiples" are the dominant form of false positive—they make up 68.87% (±0.12%) of all complete subjects.

Figure 2.2 shows the rate of multiples as a function of Galactic latitude. "Multiples" dominate especially in the Galactic plane; 74.84% (±0.16%) of subjects in the $-5° < b < 5°$ range were classified as multiples, while only 4.74% (±0.30%) of subjects in that range are good, with over 100,000 complete subjects in this range. We also observe a large spike in "multiple" rate between Galactic latitude $-35° < b < -30°$. Figure 2.3 shows the density of "multiples" (i.e. the fraction of subjects that are multiples) as a function of Galactic latitude and longitude (brighter indicates a larger fraction); this plot reveals that the spike in the $-35° < b < -30°$ range in Figure 2.2 is associated with the LMC. Figure 2.3 also shows a higher density of "multiples" in the SMC than in its surroundings. Our statistics are poor in the $60° < b < 90°$ range because there are fewer complete subjects in this region of sky, which only recently became active on the website.

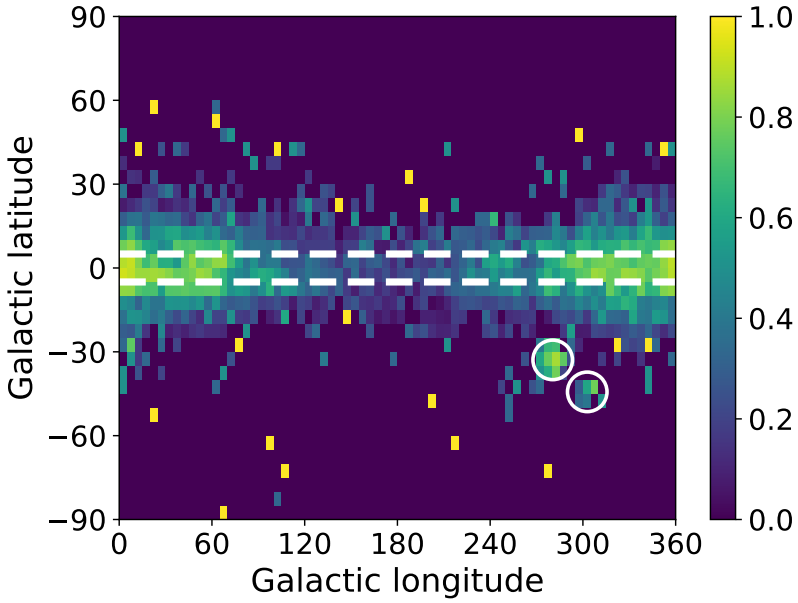

Figure 2.3: Heatmap showing the fraction of complete objects in each 5° × 5° bin that are "multiple." Brighter indicate where a larger fraction of the total has been classified as "multiple." The darkest color indicates that a bin contains no multiples. Multiples are more prevalent in the plane (between white dashed lines) of the Galaxy and toward Galactic center. Outside of the Galactic plane, a higher density of "multiples" is observed in the Large and Small Magellanic Clouds (locations indicated by the white circles).

2.2.3 Literature Review by Citizen Scientists

The next stage of our process is to review the published literature on each of the good objects, discard point-source false positives like known M giants, classical Be stars and AGN, and note re-discoveries of well-studied disk systems. While this task began as a science team function, we have since trained members of the advanced user group to use SIMBAD and VizieR themselves to perform some of this work, as detailed in Paper 1. These citizen scientists also reexamine the website flipbooks for these subjects as an additional check on the website classification. We require a minimum of two opinions on each object before a good candidate can become a Disk Detective Object of Interest (DDOI), an object worthy of additional follow-up observations. We decided that any previously-known,

well-studied disk systems (e.g. systems observed by the *Spitzer Space Telescope*, or with coronagraphic disk images) should not be designated as DDOIs, because our observing resources were better used on confirming newly detected excesses rather than following up well-studied disks; however, these systems are still valid disk detections, so we do not eliminate them as false positives.

So far, the advanced user team has reviewed 1465 good subjects. Of these, 1011 have become DDOIs, while an additional 252 subjects have not become DDOIs because they are known well-studied disk systems,[3] for a false positive rate from literature review of **14**%.

2.3 Follow-up Target Selection and Observations

We have performed follow-up imaging of a subset of our DDOIs using the Robo-AO on the 1.5-m telescope at Mount Palomar and the RetroCam instrument on the Irenée R. Dupont telescope at Las Campanas Observatory. Here we describe our target selection, observations, and reduction methodology for each telescope.

2.3.1 Robo-AO Observations

We observed 230 targets in the Sloan-i filter (Baranec et al., 2014) with adaptive optics using Robo-AO. Dates of observations and number of targets observed on each date are listed in Table 2.1. Targets were selected for visibility from Mt. Palomar, 2MASS $J < 14.5$ and $i < 17$, the limiting magnitude of the telescope. Targets were observed as a sequence of full-frame-transfer detector readouts at the maximum rate of 8.6 Hz for 90 seconds of total integration. We corrected the individual images for detector bias and flat-fielding effects, and then combined

[3]These numbers were as of 2018. The current number of DDOIs listed in the database as of 2019 April 3 is 1,738, though some records are still being entered into the database.

Table 2.1. Summary of Observations with Robo-AO

UT Date	Objects Observed
2014-06-14	15
2014-06-15	12
2014-06-16	2
2014-06-19	1
2014-07-12	1
2014-07-13	18
2014-07-14	1
2014-07-16	1
2014-07-17	6
2014-07-18	1
2014-08-21	2
2014-08-29	4
2014-08-30	2
2014-08-31	65
2014-09-01	3
2014-09-02	1
2014-09-03	1
2014-11-06	1
2014-11-09	9
2014-11-10	26
2014-11-11	41
2015-03-08	3

them using post-facto shift-and-add processing, using the target star as the tip-tilt star with 100% frame selection to synthesize a long-exposure image. Additionally, we synthesized shorter-exposure images by selecting smaller percentages of frames based on quality, as in lucky imaging. In most cases, these yielded an inner working angle for detecting background objects of $\sim 0.15''$, far less than the $6''$ of the $W4$ half-width at half-maximum (HWHM).

Table 2.1 (cont'd)

UT Date	Objects Observed
2015-03-09	18

2.3.2 Dupont/RetroCam

We also collected high-resolution images of 166 targets (including 15 observed with Robo-AO) in the Yc ($\lambda_c = 1.035\mu$m) and Hc ($\lambda_c = 1.621\mu$m) filters using RetroCam on the 100-inch (2.54-m) Ireneé R. DuPont Telescope at Las Campanas Observatory. Dates of observations and number of targets observed on each date are listed in Table 2. Targets were selected for visibility from Las Campanas and primarily for 2MASS $J < 14.5$. We observed targets using a five-point "dice" dither pattern. Individual images were corrected for dark current, and flat-fielded using the difference between lamp-on and lamp-off dome flats. H-band sky images were generated for each target by median-combining images in a dither sequence without aligning them, removing stellar contributions via sigma-clipping. The H-band science images were then sky-subtracted, using the sky image for that target. Once images were completely reduced (dark, flat, and sky corrected), images for each target in each band were then combined with the `imalign` and `imcombine` procedures in IRAF, using bright stars in the field of view (including the target star) to align the image stack. Seeing in these observations (as measured by the FWHM of a star other than the target in the stacked image) was generally $\sim 0.8''$, still smaller than the $W4$ HWHM.

Table 2.2. Summary of Observations with RetroCam/Dupont

UT Date	Objects Observed	Minimum Total Integration Time (s)	Maximum Total Integration Time (s)
2015-06-30	4	25	25
2015-07-01	52	25	100
2015-07-02	27	25	100
2015-10-26	19	25	100
2015-10-27	39	25	100
2015-10-28	40	25	100

2.4 Image Analysis

A group of ten citizen scientists examined the Robo-AO data with the SAOImage `DS9` software package to visually examine the data to identify images with faint background objects, providing them with a set of images analyzed by the science team as a training set. We developed the following method for qualitative analysis:

1. Display the image with 100% frame selection as black/white grayscale, min/max, linear scaling, to identify the target star.

2. Shift the display to "`zscale`"[4] to look for fainter objects. This allows fainter background objects to emerge more clearly than they would otherwise.

3. Identify any faint background objects in the field of view, noting their positions.

4. Note which objects have background objects within 12 arcseconds of the target star.

Each volunteer independently analyzed a subset of the images using the above

[4]A linear scaling around the median value of a subset of the image.

method. The group then discussed each image together to reach a consensus on each target. We followed a similar procedure with the Dupont data.

This visual inspection identified targets with evidence of background sources that could produce a false positive excess. We then quantified whether these background sources significantly affected the excess at W4. To estimate the contribution each background object made at W4, we determined magnitudes for the background objects with aperture photometry using the IRAF `DAOphot` package. We assumed that background objects exhibited either an M dwarf SED, or a power-law SED with spectral index 0 (corresponding to a YSO or heavily-reddened early-type star), and determined the colors of these objects (calculated in Appendix A.2 and presented in Table A.1). Using the recorded photometry and these colors, we estimated the flux of the background object at W4, and subtracted this flux from the total W4 flux to yield the intrinsic flux of the target itself (including any contribution from circumstellar material). We then re-calculated the target's [W1-W4] color using this corrected W4 flux to determine if a significant excess remained. The results are described in Section 2.5.

2.5 False Positive Rates of AllWISE Disk Detections

In this section, we determine false-positive rates based on the follow-up observations and unresolvable IR-bright background objects. We then combine these with the classification and literature-review data to determine the overall false-positive rate for Disk Detective thus far, from which we estimate the eventual final yield of disks from AllWISE.

2.5.1 False-Positive Rates from High-Resolution Follow-up

The results of quantitative analysis of the 261 targets with reliable photometry observed with Palomar/Robo-AO and Dupont/Retrocam are presented in Figure 2.4. We combine the two samples without adjustment because (as described in Appendix A.2) both instruments are similarly sensitive to the same background objects. Overall, 244 of these 261 targets retain a significant infrared excess after the contribution of background objects has been removed, for a false-positive rate of $7\% \pm 1\%$. There is no detectable significant difference in contamination rate in the Galactic plane due to the relatively small numbers involved (compared to the overall Disk Detective input catalog). Of the 39 objects in the $-5^\circ < b < 5^\circ$ range, 3 are contaminated, leaving a false positive rate of 8%(±4%). Out of the plane, 14 of 222 targets are contaminated, leaving a false positive rate of 6%(±2%).

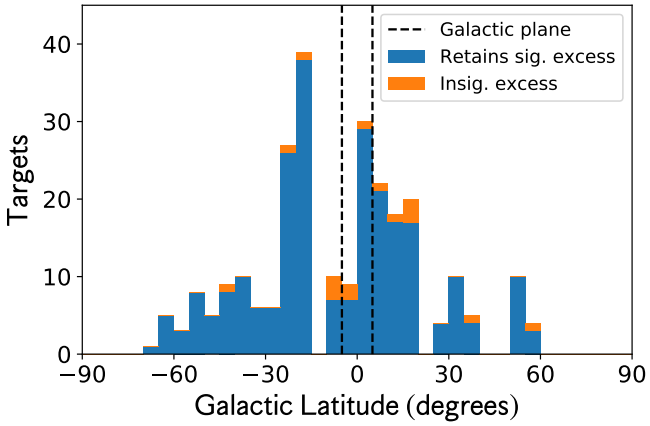

Figure 2.4: Objects with high-resolution imaging from Robo-AO and Dupont as a function of Galactic latitude. The overall false-positive rates are low in comparison to the rates from our website-based analysis. The rates inside and outside the Galactic plane show no significant difference.

We identified 16 objects as having insufficient excess at W4 once the estimated contributions from background objects were removed. We list these objects in

Table 2.3. Targets with False-Positive Excesses Due to Background Objects in High-Resolution Follow-up Observations

Identifiers		Previous
Zooniverse	WISEA	Citations
AWI0005w52	J000308.37+424452.4	
AWI0005yiz	J010722.60+380143.9	1
AWI0002vbd	J020206.67+601741.4	
AWI0003cs7	J021532.17+591424.4	
AWI0004nfu	J032853.67+490412.8	1
AWI0000uj2	J153046.05+342756.4	1,2,3
AWI00006nb	J161808.08+104551.4	
AWI0005bk2	J172912.43+005605.7	
AWI0005brq	J181949.03+310841.7	
AWI0005bud	J184141.31+313703.4	
AWI0005lx9	J193040.05+350609.9	
AWI00055by	J204443.79+425654.9	4
AWI0005vyx	J212959.78+413037.3	
AWI0005a9r	J215305.45+682955.0	1
AWI0005w1h	J220503.97+444543.7	
AWI0000kk6	J220601.14-020343.2	

References. — (1) Paper 1. (2) Wu et al. (2013). (3) Cotten & Song (2016). (4) Clarke et al. (2005)

Table 2.3, as well as any previous identifications as excess targets.

2.5.2 False-Positive Excess from Unresolvable Infrared Galaxies

While the Robo-AO and RetroCam observations catch many otherwise-unresolved background sources, they leave one potential source of confusion unexplored: objects clustered on the scale of the W4 beam with no counterpart in near-IR or red-optical light, such as luminous or ultra-luminous infrared background galax-

ies, or (U)LIRGS (Papovich et al., 2004). While WISE is not well-suited to exploring the density of these phenomena, previous higher-resolution mid-infrared surveys, operating at similar wavelengths, can provide constraints. Papovich et al. (2004) used *Spitzer*/MIPS data to identify a previously-undetected population of infrared-luminous galaxies, quoting a cumulative distribution of number of galaxies as a function of source brightness at 24 μm. We can use this distribution to estimate the confusion noise from these galaxies in our 22 μm data if we correct for sources that would be detected in website classifications and follow-up imaging.

We determined the minimum flux at W4 for a background galaxy to produce a false positive excess, assuming a bare stellar photosphere in the Rayleigh-Jeans tail. We also estimated the flux at W4 at which a background galaxy would produce a visible signal in 2MASS H images, assuming that such an object would be visible if its 2MASS H flux were half that of the target.[5] We applied these numbers to every good subject, finding the cumulative number of sources per steradian bright enough to produce a false positive, and subtracting from that the cumulative number of sources per steradian bright enough to have been detected as a background object in shorter-wavelength data. We then multiplied by the angular beam width at W4 to get the expected number of sources. We treated this as a probability of the number of sources in the beam for each object, summing the probability for each object to estimate the number of good objects for which a background galaxy was the source of the false-positive.

Of the 14,681 complete good subjects, we expect that 7.4 ± 2.7 subjects, or $0.05\% \pm 0.02\%$, are contaminated by an unresolved background infrared-luminous galaxy, a negligible contribution.

[5]This ensures that we only consider background galaxies faint enough to not be detected in our follow-up images)

2.5.3 Expected Total Number of Disks in AllWISE

Combining the data from user classifications, advanced user review, high-resolution follow-up observations, and background galaxy count estimates, we find that of the 149,273 complete subjects on the Disk Detective web site, 7.9% ($\pm$0.2%) are likely to be stars with circumstellar material. 90.20% of subjects are eliminated by website evaluation; 1.35% were eliminated by literature review; 0.52% were eliminated by follow-up observations; and a near-negligible fraction ($< 0.01\%$) are expected to have a false-positive due to undetectable background galaxies.

Applying this number to the full brightness-limited sample currently on the website, we would expect to find $\sim 21,600$ disk candidates overall, out of 272,022 subjects in the brightness-limited input catalog. Given that this analysis does not incorporate false positives that are only identifiable in spectroscopic follow-up (e.g. M giants, classical Be stars), we expect that this number is an upper limit to the number of debris and YSO disks with W4 excess in the AllWISE catalog. This 8.0% figure is higher than the 3.4% found by Kennedy & Wyatt (2012). We attribute some of this difference to our full-sky scope, as Kennedy & Wyatt (2012) only considered sources in or near the Galactic plane. We also hypothesize that some of the difference can be attributed to our detailed visual inspection of each source, rather than adopting a simple across-the-board cut based on 100μm flux, as they did.

2.6 Application to Other WISE Disk Searches

Given its large input catalog compared to other surveys, Disk Detective is well positioned to not only identify new warm debris disks in the WISE catalog, but inspect and re-evaluate disks identified by other researchers. In this section, we estimate the numbers of published disks from other searches that are likely false

positives, and present a visual re-inspection of the M dwarf disk sample presented by Theissen & West (2014).

2.6.1 False-Positives in Previous WISE Disk Searches

Because our sample encompasses the full 2MASS/WISE cross-match, we can apply our false positive rates to other searches for warm debris disks with WISE. While we cannot assess individual objects in other surveys due to limited overlap with our follow-up, we estimate the number of disks in each survey likely to be a false positive based on the rates we determined, depicted in Figure 2.5.

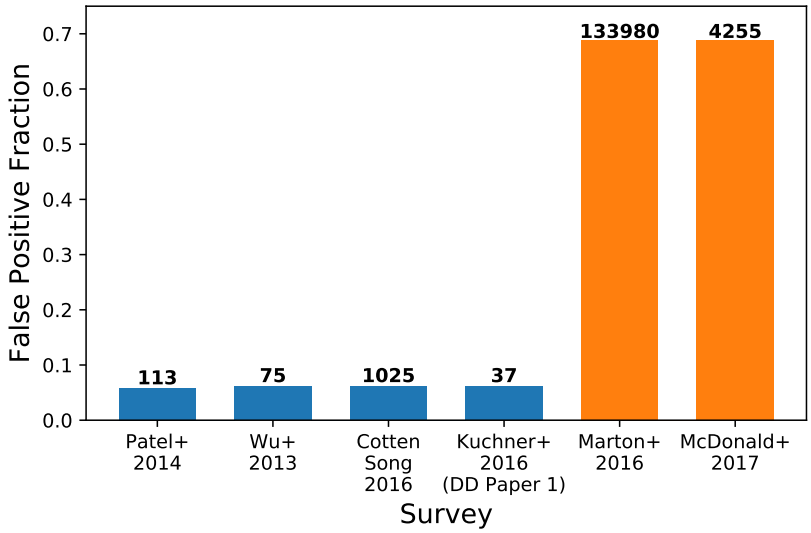

Figure 2.5: Expected false-positive fractions for published WISE disk searches. Searches that incorporate visual inspection of images (blue bars) have lower expected false-positive fractions than those that do no incorporate visual inspection (orange bars). Numbers above each bar indicate the number of disk candidates in each search.

- **Patel et al. (2014).** This survey specifically avoided the Galactic plane in its cross-match with the *Hipparcos* catalog (van Leeuwen, 2007), so we similarly apply an out-of-plane contamination rate. We will assume that the visual inspection described by the authors is comparable to the inspection

and literature review by the Disk Detective team, and will thus only apply the rate of contamination from follow-up imaging. Of the 113 new warm disks that were detected in this survey (Patel et al., 2015), we expect ~ 7 to have previously-undetected background objects that would contribute to a false-positive excess detection.

- **Wu et al. (2013).** This survey did not specifically avoid the Galactic plane as a selection criterion in its cross-match with *Hipparcos*, so we apply the statistics for the full sample to this paper's sample of 75 previously-unidentified main sequence stars with infrared excess indicative of a disk. We would therefore expect ~ 5 of these targets to be contaminated by one or more otherwise-undetected background objects.

- **Cotten & Song (2016).** This search identified ~ 1750 debris disk candidates from a thorough review of pre-WISE disk literature and a cross-match of AllWISE with the Tycho-2 (Høg et al., 2000) survey, of which 1025 are new excess detections. Applying our recovery rate for high-resolution follow-up to this sample, we would expect that ~ 64 targets would be contaminated by background objects only recoverable in high-resolution images that could produce a false-positive excess detection.

- **McDonald et al. (2012), McDonald et al. (2017).** These searches cross-matched photometry data from *Hipparcos*, *Tycho*, and various other catalogs, using astrometry from, respectively, *Tycho* and *Gaia*. These works then used SED fitting of the cross-matched data to estimate stellar and excess parameters for $> 100,000$ objects. However, neither search considered the source of the excess (e.g. self-produced dust around AGB stars rather than debris disks), and neither search included a robust visual inspection of the actual images (which eliminates $\approx 90\%$ of excess candidates in the

Disk Detective search), relying instead on visual inspection of the fit SEDs. Because these searches select for objects with star-like SEDs rather than preselecting sources with infrared excess the way our search does, we cannot directly apply our overall false-positive rates to their search. However, since we estimate there to be $\sim 21,600$ disk candidates in AllWISE, we expect that $> 79,000$ of the excesses identified by McDonald et al. (2012) and McDonald et al. (2017) are false positives.

- **Marton et al. (2016).** This search used support vector machines (SVM), a class of supervised learning algorithm, to identify 133,980 YSO candidates in AllWISE, by identifying objects that were a given type of false positive in the data via SIMBAD, and using these to train the SVM to avoid such objects. However, there was no visual inspection of the images, sources were not pre-selected for excess, the W4 PSF was not taken into account, and there is no acknowledgement of multiples, which make up the bulk of our false-positives. If we assume that the SVM algorithm identifies non-multiple false positives as effectively as Disk Detective, literature review would eliminate the SIMBAD-identified non-YSOs in their final sample (as per Table 1 of that paper), and also assume a similar number of objects would be false positives in follow-up imaging, this leaves a lower limit false-positive rate of 74%. While a search through WISE using machine-learning algorithms could prove valuable, the number of false positives that are only identified by visual inspection of images suggests that any such system would need to take the images themselves into account, rather than strictly learning based on photometric points and data quality flags.

- **Kuchner et al. (2016).** As Paper 1 was published before analysis of Robo-AO and Dupont photometry was complete, we also apply our rate analysis

to this paper. Of the 37 new disk candidates presented in that paper, we expect that ~ 2 would be contaminated.

The targets WISEA J153046.05+342756.4 (Zooniverse "ZooID" AWI0000uj2), WISEA J010722.60+380143.9 (ZooID AWI0005yiz), WISEA J032853.67+490412.8 (ZooID AWI0004nfu), and WISEA J215305.45+682955.0 (ZooID AWI0005a9r) present salient examples of the importance of imaging follow-up. AWI0000uj2, an A0 star, appears in Wu et al. (2013), in Cotten & Song (2016) as a "Reserved" excess candidate, *and* in Paper 1. AWI0004nfu appears in Paper 1 and Zuckerman et al. (2012). AWI0005yiz and AWI0005a9r were both detected for the first time in Paper 1.

Based on our follow-up observations with Robo-AO, all four of these objects have no excess once the contribution from background objects is subtracted at W4. AWI0000uj2 is likely significantly contaminated at W4 by two objects ~ 4 magnitudes fainter than it in the Sloan i band. AWI0004nfu exhibits seven background objects $3-9$ magnitudes fainter than it. AWI0005yiz exhibits several background objects $\sim 5-8$ magnitudes fainter than it, and AWI0005a9r exhibits several background objects $3-10$ magnitudes fainter than it in Sloan i. Further analysis and observations (e.g. additional wavelength coverage of the background objects to confirm the shape of their SED) are required to confirm that the observed excess is significantly affected by these targets. However, these cases illustrate that high-resolution follow-up can impact the quality of published infrared excesses.

2.6.2 A Re-Assessment of a Previous WISE-based M Dwarf Disk Search

M dwarf disk systems are particularly invaluable systems to identify. M dwarfs are key targets for large-scale exoplanet searches (e.g. Irwin et al., 2009; Ricker

et al., 2014), and host some of the most unique exoplanetary systems discovered to date (e.g. Anglada-Escudé et al., 2016; Gillon et al., 2017). Debris disks around M dwarfs should have the same informative powers as their higher-mass-star cousins. The recent discovery of cold debris around the M dwarf exoplanet host Proxima Centauri with ALMA (Anglada et al., 2017) may yield valuable insights into the structure of that planetary system, though a recent re-analysis indicates that much of the flux previously attributed to dust can be attributed to a large flare (MacGregor et al., 2018).

However, the current sample of M dwarf debris disk systems has significant shortcomings. Only $\sim 2\%$ of dM stars are currently known to host debris disks (e.g. Deacon et al., 2013; Theissen & West, 2014; Binks & Jeffries, 2017; Boucher et al., 2016; Silverberg et al., 2016), less than the $\sim 14\%$ expected from the mass distribution of primordial disks, and much less than the 20% fraction of A dwarfs with known disks (Greaves, 2010). As part of our application of Disk Detective analysis to other surveys, we began a re-analysis of imagery of the M dwarf disk candidates presented in Theissen & West (2014), one of the largest lists of M dwarf disk candidates from WISE published to date.

These disk candidates generally suffer from low signal-to-noise at W4. Of the 175 disk candidates presented in Theissen & West (2014), only three meet the Disk Detective input catalog criterion of `w4snr` > 10. By contrast, 152 of the 175 only have upper limit magnitudes at W4 due to `w4snr` < 2, as per the AllWISE data release quality flags. In most cases, W4 postage stamp images only show background emission, without a coherent point source at W4. This is presumably due in combination to the shallowness of the W4 band, and the distance of these targets.

Because of this lack of a point source, the Disk Detective classification method

fails for the majority of these targets. Due to the shallowness of W4 compared to the other three WISE bands, Theissen & West (2014) primarily focused on significant excess at W3, noting that those targets with `w4snr` > 3 and excess at W4 also exhibited excess at W3. However, the Disk Detective method is still viable for the 13 targets with `w4snr` > 3.

We downloaded 1-arcminute postage-stamp images of the Theissen & West (2014) disk candidates from the IRSA finder chart, using a similar blue-white color scale to that used on the Disk Detective website, and applied a 12-arcsecond radius red circle to these images to effectively generate Disk Detective flipbooks of these targets. Our team of advanced users then analyzed these targets as if they appeared on the Disk Detective website and cataloged their assessment of these objects in the Disk Detective website categories. All thirteen objects with `w4snr` > 3 were classified as extended by a majority of classifiers. Five of the thirteen were also majority-classified as multiple, and two were also majority-classified as oval.

The disk candidates identified by the Theissen & West (2014) M dwarf survey typically do not meet the Disk Detective standard for inclusion for analysis; the thirteen that meet these standards are clear false positives that do not survive Disk Detective's by-eye examination. It is possible that the remaining 162 M dwarf disk candidates, with significant W3 excess and low signal-to-noise at W4, could represent a class of hot, distant debris disks for which Disk Detective is not designed. However, given the high false positive rate of objects that can be assessed with the Disk Detective methodology, we recommend treating these results with caution.

2.7 New Disk Candidates

Based on our follow-up observations with Robo-AO and Dupont/Retrocam, we find that 244 of our observed targets, including 214 sources first identified by Disk Detective, have no significantly contaminating background objects within the 12″ radius of the W4 PSF, giving us the confidence to publish them as disk candidates. The candidates are listed in Table 2.4; previous surveys that have also identified these targets are listed in the Notes column. We briefly summarize characteristics of some objects of particular interest in Appendix A.3.

We used available photometry from SIMBAD, 2MASS, and WISE (including corrected W1, W2, and W4 photometry) to fit the spectral energy distributions (SEDs) of these systems. We initially fit the stellar component of the system with a blackbody to estimate the stellar temperature and ratio of stellar radius to distance. In the case where a blackbody fit yields a temperature less than 7000K, we instead fit with a stellar model from the BT-Settl CIFIST package (Baraffe et al., 2015), also fitting for $\log(g)$. We initially fit the three bluest photometry points, then refit including the next bluest point if it is not in significant excess, repeating the last step iteratively until the next point is either W3 or in excess. We fit the remaining excess using a single-temperature blackbody to determine the dust temperature. We then find the best fit parameters using the `emcee` package (Foreman-Mackey et al., 2013), using the previous parameter estimates as an initial guess. These SEDs, shown in Figure 2.6, provide a useful first-order estimate of these fundamental disk parameters. We list these parameters for likely debris disks in Table 2.5, and for likely YSO disks in Table 2.6. Table 2.5 consists of all candidates with only one point of excess (W4), as well as candidates with two points of excess and $L_{\rm ir}/L_\star < 10^{-3}$. Table 2.6 consists of all other objects. For objects with more than two points of excess, we also provide the spectral index α

Table 2.4. Disk Candidates

Identifiers			Sp.	Distance[b]	Magnitudes				
Zooniverse	HD	WISEA	Type[a]	(pc)	Vmag[c]	Jmag	W1mag	W4mag	Notes
AWI0000gib	1777	J002133.47-661816.6	A0V	163 ± 10	7.361 ± 0.010	7.365 ± 0.027	7.356 ± 0.027	6.793 ± 0.066	
AWI0006251		J002155.14-672715.9		789 ± 231	10.75 ± 0.06	9.008 ± 0.023	8.253 ± 0.022	6.655 ± 0.065	
AWI00062lo	2830	J003140.76-014737.3	A0V	109 ± 6	7.07 ± 0.01	6.917 ± 0.019	6.841 ± 0.033	5.832 ± 0.049	a,b
AWI0005mry	3051	J003412.66+540359.0	A1V	213 ± 15	7.595 ± 0.010	7.350 ± 0.019	7.346 ± 0.049	6.881 ± 0.067	a
AWI0000jvv		J003507.14+070625.0				8.142 ± 0.019	6.937 ± 0.033	4.923 ± 0.035	c
AWI00062m4		J004826.42+020753.0		535 ± 213	10.264 ± 0.046	8.490 ± 0.026	7.687 ± 0.024	5.392 ± 0.043	c
AWI0005yiv	5741	J005926.26+400918.2		113 ± 4	7.532 ± 0.010	7.170 ± 0.018	7.139 ± 0.031	6.651 ± 0.054	
AWI00055sx	6370	J010652.55+743754.5	B9IV	354 ± 39	8.368 ± 0.012	8.168 ± 0.029	8.149 ± 0.023	7.139 ± 0.087	a

[a]Spectral types are from SIMBAD, with the exception of sources that appear in Paper 1. For those sources, we use the spectral types published in that paper.

[b]Distances are based on parallax measurements from *Hipparcos* or TGAS, as listed on SIMBAD.

[c]Sourced from SIMBAD.

Note. — (a) Appears in Paper 1. (b) Listed as a comoving object in Oh et al. (2017). (c) Listed in the K2 Ecliptic Plane Input Catalog. (d) Listed in Chen et al. (2016). (e) Identified in Vieira et al. (2003). (f) Identified in Corbally & Straižys (2009). (g) Identified in Cotten & Song (2016). (h) Identified in Esplin et al. (2014). (i) Identified in Rebull et al. (2011). (j) Identified in Wu et al. (2013). (k) Identified in Guieu et al. (2010). (l) Identified in Koenig et al. (2015). (m) Identified in Hernández et al. (2005). (n) Identified in Alcala et al. (1996). (o) Identified in Rojas et al. (2008). (p) Identified in Sanchez et al. (2014). (q) Identified in Rebull et al. (2000). (r) Identified in Megeath et al. (2012). (s) Identified in Luhman et al. (2008). (t) Identified in Rapson et al. (2014). (u) Identified in Rizzuto et al. (2012). (v) Identified in Chen et al. (2012). (w) Identified in Chen et al. (2014). (x) Identified in Melis et al. (2013). (y) Identified in Evans et al. (2009). (z) Identified in Evans et al. (2003). (α) Identified in Cruz-Saenz de Miera et al. (2014). (β) Identified in Clarke et al. (2005). (γ) Identified in Kennedy & Wyatt (2013). (δ) Identified in Patel et al. (2014). (ϵ) Identified in Barentsen et al. (2011).
Table 2.4 is published in its entirety in the machine-readable format. A portion is shown here for guidance regarding its form and content.

of a power-law fit to the object's WISE data as an estimate of YSO class.

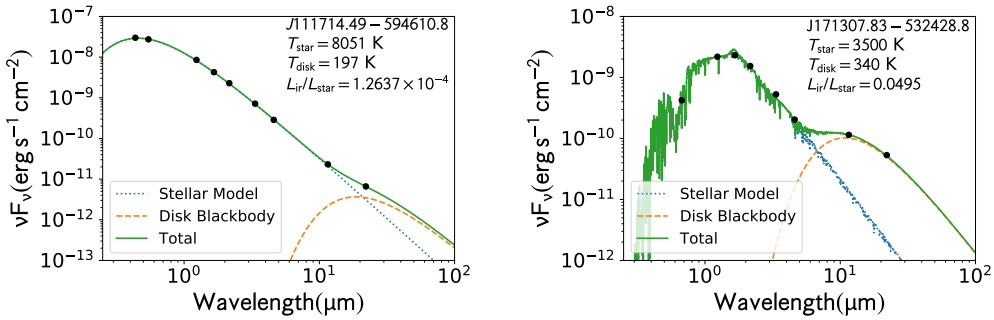

Figure 2.6: Sample SEDs for two of the 244 systems presented here. Plotted are Johnson B and V magnitudes based on *Tycho* photometry (sourced from SIMBAD), 2MASS, and WISE (black circles). Uncertainties in these measurements are typically smaller than the plotting symbol. The best-fit combined model is plotted in green along with each of the model components (photosphere in blue dots, single-temperature dust blackbody as dashed orange). Model stellar temperature, blackbody temperature, and fractional infrared luminosity are listed in the top right corner of each panel. SEDs for the entire sample are available in the online version of the article.

Of the 244 targets presented here, 223 have parallax measurements from *Hipparcos* or the second data release from *Gaia*, listed in Table 2.4. The parallax measurements indicate that 31 of these systems lie within 125 pc, making them prime candidates for follow-up observation. We list these candidates in Table 2.7.

Table 2.5. Derived Parameters of Debris Disk Candidates

Zooniverse	WISEA	$T_{\rm eff}$ (K)	$T_{\rm disk}$ (K)	$L_{\rm ir}/L_{\rm star}$
AWI00062h7	J002133.47-661816.6	11697^{+112}_{-113}	216^{+27}_{-24}	$(2.8 \pm 0.4) \times 10^{-5}$
AWI0000bs0	J003140.76-014737.3	10319^{+64}_{-69}	202 ± 11	$(8.6 \pm 0.6) \times 10^{-5}$
AWI0005mry	J003412.66+540359.0	9680 ± 72	> 35	< 0.12
AWI0005yiv	J005926.26+400918.2	9165^{+58}_{-52}	> 46	< 0.005
AWI00055sx	J010652.55+743754.5	10106^{+80}_{-85}	182^{+16}_{-15}	$(8.1 \pm 1.1) \times 10^{-5}$
AWI00055sz	J011636.23+740136.6	9011^{+99}_{-89}	685^{+125}_{-113}	$(4.5^{+2.0}_{-1.3}) \times 10^{-4}$

Note. — Table 2.5 is published in its entirety in the machine-readable format. A portion is shown here for guidance regarding its form and content.

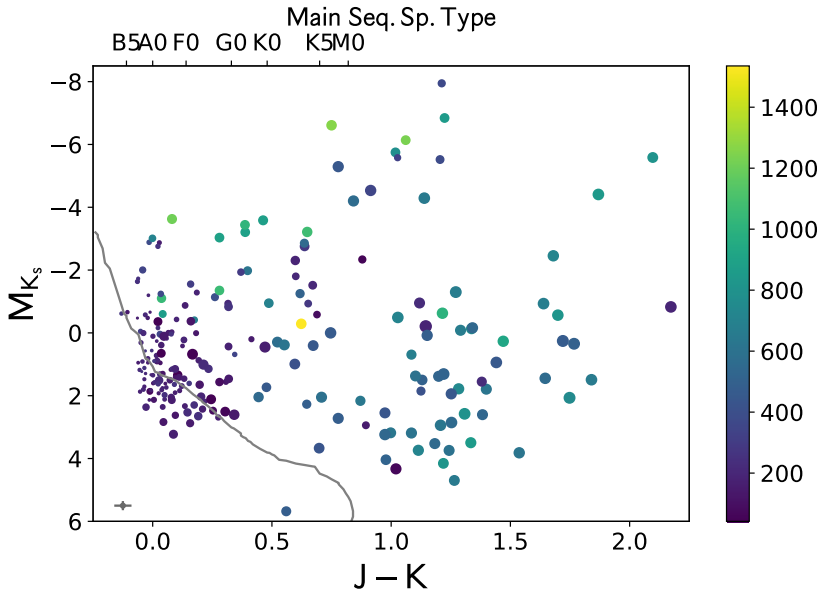

Figure 2.7: 2MASS $(M_K, J-K)$ color-magnitude diagram of 223 disk candidates with parallax measurements. Point color corresponds to disk temperature, while point size corresponds to $L_{\rm ir}/L_{\rm star}$. 148 disk candidates lie within 1.5 mag of the zero age main sequence (gray line), and 126 lie within 1.5 mag of the zero age main sequence with spectral type earlier than G0. Main sequence spectral types are listed across the top for reference. The point in grey in the lower left indicates typical uncertainties, ~ 0.04 mags in (J-K) color and ~ 0.15 mags in M_K.

Table 2.6. Derived Parameters of YSO Disk Candidates

Zooniverse	WISEA	$T_{\rm eff}$ (K)	$\alpha_{\rm disk}$	$T_{\rm disk}$ (K)	$L_{\rm ir}/L_{\rm star}$
AWI0000nfp	J002155.14-672715.9	4700 ± 100		509 ± 21	$(7.7 \pm 0.05) \times 10^{-3}$
AWI0000jvv	J003507.14+070625.0	3500 ± 100		368^{+12}_{-11}	$(1.23^{+0.05}_{-0.04}) \times 10^{-2}$
AWI00062m4	J004826.42+020753.0	4600 ± 100		207^{+5}_{-4}	$(3.7^{+0.1}_{-0.1}) \times 10^{-3}$
AWI00062mq	J011743.47-523330.8	6400 ± 100	-0.12 ± 0.01	436 ± 4	$(9.0 \pm 0.2) \times 10^{-2}$
AWI0005aeg	J013833.77+780834.3	6700 ± 100	-2.11 ± 0.02	1210^{+26}_{-25}	$(2.5^{+0.2}_{-0.1}) \times 10^{-2}$

Note. — Table 2.6 is published in its entirety in the machine-readable format. A portion is shown here for guidance regarding its form and content.

Table 2.7. Disk Candidates Within 125 Pc

Zooniverse	WISEA	Distance(pc)	V Magnitude	$T_{\rm eff}$ (K)	$T_{\rm disk}$ (K)	$L_{\rm ir}/L_{\rm star}$
AWI00062lo	J003140.76-014737.3	109 ± 6	7.07 ± 0.01	10311^{+65}_{-62}	202^{+11}_{-10}	$8.5(^{+0.54}_{-0.58}) \times 10^{-5}$
AWI0005yiv	J005926.26+400918.2	113 ± 4	7.532 ± 0.01	9169 ± 57	59^{+29}_{-17}	$7.4(^{+140}_{-6.4}) \times 10^{-4}$
AWI000425z	J024755.37+553648.4	99 ± 3	6.918 ± 0.01	9490^{+66}_{-67}	131^{+38}_{-43}	$4.2(^{+4.7}_{-0.82}) \times 10^{-5}$
AWI0000phh	J025614.05+040254.2	125 ± 21	7.706 ± 0.014	11304^{+122}_{-120}	215^{+16}_{-14}	$6.4(^{+0.60}_{-0.62}) \times 10^{-5}$
AWI0005yk3	J030651.95+303136.8	73 ± 3	7.061 ± 0.011	7640^{+46}_{-44}	243 ± 5	$7.5(\pm 0.20) \times 10^{-4}$
AWI0005ykd	J032448.99+283908.6	106 ± 6	7.121 ± 0.01	9537^{+71}_{-60}	118 ± 38	$5.5(^{+11}_{-1.4}) \times 10^{-5}$
AWI0005zy4	J032504.59+105835.0	116 ± 5	7.294 ± 0.011	9493^{+69}_{-71}	182^{+37}_{-51}	$3.4(^{+0.85}_{-0.70}) \times 10^{-5}$
AWI00062iw	J032555.87-355515.1	100 ± 6	6.385 ± 0.009	10160^{+86}_{-81}	216^{+22}_{-21}	$4.1(^{+0.42}_{-0.39}) \times 10^{-5}$
AWI0005ym9	J035157.43+255955.4	121 ± 9	7.68 ± 0.01	9135^{+49}_{-48}	158^{+44}_{-63}	$3.9(^{+2.9}_{-1.1}) \times 10^{-5}$
AWI0005ymc	J040040.65+202447.8	119 ± 5	8.05 ± 0.01	8410 ± 46	131^{+5}_{-6}	$5.7(^{+0.42}_{-0.35}) \times 10^{-4}$
AWI0005zz5	J040238.47-004803.7	123 ± 8	6.93 ± 0.1	11167^{+81}_{-80}	176^{+20}_{-24}	$3.4(^{+0.47}_{-0.43}) \times 10^{-5}$
AWI0005ymi	J041249.03+193219.2	115 ± 5	7.783 ± 0.014	6100 ± 100	175^{+14}_{-15}	$2.3(^{+0.21}_{-0.19}) \times 10^{-4}$
AWI0005wcl	J045519.57+163712.9	109 ± 8	7.17 ± 0.01	10127^{+81}_{-80}	214^{+21}_{-18}	$5.1(\pm 0.58) \times 10^{-5}$
AWI0005d88	J083100.44+185806.0	91 ± 4	7.418 ± 0.012	8319^{+47}_{-51}	45^{+20}_{-10}	$1.0(^{+20}_{-0.96}) \times 10^{-2}$
AWI0000y1k	J111714.49-594610.8	76 ± 1	7.15 ± 0.01	8048^{+52}_{-51}	195^{+17}_{-16}	$1.3(^{+0.099}_{-0.096}) \times 10^{-4}$
AWI0005da8	J112256.98-203731.7	114 ± 5	7.466 ± 0.011	8835^{+64}_{-59}	132^{+42}_{-48}	$5.6(^{+8.7}_{-1.3}) \times 10^{-5}$
AWI00056ck	J121456.32-475654.6	117 ± 5	8.097 ± 0.011	7889^{+47}_{-48}	150^{+7}_{-8}	$3.3(^{+0.20}_{-0.18}) \times 10^{-4}$

We can also use these parallaxes and 2MASS photometry to construct an HR diagram for our disk candidates (shown in Figure 2.7). On this figure, point color corresponds to disk temperature, while point size corresponds to $L_{\rm ir}/L_\star$. A gray curve shows the zero-age main sequence (Pecaut & Mamajek, 2013). The point in gray in the lower left indicates typical uncertainties, ~ 0.04 mags in $(\mathrm{J} - \mathrm{K_s})$ color and ~ 0.15 mags in $M_{\mathrm{K_s}}$. Although some stars have K-band excesses that shift their points to the right in this diagram, Figure 2.7 reveals that none of the host stars with parallaxes has a main-sequence type later than roughly K7. Even with our "drain-the-lake" approach to searching for debris disks, the M dwarf disks remain hidden, at least in this sample.

The diagram also reveals some potentially interesting outliers. The yellow point near the center of the figure is WISEA J191845.28+371449.2. This star, listed in SIMBAD as an A2 at a distance of 573 pc, has excess flux in all three 2MASS bands and all four WISE bands, which is well modeled by a single-temperature blackbody at 1535 K with $L_{\rm ir}/L_\star = 0.0647$ (Figure 2.8). The star lies roughly 0.7 mag to the right of the zero-age main sequence primarily because of its K_s excess of 0.623 mag. If this star is indeed a main sequence star with a debris disk as its SED fit suggests, this system would be an example of an "extreme debris disk" (Meng et al., 2015; Theissen & West, 2017), i.e., a signpost of a recent giant impact. Given the lack of an additional mid-IR-driven excess, this object could also be an example of a precursor to a two component system with a hot debris disk (Akeson et al., 2009), where a gap has not yet been cleared between the two components. However, Gaia DR2 indicates that this object could be super-luminous for a spectral type of $\sim$A2 (the expected spectral type for the SED-fit stellar temperature), and optical spectroscopy indicates that this object could instead be a weak-lined Herbig Ae star (Bans et al. 2018, in prep). Additional follow-up with radio/sub-millimeter observations would be necessary to

Table 2.7 (cont'd)

Zooniverse	WISEA	Distance(pc)	V Magnitude	$T_{\rm eff}$ (K)	$T_{\rm disk}$ (K)	$L_{\rm ir}/L_{\rm star}$
AWI00056i5	J132026.77-491325.4	116 ± 4	7.948 ± 0.012	8213^{+57}_{-55}	172^{+13}_{-14}	$1.3(^{+0.095}_{-0.093}) \times 10^{-4}$
AWI0000uji	J151147.67+101259.8	117 ± 6	6.875 ± 0.012	10812^{+100}_{-99}	278^{+38}_{-29}	$3.7(^{+0.50}_{-0.49}) \times 10^{-5}$
AWI0000v1z	J152954.11+234901.6	114 ± 4	7.585 ± 0.011	8576^{+49}_{-51}	47^{+35}_{-13}	$3.1(^{+160}_{-3.0}) \times 10^{-3}$
AWI00057qr	J164548.44-263858.1	108 ± 6	7.02 ± 0.011	10863^{+104}_{-97}	193^{+11}_{-10}	$7.8(\pm 0.54) \times 10^{-5}$
AWI00002yt	J172007.53+354103.6	101 ± 2	8.272 ± 0.012	6800 ± 100	196 ± 30	$9.0(\pm 1.5) \times 10^{-5}$
AWI0005igi	J172452.23-185133.5	98 ± 3	8.5 ± 0.015	6200 ± 100	91^{+13}_{-17}	$2.3(^{+3.0}_{-0.71}) \times 10^{-3}$
AWI0005d5p	J180230.72+583738.4	89 ± 4	6.858 ± 0.01	9659 ± 75	152^{+35}_{-45}	$3.3(^{+1.3}_{-0.44}) \times 10^{-5}$
AWI000621a	J205241.67-531624.8	63 ± 1	7.663 ± 0.011	6300 ± 100	47^{+23}_{-10}	$1.3(^{+21}_{-1.2}) \times 10^{-2}$
AWI0006222	J210916.04-001405.6	103 ± 9	6.659 ± 0.01	9118^{+60}_{-55}	171^{+24}_{-32}	$5.4(^{+0.65}_{-0.51}) \times 10^{-5}$
AWI00019i2	J221055.01+575629.4	112 ± 4	7.42 ± 0.01	8824^{+52}_{-54}	261^{+21}_{-20}	$8.4(^{+0.82}_{-0.79}) \times 10^{-5}$
AWI0000gjb	J224206.62-032824.4	112 ± 12	7.159 ± 0.011	11159^{+100}_{-98}	180^{+19}_{-21}	$3.8(^{+0.42}_{-0.40}) \times 10^{-5}$
AWI00062gs	J230533.05+145732.5	124 ± 12	6.762 ± 0.01	11596 ± 102	162^{+19}_{-24}	$3.3(^{+0.48}_{-0.40}) \times 10^{-5}$
AWI00062l3	J235537.71+081323.7	113 ± 8	6.818 ± 0.01	11396^{+109}_{-105}	269^{+37}_{-29}	$3.2(^{+0.41}_{-0.40}) \times 10^{-5}$
AWI00062h1	J235746.21+112827.6	102 ± 6	6.644 ± 0.01	11092^{+92}_{-96}	205 ± 27	$2.6(^{+0.36}_{-0.35}) \times 10^{-5}$

confirm whether this object hosts a warm debris disk, or instead has the expected substantial cold material reservoir of a Herbig Ae system.

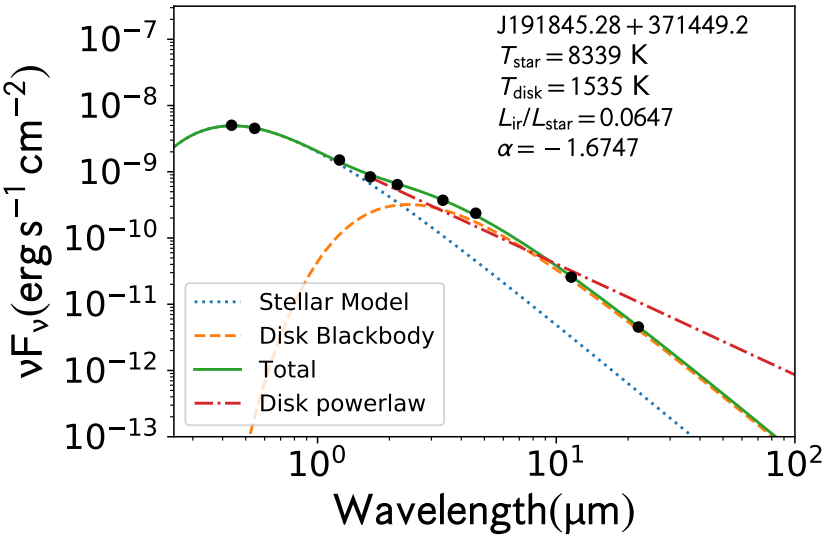

Figure 2.8: SED for WISEA J191845.28+371449.2. This system is well fit by a stellar temperature blackbody with a $\sim$ 1535 K disk blackbody with fractional infrared luminosity $\sim$ 0.065, suggesting an extreme debris disk.

Zuckerman (2015) noted the high frequency of warm dust disks occurring around stars that were members of binary systems. Oh et al. (2017) specifically searched for new comoving pairs and systems in the Tycho-Gaia Astrometric Solution (TGAS; Gaia Collaboration et al., 2016; Lindegren et al., 2016). Out of 619,618 stars searched, they identified 8,472 stars as members of comoving pairs, and a further 2,134 as members of larger comoving systems. We note that 27 of our disk candidates presented here appear as members of comoving systems in Oh et al. (2017) (listed in Table 2.4), out of 105 with parallax data sufficient for inclusion in the Oh et al. (2017) survey. Twelve of these 105, or 11% $\pm$ 3%, are members of comoving pairs only, significantly higher than the overall rate of 1.37% found by Oh et al. (2017). This significantly higher rate contributes further support to the hypothesis of Zuckerman (2015).

We tested the likelihood of moving group membership for each of the new disk

candidates we present here using BANYAN Σ (Gagné et al., 2018), and compared our targets with previous moving group membership determinations. We present the first 22 μm excess detection around J111714.49-594610.8, a known member of the Lower Centaurus Crux (LCC). Testing its kinematics with BANYAN Σ, however, indicates a 44.9% probability of membership in LCC, and a 40.5% probability of membership in Carina. We also note the first detection of an infrared excess around J140353.79-534628.3, a known Sco-Cen member (Hoogerwerf, 2000) for which BANYAN Σ yields an 88.9% chance of membership in the Upper Centaurus-Lepus complex (UCL). We find that J164540.79-310226.6, a star with infrared excess previously detected by Cruz-Saenz de Miera et al. (2014), has a 96.9% probability of membership in UCL. These determinations give us age benchmarks for these systems, allowing us to compare them to disk evolutionary models. Identification of disks in moving groups has yielded unexpected and valuable results with regard to theories of disk evolution, such as the identification of a primordial disk around an M dwarf in the Carina association, at an age 9 times greater than the e-folding time for primordial disk dissipation around solar-type stars (Silverberg et al., 2016; Murphy et al., 2018).

Most of our published targets do not yet have spectroscopically-determined spectral types or luminosity classes, and many do not have measured distances. An ongoing spectroscopic follow-up campaign of DDOIs (Bans et al., in prep) will present a more complete and more detailed analysis of the distribution of spectral types of our objects.

Between this paper, Paper 1, and Silverberg et al. (2016), Disk Detective has now published 215 previously-unidentified disk candidates. Of the 144 with either published spectral types or known parallaxes, the majority (110) are early-type main sequence stars. 125 of the 215 have disk temperatures $T_{\rm disk} < 300$ K, and disk

temperatures range up to 1800 K. A majority of these disks (114) have fractional infrared luminosities $L_{\rm ir}/L_\star > 10^{-3}$, suggesting that these are likely primordial disks, per the criterion suggested by Williams & Cieza (2011); many of these do not appear in our previous HR diagram because they lack parallax measurements. The characteristics of this sample overall suggest that while designed to identify debris disks, Disk Detective also effectively locates new primordial disks.

2.8 Summary

In this paper, we presented the results of follow-up imaging of 261 Disk Detective Objects of Interest, determining whether background contaminants appeared and whether they significantly impacted the infrared excess around these objects observed with WISE. We find that background objects, while apparent in the images, significantly affect the observed excess at a rate of $\sim 6\%$. Combining these data with false-positive rates from classifications and literature review, we find that AllWISE should yield $\sim 21,600$ high quality disk candidates based on excess at 22 μm. Applying this result to other surveys, we estimate that $4-8\%$ of published disk candidates from high-quality surveys may have background objects in follow-up high-resolution imaging bright enough to significantly affect the detected excess. Based on our expected yield of disks from AllWISE, we found that the searches of McDonald et al. (2012), McDonald et al. (2017), and Marton et al. (2016) have lower-limit false positive rates greater than 70%. We considered the 175 disk candidates of Theissen & West (2014), and found that the vast majority of these candidates would not be detected by Disk Detective due to insufficient signal-to-noise at W4. All thirteen targets in the Theissen & West (2014) search with W4 SNR sufficient for the Disk Detective methodology to apply were false-positive identifications after visual inspection.

We presented a sample of 244 disk candidates, vetted through visual inspection by citizen scientists and high-resolution follow-up imaging to refine the observed excess. Disk Detective has now published 215 newly-identified disk systems, of which 114 have fractional infrared luminosities indicative of primordial disks (either full protoplanetary or transitional). We find twelve of our disk candidates to be in comoving pairs, providing further support for the hypothesis of Zuckerman (2015) that there is a causal relationship between a distant companion and a warm dusty debris disk. We identified one system, WISEA J191845.28+371449.2, as a likely "extreme" debris disk, based on its high fractional infrared luminosity. Thirty-one of these systems lie within 125 pc, including 27 debris disks. These nearby disk systems are good targets for adaptive-optics and coronagraphic imaging to directly image exoplanets in orbit around the host star.

High-resolution follow-up imaging can eliminate many false positives, but it will not eliminate not-yet-identified spectroscopic false-positive detections of primordial and debris disks (e.g. previously-unidentified dust-producing M giants, AGN, classical Be stars). A spectroscopic follow-up program to identify these sorts of false positives is ongoing. The results presented here should be used in conjunction with the results of that program (Bans et al., in prep) to determine the expected yield of AllWISE.

Chapter 3

A New M Dwarf Debris Disk Candidate in a Young Moving Group Discovered with Disk Detective*

3.1 Introduction

Young moving groups and associations (YMGs) provide highly valuable targets for exoplanet searches and important tracers of disk evolution (Zuckerman & Song, 2004; López-Santiago et al., 2006). The stars in YMGs share similar ages, and their motions through the Galaxy trace back to a common origin locus. Exoplanets around stars in YMGs are often young and warm enough to be observed via near-infrared direct imaging with large telescopes (e.g. Marois et al., 2008; Currie et al., 2014). Additionally, the well-determined ages of YMG members allow us to place any planets and disks discovered around them in a chronological sequence, tracing the evolution of planetary systems.

YMGs have driven many studies of disk evolution. Based on *Spitzer* data and disk models of objects in the Taurus cloud and Ophiuchus, Espaillat et al. (2010) proposed that the gaps in pre-transitional disks were indicators of planet formation. Mid- (24 μm) and far-IR (70 μm) observations of moving group A stars from *Spitzer*/MIPS show that disks around older stars have a narrower temperature distribution than younger stars, and that 70 μm disk emission persists longer than 24 μm emission (Su et al., 2006). Kennedy & Wyatt (2010) modeled the potential self-stirring behavior of disks and applied it to A-stars in the β Pictoris moving

*The contents of this chapter were previously published in Silverberg et al. (2016).

group and the TW Hya association. Further observations and analysis of archival data of the Tucana/Horologium, AB Doradus, Columba, and Argus associations with *Spitzer* (Zuckerman et al., 2011) characterized the appearance of debris disks around YMG stars, and constrained the decay of dusty debris disks over time.

In recent years, many direct-imaging exoplanet and disk surveys have focused on YMG members. Kasper et al. (2007) primarily surveyed the Tucana-Horologium and β Pictoris moving groups in their direct imaging search for Jupiter-mass sub-stellar companions. Biller et al. (2013) directly imaged 80 members of the β Pictoris, TW Hya, Tucana-Horologium, AB Doradus, and Hercules-Lyrae YMGs in a survey for giant planets as part of the Gemini/NICI Planet-Finding Campaign, finding four co-moving companions and constraining the frequency of 1-20 $M_{\rm Jup}$ planets at separations up to 150 AU. The Strategic Exploration for Exoplanets and Disks with Subaru (SEEDS) survey included a dedicated focus on potential moving group members (Brandt et al., 2014), using high-contrast coronagraphic imaging to observe many targets identified with YMGs. Currie et al. (2015) identified a Kuiper belt-like debris disk in the Scorpius-Centaurus association with the Gemini Planet Imager as part of a larger survey.

The Wide-field Infrared Survey Explorer (WISE) mission (Wright et al., 2010), the most sensitive all-sky mid-infrared survey to date, provides the best source of new YMG candidate members with infrared excess across the sky. Some past WISE studies to identify late-type YMG candidate members with infrared excess have generally proceeded by first identifying likely members, then examining WISE data to see if they have infrared excesses (e.g. Schneider et al., 2012a,b). Other WISE studies of YMG candidate membership of earlier-type stars have used the presence and strength of infrared excess in WISE data as a component in their membership determination (e.g. Rizzuto et al., 2012). We instead first identify stars with infrared excesses, and then test each one for membership in a

YMG.

We report here one newly identified candidate YMG member with infrared excess discovered by the Disk Detective project (Kuchner et al., 2016, hereafter Paper 1). This star has $> 90\%$ membership probability in a YMG based on the BANYAN II Bayesian analysis tool (Malo et al., 2013; Esplin et al., 2014). Distance estimates (< 88 pc) suggest that this star is a good target for direct imaging.[1] We also recover a previously-identified YMG candidate member with a known infrared excess.

In Section 2 of this paper, we summarize our methodology for identifying and modeling stars with excesses and determining their YMG membership probability in more detail. In Section 3, we present our candidate member, discuss its stellar characteristics, compare its kinematics to its association, and characterize basic parameters of the star and its infrared excess. In Section 4, we summarize our findings and discuss the outlook for future identifications in this manner, in light of the upcoming release of results from the *Gaia* mission (Perryman et al., 2001).[2]

3.2 Methodology

The objects with identified infrared excesses come from the Disk Detective project (Paper 1; `http://www.diskdetective.org`), a citizen science-based all-sky search for circumstellar disks in the AllWISE Data Release (Cutri & et al., 2013). Unlike other *WISE* debris disk searches, Disk Detective is not limited to the *Hipparcos* or *Tycho* catalogs, which are magnitude-limited in V and thus omit a wide swath of mid- and late-type stars. It instead searches the entire 2MASS catalog (Skrutskie et al., 2006) for objects with [W1] - [W4] > 0.25 that meet other criteria designed

[1] Since the original publication of this work, this system's parallax was observed in *Gaia* DR2. Its measured distance is 101.42 ± 0.57 pc.

[2] Since initial publication of this text, *Gaia* DR2 has been released. A discussion of the *Gaia* data for this object appears in Chapter 4.

to eliminate contaminants and other sources of noise. The DiskDetective.org website aims to harvest Disk Detective Objects of interest (DDOIs), sources we consider to be worthy of further research. DDOIs are then submitted for follow-up observation on ground- and space-based telescopes. Details on the identification of DDOIs can be found in Paper 1. As of 25 April, 2016, DiskDetective.org users had identified 1774 DDOIs, a unique new collection of potential debris disks.[3]

To test the likelihood of YMG membership for these objects, we used Bayesian Analysis for Nearby Young AssociatioNs II (BANYAN II; Malo et al., 2013; Esplin et al., 2014). This tool uses a naive Bayesian classifier to compare the Galactic position and space velocity of a given object to the positions and velocities of several well-defined moving groups and associations with distances < 100 pc and ages < 200 Myr: the β Pictoris, AB Doradus, and TW Hya moving groups, as well as the Argus, Columba, Carina, and Tucana-Horologium associations. BANYAN II takes as inputs an object's right ascension, declination, trigonometric parallax, radial velocity, and proper motion. We tested 1774 DDOIs with BANYAN II, using spatial coordinates from AllWISE, and parallax and proper motions from *Hipparcos* (ESA, 1997) or the Tycho-Gaia Astrometric Solution (TGAS, Lindegren et al., 2016) whenever available. When parallax and proper motion data from these surveys were not available, we used proper motion data from other surveys, such as the Tycho-2 bright star catalog (Høg et al., 2000), or the SPM4 catalog (Girard et al., 2011).

We used an algorithm based on the implementation of the Levenberg-Marquardt minimization scheme in the Python `lmfit` package to estimate basic parameters of the host star and disk of our YMG candidates. Our algorithm cycles through combinations of $T_{\rm eff}$ and $\log(g)$, fitting the corresponding BT-Settl stellar atmo-

[3]After this chapter was originally published, we revised our definitions of DDOIs to exclude well-studied disks, e.g. those with images from *Spitzer*. The number of DDOIS listed in the database as of 3 April, 2019, is 1,738, though some records are still being entered.

sphere model (Baraffe et al., 2015) to 2MASS J, H, and K, WISE W1, and any additional large-survey photometry (e.g. the Tycho2 catalog or the DENIS survey (Epchtein et al., 1997)) to find a best-fit ratio of stellar radius to distance. We adopt the best-fitting of these models, yielding estimates of the stellar temperature $T_\star$ and distance. Taking this distance and stellar model into account, the algorithm then fits the four bands of WISE photometry with a Planck function, representing a single-temperature disk. The parameters from these two fits are then used to derive a value for the disk's fractional infrared luminosity, $L_{ir}/L_\star$.

3.3 Results

From our initial sample of 1774 DDOIs, we identified one star with $> 90\%$ likelihood of membership in a YMG, with significant excess [W1]-[W4]> 0.25. As this system was not included in either the *Hipparcos* survey, or the late-M surveys for BANYAN (Malo et al., 2013; Esplin et al., 2014), its membership candidacy has not been evaluated until now. We initially identified WISE J060652.79-313054.1, an F8 star, as a member of the Columba association, based on position and proper motion measurements. and estimated the distance to the star via spectroscopic parallax, independent of the BANYAN II calculation. However, when we incorporated the parallax measurement from TGAS into the BANYAN II analysis, the membership probability dropped from 93.77% to 0.73%, indicating that the detection was due to incomplete information. We also recovered TWA 33, which was previously reported in Schneider et al. (2012b). Here, we briefly discuss the characteristics of this new dusty YMG member.

3.3.1 J080822.18-644357.3

This star has no previously-reported parallax or radial velocity measurements. It does have proper motion observations from the Southern Proper Motion 4.0 (SPM4.0) survey (Girard et al., 2011). Based on this data, it has a 93.9% probability of membership in the Carina association. This association was first identified as part of the Great Austral Young Association by Torres et al. (2003, 2006), but was later identified as a separate association by Torres et al. (2008). The association has age 45^{+11}_{-7} Myr (Bell et al., 2015), and distance range 46-88 pc (Malo et al., 2013, and references therein). Examination of the star's Galactic position and velocity relative to that group (shown in Figure 3.1) indicates that while it is centrally located in the group at the most probable radial velocity and parallax from BANYAN II, its velocity is not as typical; its three-dimensional velocity falls outside the 68% confidence bubble for the group, indicated by the faint red ellipsoid in Figure 3.1. However, it is not a particularly extreme outlier; the 1σ error bars on the star's velocity intersect with the ellipsoid.

As seen in Figure 3.2, this star exhibits a significant excess at both W3 ([W1] - [W3] = 2.367 ± 0.036) and W4 ([W1] - [W4] = 4.234 ± 0.087), suggesting a fairly warm disk around a fairly cool star. While this star does not have a previously-reported spectral type, we use photometry from 2MASS, AllWISE, and the DENIS survey (Epchtein et al., 1997) to find a best-fit BT-Settl stellar atmosphere with $T_\star = 2900$ K, consistent with a spectral class of M5.5V based on the models used by Rajpurohit et al. (2013). Using this adopted spectral type and an absolute 2MASS J magnitude for this model of 9.21, we find a distance based on spectroscopic parallax of ~ 57 pc, which reasonably agrees with the most probable distance from BANYAN II. We find values for the disk of $T_{\rm disk} \sim 263$ K, and $L_{ir}/L_\star = 8.06 \times 10^{-2} \pm 9.02 \times 10^{-3}$. These high values of $L_{ir}/L_\star$ and $T_{\rm disk}$ suggest

a young star, independent of its YMG candidacy. The high blackbody temperature of the disk also suggests a close-in disk, with an inner disk radius of ~ 0.074 AU, approximately 1.5 times the semi-major axis of the orbit of Proxima Centauri b (Anglada-Escudé et al., 2016).

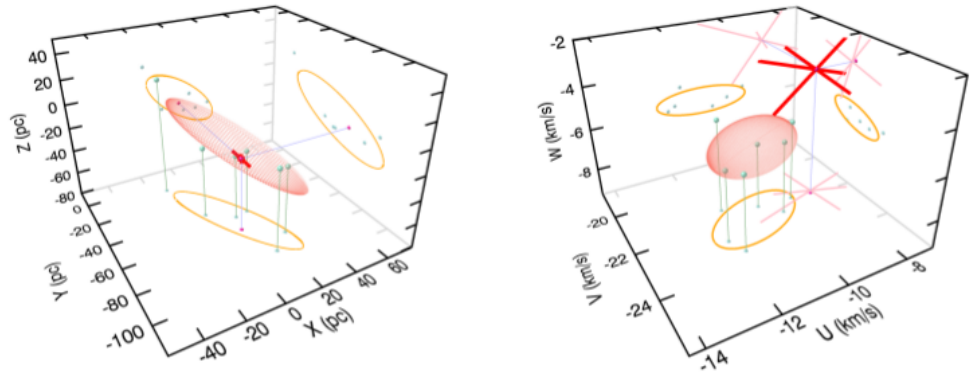

Figure 3.1: Galactic space position and velocity coordinates for J080822.18-644357.3 (purple dot), relative to the members of the Carina association used in BANYAN II (green dots). Red lines are 1σ error bars, oriented to decouple errors in proper motion and radial velocity. The orange ellipsoid highlights the 68% confidence interval in 3D space, while the gold contours indicate the two-dimensional projections of the ellipsoid in each plane. The Galactic position and velocity coordinates for J080822.18-544357.3 indicate that it has 93.9% probability of membership in this association.

The excess observed around this star is much larger than the warm debris excess observed around any other mid-M dwarf. The infrared colors of the star are quite similar to the colors of T Tauri stars observed in the youngest embedded clusters (e.g. Luhman & Mamajek, 2012). Additionally, our derived value of $L_{ir}/L_{\star}$ for this star is comparable to those observed for protoplanetary disks in Taurus, IC 348, and other new star-forming regions. However, large surveys of disks in young associations suggest that gas-rich protoplanetary disks dissipate by ~ 10 Myr (e.g. Williams & Cieza, 2011). With such a large excess at an age of ~ 45 Myr, this disk system is an outlier, which compels further study.

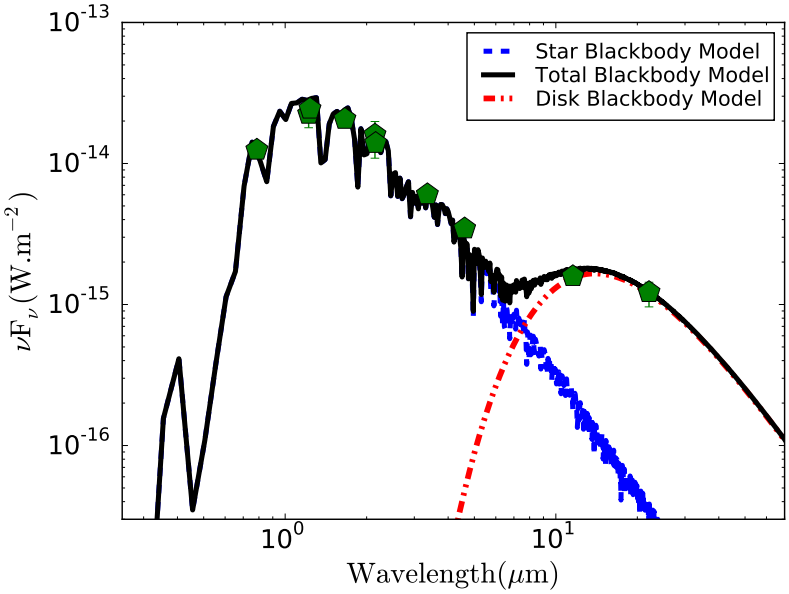

Figure 3.2: Spectral energy distribution for J080822.18-644357.3, with stellar atmosphere (blue dashed line) + blackbody (red dot-dash line) fitting applied to observed photometry (green pentagons) from 2MASS, AllWISE, and the DENIS survey, to produce a total model (black solid line). Our fitting indicates a disk temperature ~ 263 K, and $L_{ir}/L_\star = 8.06 \times 10^{-2} \pm 9.02 \times 10^{-3}$.

3.4 Summary and Discussion

In this paper, we identified one new star with infrared excesses that has a high ($> 90\%$) likelihood of membership in the Carina association. This new YMG disk candidate is a valuable target for further follow-up observations with adaptive-optics systems on large telescopes. As it is a candidate member of a nearby (distances < 100 pc) association (Malo et al., 2013, and references therein), it is well within range for high-contrast imaging to resolve the disk structure (Currie et al., 2015; Boccaletti et al., 2015; Schneider et al., 2014), which will contribute to our understanding of disk evolution at the age of the Carina association. Its known young age also makes it a prime target for finding exoplanets via direct imaging, given the expected warmth of any exoplanets orbiting the disk (Marois et al., 2008, 2010).

If confirmed as a member of Carina, our new debris disk appears to be the oldest observed YMG M dwarf debris disk. The frequency of M dwarf debris disks at varying ages is a subject of intense debate in the literature. The frequency of debris disks around young ($\leq$ 40 Myr) M dwarfs is $\sim$ 6% (Binks, 2016), while the prevalence around older M dwarfs is $\leq$ 1.3% (Avenhaus et al., 2012; Theissen & West, 2014). In contrast, debris disks are detected around $32 \pm 5\%$ of young A stars with *Spitzer*/MIPS (Su et al., 2006), and around $1 - 6\%$ of old ($\sim$ 670 Myr) Sun-like (F5-K9) stars with *Spitzer*/MIPS (Urban et al., 2012). Survival models predict that M dwarf debris disks occur at a similar frequency as disks around Sun-like stars, and that the dearth of detections to date is either due to systems having blackbody-like dust close to their central star, or due to systems having a smaller amount of dust distributed over a larger orbital separation (Heng & Malik, 2013). Alternatively, disk dissipation could be accelerated around these stars due to stellar wind drag (Plavchan et al., 2005, 2009). Our new M dwarf debris disk would bridge the gap between YMG and field M dwarf disks. Given their common spectral type (both M5.5V), this system could be a young analog for the Proxima Centauri system (Anglada-Escudé et al., 2016), as well.

We identified this new candidate YMG member with infrared excess via the ongoing Disk Detective project, out of an initial sample of 1774 DDOIs. We expect to find $\sim$ 12000 DDOIs by the end of the Disk Detective project, so we expect to find more YMG candidate disks as the project continues. We detected fewer YMG candidate members from this sample than might have been expected, given the results of Kennedy & Wyatt (2013). We believe that this low detection rate is in part due to Disk Detective's sizable inclusion of objects with distances $>$ 100 pc, more distant than any of the moving groups included in BANYAN II. Additionally, some nearby high-proper-motion targets may have originally been classified as "shifting" targets rather than good candidates. We have begun re-evaluation of

these shifting targets to identify these false negatives. Forthcoming improvements to the BANYAN software and results from the *Gaia* mission (Perryman et al., 2001) should lead to substantially higher yields in the future, as well. We plan to add an additional six known YMGs, which are not currently included in any probabilistic membership tool, to the BANYAN software. The data from *Gaia* are likely to yield many previously-undiscovered YMGs, as well as find previously-unidentified members of the currently known moving groups and associations. We expect that *Gaia* will determine parallaxes, proper motions, and radial velocities for $\sim 70\%$ of our current list of DDOIs.[4] Extrapolating to the anticipated 12,000 DDOIs and assuming the use of *Gaia* data, we estimate that we will identify an additional ~ 15 candidate members of the moving groups and associations studied here with significant 22μm excess by the end of the Disk Detective project.

[4]Since initial publication, *Gaia* DR2 has provided 5D (without radial velocity) kinematics measurements for 74.5% of the Disk Detective input catalog; however, only 7% of those have statistically significant parallax measurements. Future data releases from *Gaia* should increase this fraction, as measurement precision improves.

Chapter 4

Peter Pan Disks: Long-lived Gas-Rich Disks Around Pre-Main Sequence M Stars

4.1 Introduction

Primordial disks around solar-mass stars have been shown to dissipate rapidly over time in *Spitzer* disk surveys. The c2d project, observing 188 classical and weak T Tauri stars (CTTS; WTTS) spanning spectral types G5-M5 in the Taurus, Lupus, Ophiochus, and Chamaeleon star-forming regions (Padgett et al., 2006) found that no studied weak-lined T Tauri stars (WTTS) exhibited a disk beyond an age of 10 Myr (Wahhaj et al., 2010). The FEPS project, surveying $\sim$ 328 approximately solar-mass ($0.7 - 2.2 M_{\odot}$) stars from ages 3 Myr to 3 Gyr, found that only $\sim$ 12% of stars surveyed younger than 10 Myr exhibited a primordial disk, and only $\sim$ 2% of stars surveyed between 10 and 30 Myr exhibited such a disk (Carpenter et al., 2009).

Studies of large young clusters and associations have also shown that disks around high-mass star disks dissipate more quickly than those around solar-mass stars (Carpenter et al., 2006). Pecaut & Mamajek (2016) took a census of disks around K stars in the Scorpius-Centaurus complex. From this, they determined disk fractions for each component of Sco-Cen, finding full disk fractions of $9.0^{+4.0}_{-2.2}$% for the 10 ± 3 Myr Upper Scorpius association, $5.1^{+2.4}_{-1.2}$% for the 16 ± 2 Myr Upper Centaurus-Lupus association, and $3.4^{+2.5}_{-1.0}$% for the 15 ± 3 Myr Lower Centaurus-Crux association. Using these data points, they found that the characteristic (e-folding) timescale for primordial disk lifetimes around K-type stars was 4.7 Myr—that is, only $1/e$ disks around K-type stars in this association have not

dissipated in a 4.7-Myr span. Given that K-type stars have higher primordial disk fractions than solar-type stars in the same associations, one would expect that M dwarf primordial disks would have an even longer lifetime. Indeed, the most recent detailed study of the Upper Scorpius association (age 10 ± 3 Myr, Pecaut & Mamajek, 2016) found that the frequency of M dwarf primordial disks was more than three times the frequency of primordial disks around all earlier-type stars in the same association (Esplin et al., 2018), suggesting a disk lifetime timescale much longer than the 4.7 Myr for K stars in the same association.

In contrast to the prevalence of M star and brown dwarf primordial disks in young associations, M dwarf debris disks are detected much less frequently than their counterparts around higher-stars. The occurrence rate around field M dwarfs is $< 1.4\%$, based on observational surveys (Plavchan et al., 2005, 2009; Avenhaus et al., 2012). These systems are more commonly detected in younger systems; Forbrich et al. (2008) find significant 24μm around 4.3% of M dwarfs in the 30-40 Myr cluster NGC 2547, while Binks & Jeffries (2017) find significant 22 μm excess around 13%($\pm$5%) of $<$ 30-Myr M dwarfs. These detection rates are still significantly lower than their earlier-type counterparts (Greaves, 2010). While some argue that this could be due to the detector limits of WISE (e.g. Heng & Malik, 2013), the low detection rate of debris disks around older M dwarfs could indicate rapid clearing by stellar wind (e.g. Wyatt, 2008) or stellar activity (e.g. AU Mic; Grady et al. 2019, in prep).

The Disk Detective project (Kuchner et al., 2016, hereafter Paper 1) identifies circumstellar disk candidates in the AllWISE catalog using visual inspection of objects with WISE-detected infrared excess by citizen scientists. Silverberg et al. (2016, hereafter Paper 2) identified WISEA J080822.18-644357.3 (J0808), a disk candidate discovered by Disk Detective citizen scientists, as a likely member of the 45-Myr Carina association (Bell et al., 2015) based on its kinematics. J0808

exhibits a large fractional infrared luminosity ($L_{\rm ir}/L_\star > 0.01$), surprising given its age, as such a high $L_{\rm ir}/L_\star$ is typically only seen in primordial disks. Paper 2 initially characterized this as one of the oldest dM-type debris disk systems. Murphy et al. (2018) confirmed membership of J0808 in Carina based on its radial velocity and detected lithium absorption in optical spectroscopy, and noted broad, variable Hα emission indicative of active accretion, suggesting that the system is instead a gas-rich primordial disk. They also identified correlated variability in the W1 and W2 single-epoch photometry of the object consistent with a variable hot disk component, and listed three other systems from the literature that exhibited emission indicative of accretion (2MASS J0041353-562112, J02265658-5327032, and 2MASS J05010082-4337102, hereafter J0041, J0226, and J0501; Reiners, 2009; Boucher et al., 2016) in the Great Austral Young Association (GAYA), a large, $\sim$ 45-Myr complex consisting of the Tucana-Horologium (THA), Columba (COL), and Carina (CAR) associations. Flaherty et al. (2019) recently published ALMA observations of J0808, in which they detected continuum dust emission consistent with a third disk component (in addition to those identified in the WISE data), but did not detect cold CO gas.

In this paper, we discuss the characteristics of the known examples of a class of disk we name "Peter Pan" disks: disks around low-mass stars and brown dwarfs at ages $>$ 35 Myr based on membership in a $\sim$ 45 Myr moving group that exhibit substantial mid-IR excesses and evidence of accretion indicative of a gas-rich disk—that is, accretion disks that seem to "never grow up" (Barrie, 1904). In Section 4.2, we present identifications of new examples of this phenomenon, based on astrometry and kinematic information from the second data release of *Gaia* and optical spectroscopy. In Section 4.5, we summarize our observations of known Peter Pan disks, including both ground- and space-based high-cadence photometry

and near-infrared spectroscopy. In Section 4.6, we present high-cadence optical photometry of J0808, which exhibits variability indicative of accretion as well as a high-amplitude classical flare, and J0501, which indicates strong periodicity and a classical flare. In Section 4.7, we present near-IR spectroscopy of J0808, which identifies the short-wavelength end of the W1/2 excess identified by Murphy et al. (2018) and shows variable accretion. In Section 4.8, we formally define Peter Pan disks, determine which of the systems that have been identified as potential older accretion disks meet these criteria, and discuss potential mechanisms for disks that produce these signatures. We summarize our findings in Section 4.9.

4.2 Identification of New Peter Pan Disk Systems

As part of our ongoing work to build a publicly-accessible database for Disk Detective through the Mikulski Archive for Space Telescopes at the Space Telescope Science Institute[1], we cross-matched the *Gaia* DR2 catalog with the Disk Detective input catalog. Rather than exclusively using the matches provided in DR2, we projected objects in DR2 back to their expected WISE positions using the proper motion data in DR2, then found the nearest WISE source to that position. Our cross-match did not explicitly take into account the position of nearby objects in the *Gaia* data. We ran the results of this crossmatch through BANYAN Σ (Gagné et al., 2018) to identify potential new moving group members, specifically with an eye toward identifying new Peter Pan disks. This produced two late-type systems with a high probability of membership in a $\sim$ 45-Myr moving group. WISEA J044634.16-262756.1 has a 96.9% likelihood of membership in the $\sim$ 42-Myr Columba association (COL) based on its parallax and proper motion from *Gaia*. WISEA J094900.65-713803.1 has a 99.2% likelihood of membership

[1]Accessible through the portal at `https://mast.stsci.edu`.

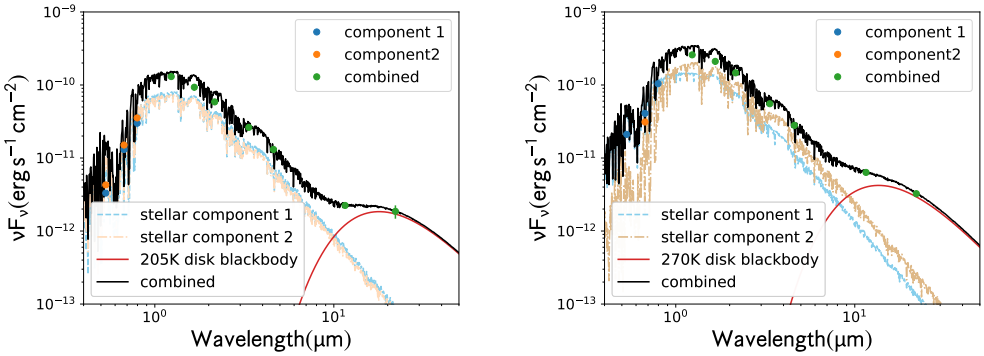

Figure 4.1: *Left*: SED fit for the J0446 system. *Right*: SED fit for the J0949 system. Characteristics of the systems are listed in Table 4.1.

in the Carina association.

Each of these systems is an apparent visual double, with a nearby star at an angular distance within the beam size of both 2MASS and WISE, based on data from Pan-STARRS DR1 and *Gaia* DR2. Initial SED fitting using *Gaia* photometry to estimate the spectral type of each component indicated that both J0446 and J0949 exhibited significant excess at W3 and W4 after accounting for both stellar components. Additionally, BANYAN Σ indicated that the two nearby targets were also possible moving group members. SED fits of the systems are shown in in Figure 4.1.

4.3 Follow-up Spectroscopy of New Peter Pan Disk Systems

We obtained spectra of each of these targets during 2018 November in queue mode with the Gemini Multi-Object Spectrograph (GMOS-S) at the Gemini-South observatory through Program GS-2018B-FT-106, to confirm moving group membership and further characterize the systems. We observed both objects in each apparent visual double. We observed three spectra of each target in sequence to mitigate cosmic rays, using the 0.5″ longslit with the R831 grating centered at

7570 Å to achieve spectral resolution of 4396, with wavelength coverage of 6394-8736 Å. We used the GG455 filter to block second-order light. Quartz/halogen flats were taken after each set of science observations, and master arcs for the project were taken using Cu-Ar lamps on 2018 November 8. We used the flux standard LTT 1020, observed on 2018 October 3, to calibrate our result spectra. Exposure times ranged from 12-100 seconds, based on expected brightness, yielding spectra with SNR 14-25 at Hα. Spectra were reduced using version 2.16 of the Gemini package in PyRAF, using standard techniques. We list the four components at J0446A, J0446B, J0949A, and J0949B in Table 4.1, along with separate equatorial positions for each target, and their astrometric information. Data from these spectra are listed in Table 4.1, along with their *Gaia* astrometry and *WISE* excess information, and the spectra are plotted in Figure 4.2.

4.4 Analysis of New Peter Pan Disk Systems

4.4.1 Spectral types

We used the PyHammer package (Kesseli et al., 2017) to classify our four spectra. Given the proximity of the four targets to the Sun, we assumed solar metallicity for all four cases. We adopt spectral types of M6 for both components of J0446, and find that J0949 consists of an M5 and an M4. The four spectra, with comparison spectral standards, are shown in Figure 4.2.

4.4.2 Age estimates and radial velocity measurements

To confirm the membership of these specific objects in moving groups, we must find the stellar radial velocity (to ensure that its full kinematics match those of the group), and identify an independent age constraint.

Table 4.1. New Peter Pan Disk Candidates From *Gaia* DR2 and BANYAN Σ

Designation	J0446A	J0446B	J0949A	J0949B	References
R.A. (h:m:s)	04:46:34.105362	04:46:34.249381	09:49:00.752604	09:49:00.441275	1
DEC (d:m:s)	-26:27:56.83936	-26:27:55.57007	-71:38:02.94748	-71:38:03.15884	1
Separation (pc)	0.347 ± 0.341		1.100 ± 0.474		2
Spectral Type	M6	M6	M5	M4	2
Group	COL	COL	CAR	CAR	3
EW[Hα] (Å)	-10.44 ± 0.22	-16.79 ± 0.18	-23.91 ± 0.25	-110.04 ± 0.29	2
v_{10}[Hα] (km s^{-1})	210 ± 14	239 ± 13	305 ± 20	367 ± 16	2
EW[Li I 6707.8] (mÅ)	< 108	< 126	< 251	< 116	2
Parallax (mas)	12.1093 ± 0.0629	12.1604 ± 0.0594	12.6285 ± 0.0742	12.8064 ± 0.0509	1
$\mu_\alpha \cos\delta$ (mas/yr)	33.351 ± 0.084	33.534 ± 0.080	-36.096 ± 0.135	-39.135 ± 0.099	1
μ_δ (mas/yr)	-5.459 ± 0.118	-3.629 ± 0.112	28.565 ± 0.131	23.582 ± 0.117	1
Radial velocity (kms^{-1})	26.7 ± 16.8	29.8 ± 16.8	20.5 ± 16.8	22.4 ± 16.7	2
Excess ([W1]-[W3])	1.146 ± 0.034		1.468 ± 0.027		2
Excess ([W1]-[W4])	3.093 ± 0.078		2.888 ± 0.043		2
Stellar temperature	~ 2800	~ 2800	~ 3050	~ 3200	4
Warm disk temperature (K)	299^{+11}_{-9}		279^{+7}_{-6}		2

References. — (1) Gaia Collaboration et al. (2018). (2) This work. (3) Gagné et al. (2018). (4) Pecaut & Mamajek (2013).

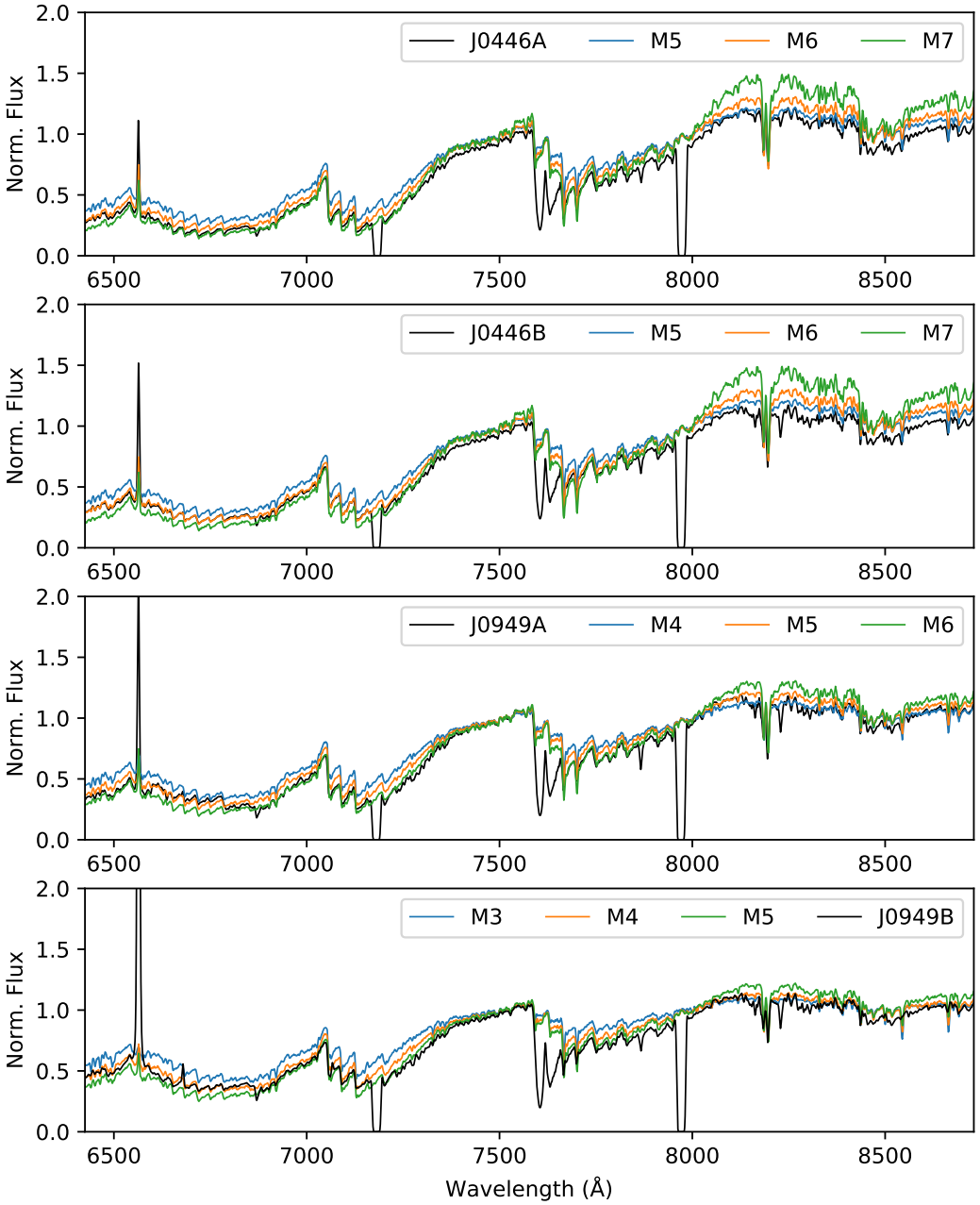

Figure 4.2: Spectra of the four new potential Peter Pan disks, plotted against PyHammer empirical spectral templates. Observed and template spectra are normalized at 7500Å. The dips in the observed spectra are due to the GMOS chip gaps. Note the strong Hα emission in all four spectra, and the He I λ6678 emission in J0949B.

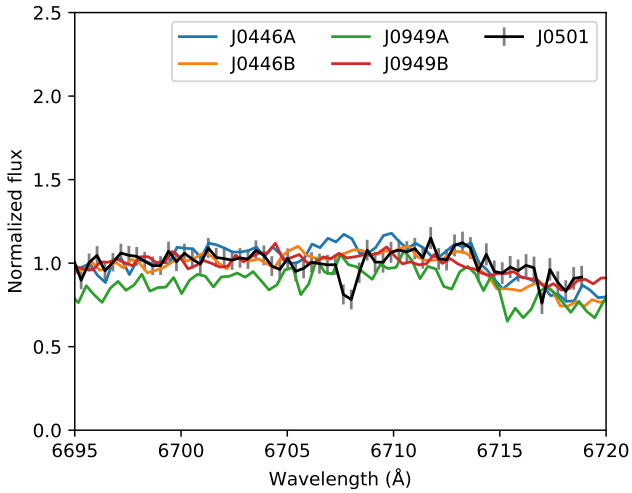

Figure 4.3: GMOS spectra of the region around the Li I absorption line at 6707.8 Åin four new Peter Pan disk candidates, compared with observations of J0501 (Boucher et al., 2016) smoothed to the resolution of the GMOS data. None of the four disk candidates show significant absorption, though such absorption should be detectable based on the rebinned spectrum of J0501.

We determined radial velocities for each of the four targets based on Gaussian fitting of four prominent lines (Hα, K I λ7669, Na I λ8183, and Ti I λ8435). Uncertainties for each measurement reflect the 68% confidence interval of the line profile as determined using `emcee` (Foreman-Mackey et al., 2013), the resolution of the spectrograph, and instrumental uncertainty due to telescope flexure. These measurements are listed in Table 4.1.

Figure 4.3 depicts the spectra for our four targets around the lithium feature at 6707.8 Å, along with the spectrum of J0501 (adopted from Boucher et al., 2016), degraded to the resolution and rebinned to the dispersion of our data. As seen in Figure 4.3, we do not detect clear evidence of lithium in our data, deriving upper limits of 0.11-0.25 Å. Lithium is often used as an age indicator (Murphy et al., 2018, and references therein); these upper limits are consistent with ages 40-45 Myr and our moving group assignments.

Another indicator of youth is the depth of the Na I doublet at 8200 Å which

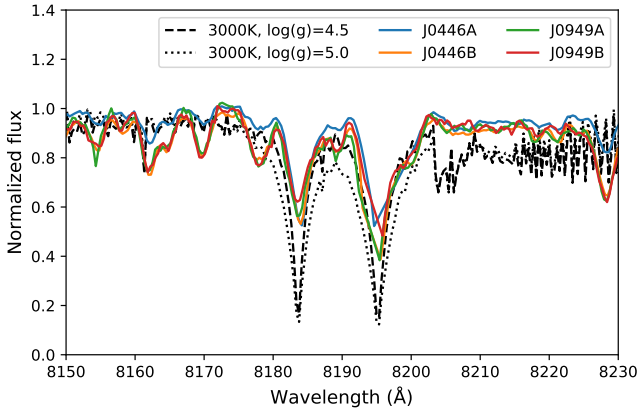

Figure 4.4: GMOS spectra of the Na I 8200 Å feature in four new Peter Pan disk candidates, compared with BT-Settl CIFIST models (Baraffe et al., 2015) smoothed to the resolution of the GMOS data and shifted to the wavelength scale of the GMOS data. All four disk candidates exhibit Na I 8183 Å absorption weaker than the $\log(g) = 5.0$ model but not dissimilar to the 4.5 model, indicating weaker gravity than a typical dwarf and therefore youth.

can be used to differentiate young cluster and moving group members from field stars and giants (Schlieder et al., 2012). The 8195 Å line of this feature falls on a bad pixel column in our data, making an equivalent width measure of the feature in our data unreliable. However, we can compare the observed line profiles of the 8183 Å line to stellar models to qualitatively assess the depth of the line. As seen in Figure 4.4, all four of our spectra are much shallower at 8183 Å than a BT-Settl (Baraffe et al., 2015) model of a mid-M dwarf, suggesting that they have weaker gravity and are therefore younger than the typical field M dwarf.

4.4.3 Hα emission and accretion

Accretion of disk material from a circumstellar disk onto the host star is accompanied by enhanced line emission (e.g. Muzerolle et al., 1998). We identify Hα emission on all four of our candidates, as shown in Figure 4.5. We computed the equivalent width of each line via direct integration of the observed spectrum after

continuum fitting. We list these widths, ranging from -110Å $<$ EW[Hα] < -10Å, in Table 4.1.

Fang et al. (2009) proposed an equivalent width limit of -18 Å for Hα for a mid-M accretor. While J0446A and J0446B do not meet the Fang et al. (2009) limit, both J0949A and J0949B do. All four objects show an equivalent width larger in magnitude than the -7.56 angstroms exhibited by 2MASS J0501 (Boucher et al., 2016), but only J0949B approaches the -125 Å $<$ EW[Hα]$<$ -65Å values observed for J0808.

Following Murphy et al. (2018), we estimated the velocity width at one-tenth maximum (v_{10}) by normalizing the line profile to a linear fit to the continuum at $\pm 1000 - 500 \mathrm{kms}^{-1}$, and finding the numerical intercept of the line profile and the $f = v_{10}$ line (as shown in Figure 4.5). White & Basri (2003) adopt a $v_{10} > 270 \mathrm{kms}^{-1}$ criterion for accretion across all M-types, while Jayawardhana et al. (2003) adopt a $v_{10} > 200 \mathrm{kms}^{-1}$ for M5-M8 stars, and Natta et al. (2004) adopts a $v_{10} > 200 \mathrm{kms}^{-1}$ criterion for M6-M8.5 stars. We adopt the Jayawardhana et al. (2003) criterion for the three stars with spectral types M5-M6, and adopt the White & Basri (2003) criterion for J0949B, which has a spectral type out of this range. Using these criteria, all four objects are accreting. v_{10} widths for the four targets are listed in Table 4.1.

Asymmetry of the line profile can also indicate whether emission is due to accretion rather than stellar activity, as infalling material should have some velocity shift relative to the host star (e.g. Hartmann et al., 2016). We present the Hα profiles of the four targets in Figure 4.6, plotted against the best-fit Gaussian for each object to provide a symmetric reference to guide the eye. The line cores appear symmetric, once the asymmetric distribution of pixels across the line is accounted for. J0949A shows no obvious asymmetry. J0446A shows enhancement

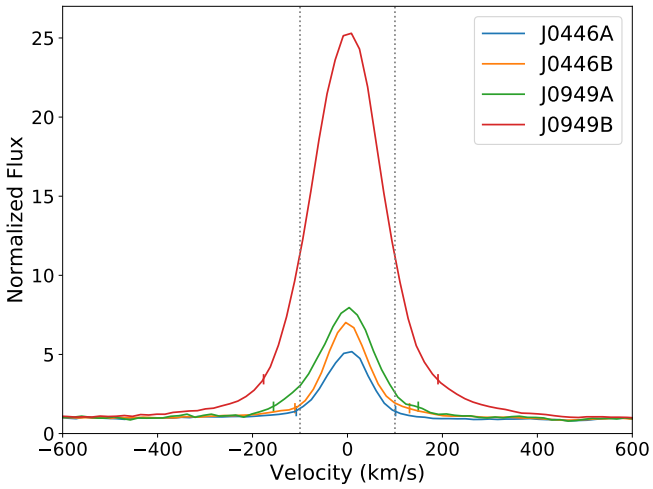

Figure 4.5: GMOS velocity Hα profiles of the four new Peter Pan disk candidates. Vertical markers indicate the velocity at which the profile is at 10% of maximum. The dotted lines are the symmetric $v_{10} = 200\text{kms}^{-1}$ criteria defined by Jayawardhana et al. (2003) and Natta et al. (2004).

in the blue wing of the line compared to the red wing, though this may be due to the severe negative slope of the continuum in this range and imperfect continuum subtraction. Counter to this, J0949B exhibits an enhanced red wing of the profile compared to the blue wing. J0446B shows an asymmetric profile in the wings, similar to the asymmetric profile observed in 2MASS J05010082-4337102 (Boucher et al. 2016). None of the asymmetry observed here is to the degree of asymmetry exhibited by Hα in young CTTSs (e.g. Hartmann et al., 2016); while there is apparent qualitative asymmetry, it is not quantitatively significant.

We determined accretion rates using the Natta et al. (2004) $v_{10,H\alpha} - \dot{M}_{acc}$ relation (following Murphy et al., 2018; Boucher et al., 2016). Accretion rates (listed in Table 4.1) range from $-10.8 < \text{Log}(\dot{M}_{acc}) < -9.3$. These rates are likely higher than the true accretion rate, as the Natta et al. (2004) relation was calibrated on younger (and therefore higher-radius) stars (as noted by Murphy et al., 2018).

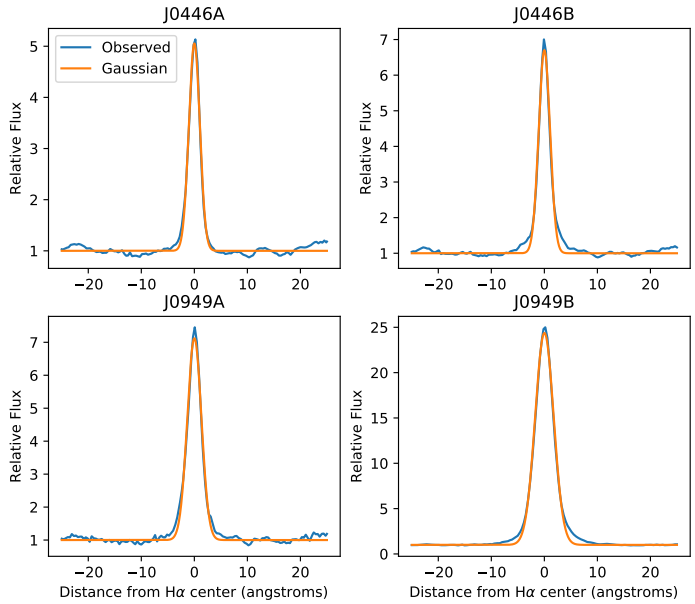

Figure 4.6: Observed Hα line profiles of the four targets, compared with best-fit Gaussians. Each example exhibits some qualitative asymmetry.

4.5 Observations of Known Peter Pan Disks

4.5.1 High-Cadence Optical Imaging

We obtained high-cadence optical photometry of J0808 over nine nights with the CTIO/SMARTS 0.9m telescope at Cerro Tololo Inter-American Observatory, from UT 2018 February 14-22, primarily to detect optical/UV flares (Lacy et al., 1976; Kowalski et al., 2013). Exposure times ranged 90-105 seconds exposures depending on sky transparency, to maximize signal-to-noise while maintaining as high a cadence as possible. We observed in the SDSS g band to maximize contrast of the UV-bright flares with the underlying stellar photosphere while ensuring the faint source was detected in quiescence. To minimize time on-sky lost to readout, we observed in four-quadrant read-out, only exposing the inner 1024×1024 pixels. Data were reduced using standard IRAF procedures, and cosmic rays were removed using the `lacosmic` function (van Dokkum, 2001). Relative differential

photometric lightcurves were generated for each night using AstroImageJ (Collins et al., 2017). We used an ensemble of six stars in the field of view as comparison stars for the target. To ensure that these stars were non-variable, we analyzed light curves produced by differential photometry of each comparison star compared to the others in the ensemble; all observations in the light curves of these comparison stars are within 5σ of the light curve median. Typical photometric uncertainties of the target are on the order of 2%.

Additionally, both J0808 and J0501, another Peter Pan disk candidate in the Columba system (Boucher et al., 2016), were observed at two-minute cadence by the Transiting Exoplanet Survey Satellite (TESS; Ricker et al., 2014) during Cycle 1, Sector 4, as part of TESS GI Program G011148 (PI Kuchner). J0808 appeared in CCD 4 of Camera 4, while J0501 appeared in CCD 4 of Camera 3. The two-minute cadence data consist of 11×11 pixel subarrays, reduced with the Science Processing Operations Center (SPOC) pipeline, as described in Jenkins et al. (2016). We use the two-minute Presearch Data Conditioning light curves from the SPOC pipeline, extracted from the apertures depicted in Figure 4.7. The aperture for J0808 includes contributions from four other nearby stars that are spatially resolved in the CTIO data. We address the effect of these stars in Section 4.6.

4.5.2 Near-Infrared Spectroscopy

We observed J0808 three times with the Astronomy Research using the Cornell Infra Red Imaging Spectrograph (ARCoIRIS) near-infrared spectrograph (Schlawin et al., 2014) on the 4m Victor Blanco Telescope at Cerro Tololo Inter-American Observatory. Observation dates, individual exposure times, and total integration times are listed in Table 4.5.2. We observed multiple spectra of the target and a

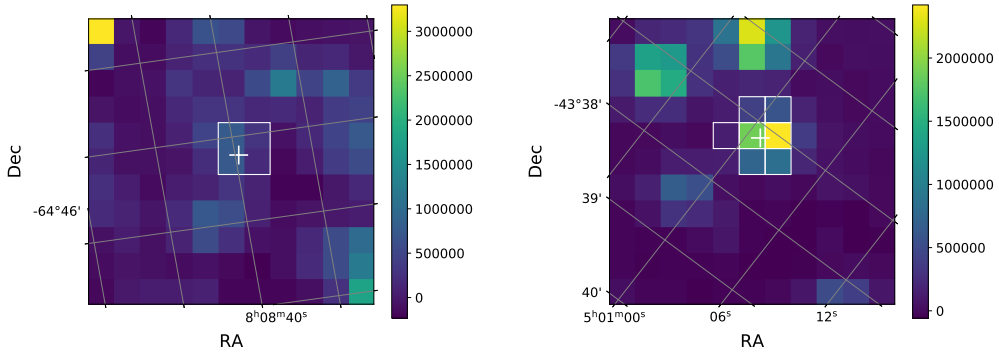

Figure 4.7: The TESS target pixel files for J0808 (*left*) and J0501 (*right*) in Cycle 1, Sector 4. The PDC apertures are enclosed by white boxes.. The *Gaia* DR2 positions of the target stars are indicated by white crosses.

Table 4.2. Observing Data for Near-IR Spectroscopy with Blanco/ARCoIRIS

Date	Number Exposures	Total Integration Time (s)
2017-11-04	12	540
2018-03-01	12	540
2018-03-02	12	720

nearby A0V star (for use in telluric correction) using an ABBA pattern to correct for sky variability over the observation. We reduced the data using the ARCoIRIS extension of the `Spextool` package (Cushing et al., 2004), combined spectra using the `xcombspec` package (Cushing et al., 2004), and corrected for telluric lines using the `xtellcor` package (Vacca et al., 2003).

4.6 Variability in High-Cadence Optical Photometry

4.6.1 Varying Morphologies in Different Bandpasses of J0808

Figure 4.8 depicts the light curve of J0808 from CTIO, while Figure 4.9 depicts the lightcurve from TESS. Cody et al. (2014) presents a morphology classification

system for young stellar objects in space-based high-cadence light curves. As J0808 shows evidence of accretion in both optical (Murphy et al., 2018) and near-IR (Section 4.7) spectroscopy, we adapt this system to our data.

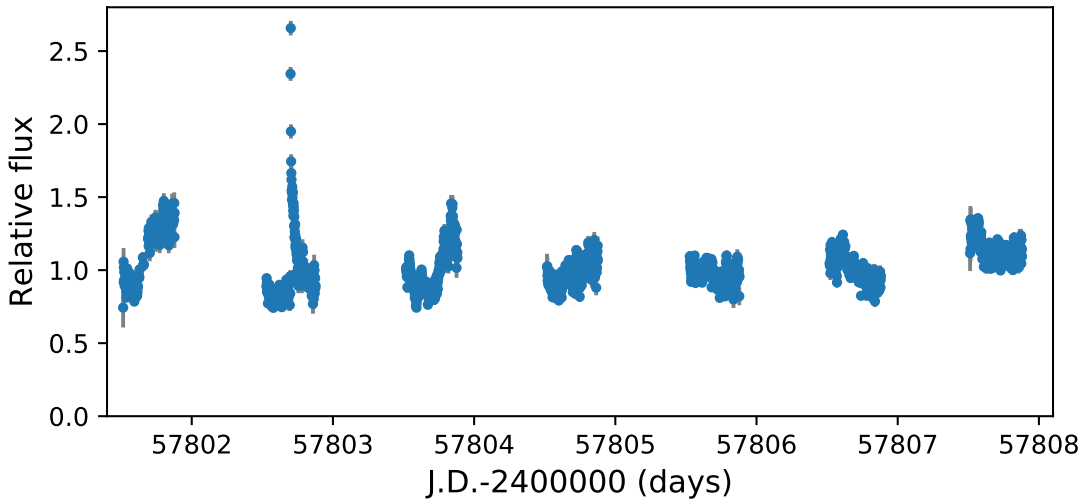

Figure 4.8: The CTIO light curve of J0808 is characterized by short-duration aperiodic bursts, on timescales of half a night, and a large flare. Relative flux is calculated by dividing the sky-subtracted target star flux from the sky-subtracted flux of the comparison ensemble, and is normalized by dividing by the median.

Qualitatively, the CTIO light curve of J0808 exhibits stochastically-occurring, low-amplitude bursting events (Stauffer et al., 2014), thought to correspond to accretion events. To quantify this, we applied a variation of the Cody et al. (2014) M statistic, which measures how asymmetric the light curve is with respect to reflection in the flux dimension (i.e. whether the light curve tends to burst, dip, or a mix of the two). Briefly, we smoothed the light curve for each night using a boxcar smoothing kernel of width 1.5 hours, and then identified 5σ outliers from the residual of the raw and smoothed light curves. We averaged the top and bottom 5% of values from the outlier-removed light curve, subtracted this value from the median of the outlier-subtracted light curve, and divided by the root mean square uncertainty of the outlier-subtracted light curve. Cody et al.

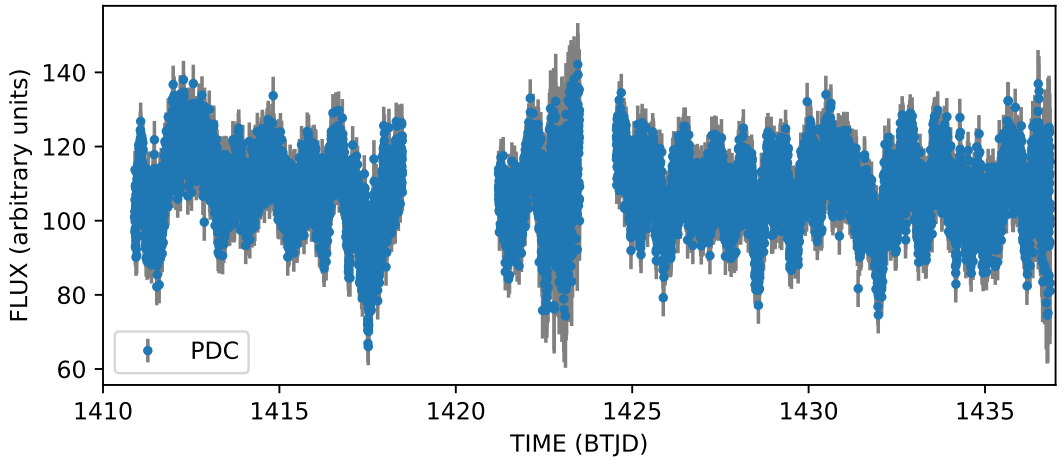

Figure 4.9: The TESS PDCSAP light curve of J0808 is primarily characterized by aperiodic dipping, on timescales of half a day to two days. Gaps appear due to an instrument anomaly (TJD 1418.53-1421.21) and a data download (1423.51-1424.55). The light curve is normalized by division by the light curve median.

(2014) define "bursters" as targets with $M < -0.25$, and "dippers" as targets with $M > 0.25$; objects with values between these limits are classified as "symmetric." For the CTIO data, $M = -0.602$, consistent with our qualitative "bursting" assessment

Periodicity in the CTIO light curve is more difficult to assess, given the degeneracies that arise from the large gaps in the ground-based light curve. Due to these gaps, we discarded the autocorrelation-function-based assessment of Cody et al. (2014), instead adapting it to use the Lomb-Scargle periodogram (Lomb, 1976; Scargle, 1982). We show the Lomb-Scargle periodogram for J0808 and neighboring stars within the TESS aperture in Figure 4.10. We see strong periods of 1.10 days and 0.53 days for J0808, likely aliases of each other introduced by the windowing function of nightly observations. However, similar signals do not appear for the other stars in the aperture, and the periodogram of the combined-flux light curve of all four stars is dominated by the signal found in J0808.

The phase-folded light curve assuming a 1.098-day period has a gap due to

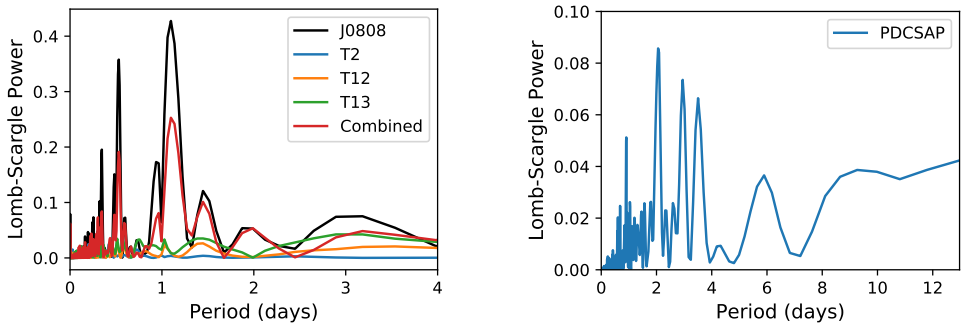

Figure 4.10: *Left*: Lomb-Scargle periodogram of CTIO lightcurves of J0808, three nearby stars within the TESS aperture, and the combined flux of the four stars. While J0808 shows two strong periods, likely aliased off each other by the nightly observing window, none of the other three stars exhibit similar periodicity, suggesting that the variability is intrinsic to J0808 rather than a purely observational effect. The periodogram of the combined flux is dominated by J0808, suggesting that any periodicity observed in the TESS data is attributable to J0808. *Right*: The Lomb-Scargle periodogram for the TESS light curve of J0808 does not exhibit a signal at the periods found in the CTIO data, suggesting that the strength of this signal is primarily due to the observing window.

the nightly observing window, so we adopt the 0.531-day period to derive the Q statistic from Cody et al. (2014), which measures how periodic a light curve is by determining the fraction of variability determined by the dominant periodic signal. With this period, we find $Q = 0.637$ for a 0.531-day period, an aperiodic variation per Cody et al. (2014). The most likely scenario is that the Lomb-Scargle periodogram is picking up this aperiodic variability.

The TESS light curve does not share these morphological characteristics. We qualitatively assess the light curve, shown in Figure 4.9, as an aperiodic dipper, but mostly symmetric, with dips on the timescale of half a day to several days. The Lomb-Scargle periodogram for the target (Figure 4.10) has no peaks with powers stronger than 0.1, further bolstering the case for aperiodicity. To quantify the level of (a)periodicity, we calculate the Q statistic using the strongest period from the light curve's Lomb-Scargle periodogram, which yields $Q = 0.85$. We find $M = 0.20$, which Cody et al. (2014) classify as symmetric, but closer to the dipper

end ($M > 0.25$) than the burster end.

We also recover one large classical flare during the CTIO observations, in the second night depicted in Figure 4.8, using the PyVan software (Lawson et al., 2019) for identifying and characterizing flares in unevenly-sampled photometry. The flare has a peak amplitude of 2.378× the median of the full light curve, and a duration of 0.08 days. Using the empirical flare template for GJ 1243 from *Kepler* (Davenport et al., 2014), we estimate a flare equivalent duration of ~ 955 s. Traditionally flare energies are calculated from the equivalent duration (e.g. Gershberg, 1972); however, this requires an accurate determination of the stellar luminosity. Given that the star is actively accreting, such a determination is not possible with the available data.

The TESS data do not reveal any obvious flares, possibly because the TESS bandpass is redward of the peak flare brightness, and the SNR of the TESS data (typically $\sim 20 - 25$) is low compared to the CTIO data. To quantify this, we derive a conversion to estimate the flux increase the flare observed with CTIO would produce in our TESS data, using known standard flare characteristics and the CTIO observations. We choose a 3100K, log(g)=4.5 BT-Settl (Baraffe et al., 2015) model to represent J0808 (Murphy et al., 2018), and a 10,000K blackbody to represent the flare (Kowalski et al., 2013). We then determine the filling factor a such that

$$aF_{g,\mathrm{flare}} + F_{g,\star} = 3.378F_{g,\star}, \tag{4.1}$$

where $F_{g,\star}$ and $F_{g,\mathrm{flare}}$ are the star and flare fluxes, determined by integrating the flare and star spectra over the Sloan g band, and $3.378F_{g,\star}$ is the observed flux at the flare peak relative to the median of the light curve.

We then inverted this equation in the TESS bandpass, using the value of a

from the g band to solve for the relative flux increase with TESS. We find that the CTIO flare would produce a 16.5% increase in flux observed with TESS at the flare's peak, a 3.33σ increase above the light curve median flux based on the light curve's RMS uncertainty.

We also estimated the peak brightness in Sloan g of a flare with peak brightness 5σ above the median TESS flux. Such a flare would have a peak brightness $\sim 4.6\times$ the observed median with CTIO.

4.6.2 Periodicity and a Flare on J0501

Figure 4.11 shows the TESS light curve for J0501. Unlike the light curve for J0808, J0501 exhibits both clear periodicity and an obvious flare. The Q and M statistics bear this out: $Q = 0.157$, on the periodic/quasi-periodic boundary, while $M = -0.005$, nearly perfectly symmetric. The period of J0501 is 0.906 days, and the phase-folded light curve (shown in Figure 4.12) exhibits a shape consistent with a persistent starspot or complex of starspots, as seen on the active M dwarf GJ 1243 with *Kepler* (Hawley et al., 2014; Davenport et al., 2015)

We estimate a stellar radius for J0501 of $0.32R_{\odot}$, following the J-magnitude-based relation of Pecaut & Mamajek (2013).[2] Using this, the observed TESS period, and the $v \sin i = 11 \mathrm{kms}^{-1}$ found by Boucher et al. (2016), we estimate an inclination angle for the system of $\sim 38^{\circ}$. While not face-on, this indicates an inclination angle favorable for potential spatial resolution of the disk.

In addition to the rotation period, we identify one flare in the TESS data using PyVan and visual inspection. Fitting the *Kepler* empirical flare template (Davenport et al., 2014) to it, we recover a rise time of 385 seconds, and a duration of 106 minutes, yielding an equivalent duration of 11.6 ± 1.6 minutes.

[2]We adapt the technique from Pecaut & Mamajek (2013) to use the 2015 IAU definition of $M_{\mathrm{bol},\odot} = 4.74$, as was done in Murphy et al. (2018).

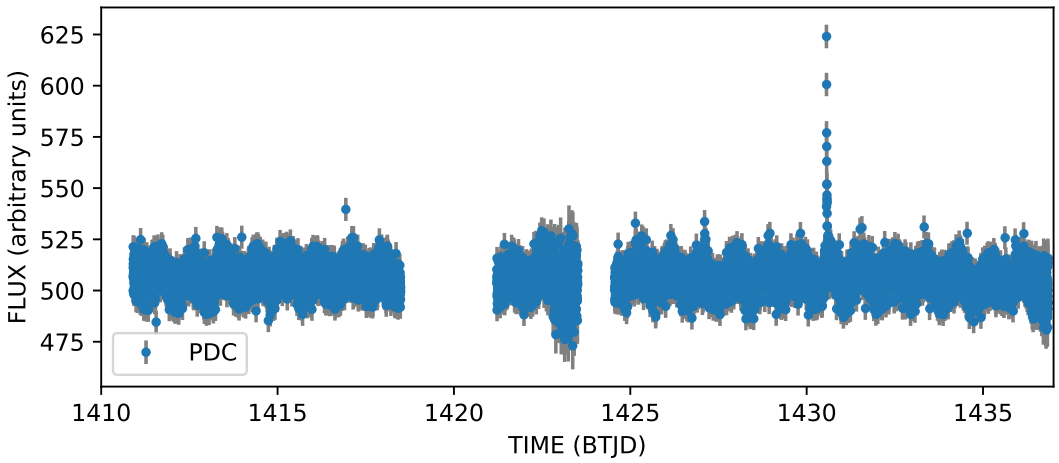

Figure 4.11: The TESS PDCSAP light curve of J0501 is dominated by a periodic oscillation characteristic of a persistent starspot or complex of starspots. We also note a flare peaking at 1430.561 days.

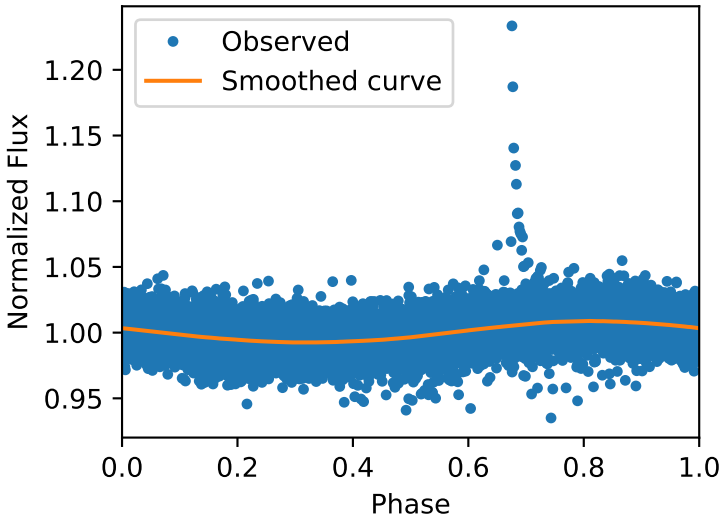

Figure 4.12: The phase-folded light curve for J0501 shows clear sinusoidal modulation with a period of 0.907 days.

4.7 Accretion and Excess Detection in Near-Infrared Spectroscopy

Figure 4.13 shows all three observations of J0808, compared with the SpeX library spectrum of Gl 866ABC (Rayner et al., 2009), a typical M5V star that we use as a comparison template based on the M5V spectral type from Murphy et al. (2018). This comparison spectrum overall shows a good match to the J0808 spectra, as expected given their common spectral types. However, there are significant deviations of interest in two places: J0808 exhibits an excess in its K-band spectra, and exhibits time-variable hydrogen emission.

4.7.1 K-band Excess

All three K-band spectra of the system (Figure 4.14) show a continuum level in excess of the expected continuum of an M5V star. Murphy et al. (2018) identified correlated variability in the W1 and W2 single-exposure photometry for J0808, with a best-fit blackbody of 1071 ± 103 K and fractional infrared luminosity $L_{\rm ir}/L_\star = 0 \ldots 0.11$ based on the observed variability. Our observations are consistent with detecting the short-wavelength end of this excess. The 1071 K blackbody at 0.11 $L_\star$ is a good fit to the excess beyond 2.30 μm in all three epochs; however, contributions from this blackbody do not appear at shorter wavelengths, suggesting a potential disk truncation radius. We do not detect any variability between observations above the continuum noise; however, the time series W1/W2 photometry has exhibited similar fluxes on 24-hour timescales.

4.7.2 Hydrogen Emission Variability

We determined equivalent widths and line luminosities for the Pa β and Br

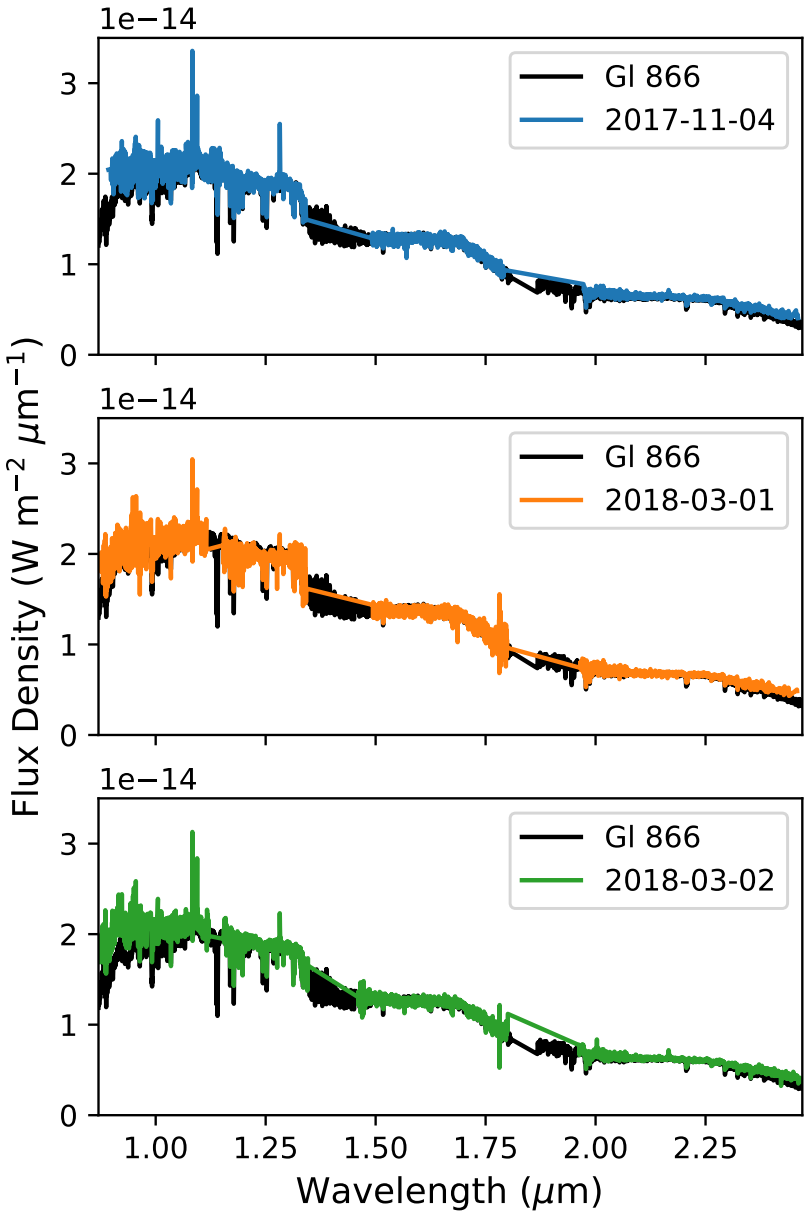

Figure 4.13: Near-infrared spectra of J0808 from Blanco/ARCoIRIS, compared with Gl 866, a library M5V star used as a template.

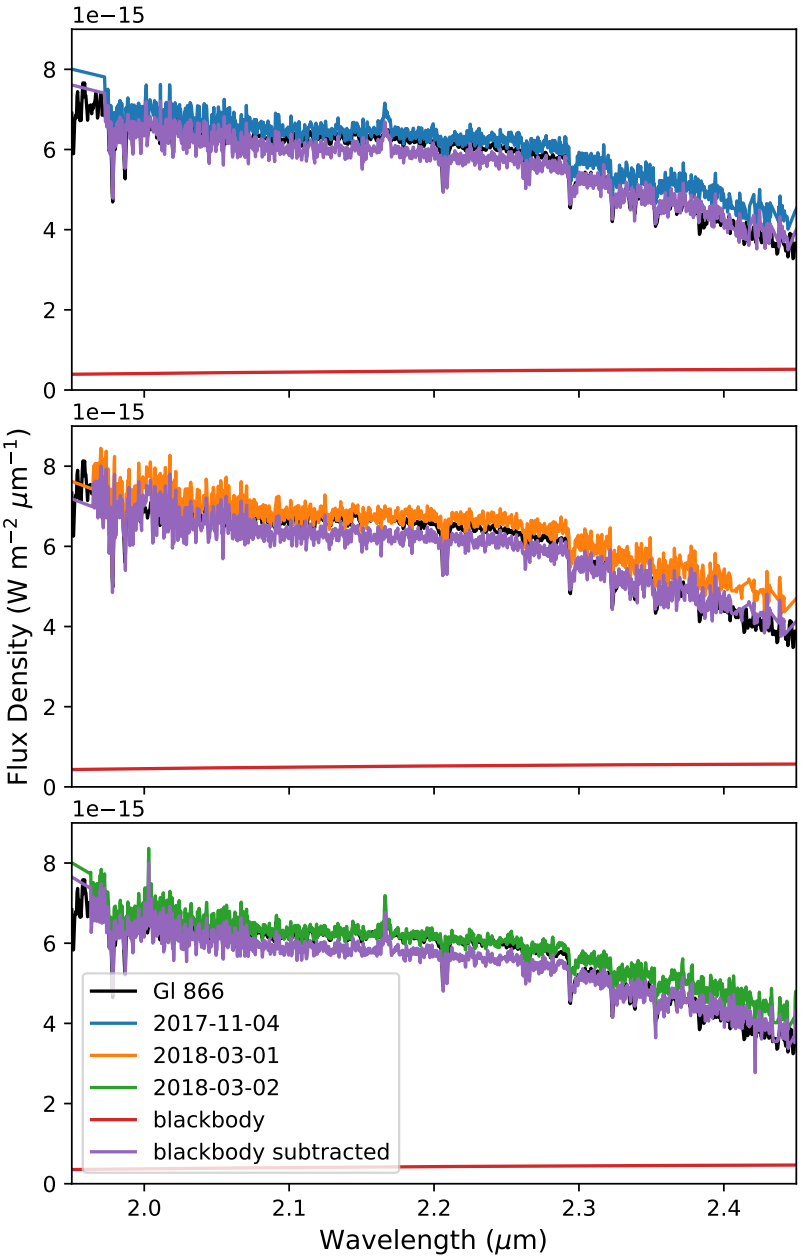

Figure 4.14: K-band spectra of J0808 from Blanco/ARCoIRIS, compared with Gl 866 (black). The red line in each panel represents the 1071K blackbody with $L_{\rm ir}/L_\star = 0.11$. The purple line is the observed spectrum, with the 1071K blackbody subtracted off. While the blackbody-subtracted spectrum matches Gl 866 well at wavelengths longer than 2.30 μm, the observed spectrum matches the template more closely at shorter wavelengths.

Table 4.3. Hydrogen Emission Characteristics in Near-IR Observations

Date	Pa β			Br γ			Accretion	Accretion
	EW Å	Line Flux $10^{-18}\mathrm{Wm}^{-2}$	Accr. Lum. $\log L_{\mathrm{acc}}/L_{\odot}$	EW Å	Line Flux $10^{-18}\mathrm{Wm}^{-2}$	Accr. Lum. $\log L_{\mathrm{acc}}/L_{\odot}$	Luminosity $\log L_{\mathrm{acc}}/L_{\odot}$	Rate $\log(\dot{M}_{\odot} yr^{-1})$
2017-11-04	3.96 ± 0.15	7.48 ± 0.30	-3.6 ± 1.1	4.61 ± 0.25	2.95 ± 0.17	-3.2 ± 1.4	-3.4 ± 1.1	-10.8 ± 1.3
2018-03-01	0.69 ± 0.23	1.36 ± 0.45	-4.7 ± 1.3	< 0.98	< 0.66	< -6.7	-4.7 ± 1.3	-12.0 ± 1.7
2018-03-02	1.08 ± 0.21	2.06 ± 0.41	-4.4 ± 1.3	4.02 ± 0.27	2.50 ± 0.18	-3.2 ± 1.4	-3.9 ± 1.2	-11.2 ± 1.2

γ emission lines in all three spectra. From these we estimated the accretion luminosity, using the log(Brγ) relation from Muzerolle et al. (1998). We use the log(Paβ) relation from Natta et al. (2004) rather than the similar relation from Muzerolle et al. (1998) because the former incorporates data from objects with lower masses and line luminosities than our target, allowing us to estimate the value for our star by interpolation rather than extrapolation. We used these accretion luminosities to estimate the mass accretion rate onto the star, using the stellar radius and mass from Murphy et al. (2018), and assuming that the inner radius of the accretion disk corresponds to the blackbody radius of the hot disk identified in Murphy et al. (2018). Results are listed in Table 4.7.2. Our mass accretion rates fall $\sim 0.8 - 2$ dex lower than those found by Murphy et al. (2018) using the $v_{10}[\mathrm{H}\alpha] - \dot{M}_{\mathrm{acc}}$ relation from Natta et al. (2004). This is expected, given that the $v_{10}[\mathrm{H}\alpha] - \dot{M}_{\mathrm{acc}}$ relation was calibrated for younger stars and was unadjusted for age.

While quantitatively the accretion luminosities do not significantly vary from observation to observations, the accretion signature lines show striking differences from image to image. Most notable is the complete disappearance of Br γ in the observation of 2018 March 01, as seen in Figure 4.15. While Br γ is a shallow line, and thus would be expected to disappear before Pa β does, this highlights the need for monitoring in multiple bandpasses at once. The lack of variation in accretion luminosity is due to the conversion from line fluxes to accretion fluxes, which is dominated by uncertainty in the conversion itself (rather than observational uncertainty in the line flux).

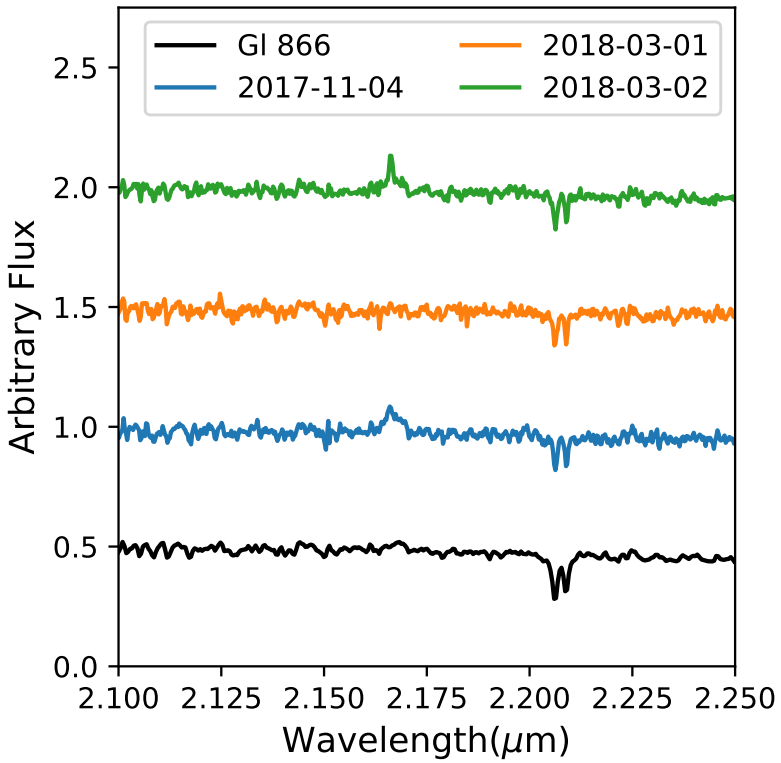

Figure 4.15: The Br γ region of AWI0005x3s. Spectra are normalized to the continuum around the line, and separated by an arbitrary offset for easier comparison. The 2017-11-04 spectrum shows broad emission above the expected underlying continuum (as depicted by Gl 866), while the 2018-03-01 spectrum shows no enhancement whatsoever. The 2018-03-02 spectrum, by contrast, exhibits a clear line profile, in addition to broad emission enhancement comparable to that seen in the 2017-11-04 spectrum.

4.8 Characteristics and Formation Mechanisms of Peter Pan Disks

Over the preceding sections, we have identified new Peter Pan disk systems, and further characterized known Peter Pan disks. Here, we use the accumulated information on these systems to identify the shared characteristics that define a Peter Pan disk system. Using this definition, we discuss five potential formation and evolution mechanisms that lead to the observed characteristics of these systems at their ages. We also consider the implications of the findings of Flaherty et al. (2019), indicating a lack of CO gas in the system. In the final subsection, we discuss various additional observations that could potentially be used to test these scenarios.

4.8.1 What is a Peter Pan Disk?

There are now eight systems with literature identifications in the Great Austral Young Association (GAYA) that have been claimed as accretion disk candidates. However, there are disagreements in the literature about these targets and their behaviors. With the sample of these targets now doubled thanks to this paper, we take this opportunity to define what observational characteristics constitute a Peter Pan disk, and which of these eight systems meet these criteria.

We define a Peter Pan disk as

1. a star or brown dwarf of mid-M or later spectral type,
2. at age > 35 Myr, based on membership in a ~ 45 Myr moving group
3. that exhibits substantial excess ($L_{\rm ir}/L_\star > 0.001$) at both 12 and 22 microns

4. and has a measurement of an accretion signature indicative of the presence of warm gas.

J0808 is the prototypical Peter Pan disk. Its kinematics and spectroscopic age indicators clearly place it at age ~ 45 Myr, it has a $L_{\rm ir}/L_\star \sim 0.15$ (Murphy et al., 2018), and its optical and near-IR spectra show clear evidence of accretion (Murphy et al., 2018, Section 4.7). Similarly, J0501 shows clear evidence of age ~ 45 Myr, $L_{\rm ir}/L_\star \sim 0.02$, and evidence of accretion from broad Hα emission.

While Gagné et al. (2014) identified J0441 as a likely member of Tucana-Horologium, Shkolnik et al. (2017) identify it as a likely member of the Beta Pictoris moving group. Given this uncertainty in the age of the system and the lack of a significant excess detection with WISE, we discard it from consideration as a Peter Pan disk. We also discard J0226, as it does not yet have a reliable measurement of accretion (its assessment as an accretion star is based only on a qualitative assessment of its near-IR spectroscopy, rather than a quantitative measurement).

While both J0446A and J0446B are high-likelihood members of Columba, the Hα measurements straddle the boundaries separating an accretion origin from an activity origin defined in the literature (White & Basri, 2003; Jayawardhana et al., 2003). Until accretion signatures that suffer less from origin confusion are measured (e.g. near-IR hydrogen emission, UV observations), we identify both targets as Peter Pan disks.

The J0949 system is more puzzling. Despite an angular separation of $1.49''$ and a physical distance of $\sim 1.10 \pm 0.47$ pc (Table 4.1), the proper motions of the two objects significantly differ. J0949B moves 3.039 ± 0.167 mas/yr faster than J0949A in right ascension, and $4.98. \pm 0.176$ mas/yr slower in declination. Thus, while J0949A has a membership likelihood in Carina of $> 99\%$, J0949B has

similar likelihood of membership in Carina, Lower Centaurus-Crux, and the field. The observed radial velocities make Carina more likely (per BANYAN Σ), but not overwhelmingly so. One possible explanation is that the observed proper motion difference is due to orbital motion of a bound binary system. It is not possible with the current data to determine if the system is bound, given the large relative uncertainties of the system; further observations to reduce these uncertainties will be necessary to confirm this possibility.

J0949B is clearly accreting, based on the presence of He I 6678Å emission and the strength and breadth of the Hα emission. While not as clear-cut, J0949A also shows evidence of accretion. We thus consider both of these stars Peter Pan disk candidates.

4.8.2 Characteristics of Known Peter Pan Disks

We list the observed characteristics of the six Peter Pan disk candidates in Table 4.4, including updated astrometry and moving group membership information for J0808 from *Gaia* DR2. Parallax and proper motion measurements for J0501 were not included in *Gaia* DR2, so we use the characteristics listed in Boucher et al. (2016). In addition to the astrometry, we list accretion rate measurements from both optical and near-IR spectroscopy, WISE colors, and best-fit SED model characteristics of the systems.

4.8.3 Origins for Peter Pan Disks

Below, we discuss six possible origins for Peter Pan disks. Some listed scenarios are non-physical for the specific examples in hand (ages $\sim$ 45 Myr), we include all of these scenarios to allow for the possible discovery of even older Peter Pan disks in the future.

Table 4.4. Collected Properties of Peter Pan Disks

Designation	J0808	J0501	J0446A	J0446B	J0949A	J0949B	Ref.
R.A. (h:m:s)[a]	08:08:22.182	05:01:00.889	04:46:34.105	04:46:34.249	09:49:00.753	09:49:00.441	1
Dec. (d:m:s)[a]	64:43:57.26	-43:37:09.96	-26:27:56.84	-26:27:55.57	-71:38:02.95	-71:38:03.16	1
Distance (pc)	101.4 ± 0.6	$(47.8^{+7.2}_{-8.4})$[b]	82.6 ± 0.4	82.2 ± 0.4	79.2 ± 0.5	78.1 ± 0.3	1,2
$\mu_\alpha \cos\delta$ (mas yr^{-1})	-11.539 ± 0.118		33.351 ± 0.084	33.534 ± 0.080	-36.096 ± 0.135	-39.135 ± 0.099	1,
μ_δ (mas yr^{-1})	25.615 ± 0.100		-5.459 ± 0.118	-3.629 ± 0.112	28.565 ± 0.131	23.582 ± 0.117	1,
RV (km s^{-1})	22.7 ± 0.5	19.6 ± 0.5	26.7 ± 16.8	29.8 ± 16.8	20.5 ± 16.8	22.4 ± 16.7	3,2,4
Spectral Type	M5	M4.5	M6	M6	M5	M4	3,2,4
Association	CAR	COL	COL	COL	CAR	CAR	5,2,4
Age (Myr)	45^{+11}_{-7}	42^{+6}_{-4}	42^{+6}_{-4}	42^{+6}_{-4}	45^{+11}_{-7}	45^{+11}_{-7}	6
$\log_{10}(\dot{M}_{\rm acc,H\alpha}$ ($M_\odot$ yr^{-1}))	$(-10)-(-9.5)$	$-10.80^{+0.07}_{-0.05}$	-10.9 ± 0.4	-10.6 ± 0.4	-9.9 ± 0.4	-9.3 ± 0.4	3,2,4
$\log_{10}(\dot{M}_{\rm acc,IR}$ ($M_\odot$ yr^{-1}))	(-12)-(-10.8)	...	...	...	...	...	4
[W1] − [W3] (mag)	2.445 ± 0.036	1.256 ± 0.039	1.146 ± 0.034		1.468 ± 0.027		4
[W1] − [W4] (mag)	4.312 ± 0.087	3.42 ± 0.08	3.093 ± 0.078		2.888 ± 0.043		5,2,4
$T_{\rm eff}$ (K)	3050 ± 100	3125	~ 2800	~ 2800	~ 3050	~ 3200	3,2,4
$T_{\rm disk,hot}$ (K)	1071 ± 103	...	...	...	...	...	3
$L_{\rm disk,hot}/L_\star$	$0.054 \pm 0.018[0...0.11]$[c]	...	...	...	...	...	3
$T_{\rm disk,warm}$ (K)	237 ± 11	170 ± 10	299^{+11}_{-9}		279^{+7}_{-6}		3,2,4

Table 4.4 (cont'd)

Designation	J0808	J0501	J0446A	J0446B	J0949A	J0949B	Ref.
$L_{\rm disk,warm}/L_\star$	0.070 ± 0.015	$0.021^{+0.002}_{-0.001}$	$0.0262^{+0.0006}_{-0.0008}$[d]		0.0178 ± 0.0003[d]		3,2,4
$T_{\rm disk,cold}$ (K)	> 20	...	...	...	...	...	7

[a]Right ascension and declination are the stellar positions at epoch J2015.5, the *Gaia* reference epoch.

[b]Statistical distance from Boucher et al. (2016).

[c]Approximate range from variability in W1 and W2 photometry (see Murphy et al., 2018).

[d]$L_{\rm ir}/L_\star$ calculated using combined flux from both stars.

Note. — (1) Gaia Collaboration et al. (2018) (2) Boucher et al. (2016) (3) Murphy et al. (2018) (4) This paper (5) Silverberg et al. (2016) (6) Bell et al. (2015) (7) Flaherty et al. (2019)

Star-Star and Star-Disk Interactions

Two potential explanations of "Peter Pan" disks would require close encounters with other stellar bodies. In one scenario, a disk could result from a close encounter with a star, either by acquiring the disk of the other star (e.g. Pfalzner et al., 2005), or from a close encounter generating new collisions of planetesimal-size objects, producing a new debris disk. In another, an M dwarf could collide with a lower-mass M dwarf or brown dwarf (e.g. Leonard & Livio, 1995). Assuming the expected timescale for primordial disk dissipation still applies in this scenario, the encounter must have taken place in the star's recent history, within $\sim$ 15 Myr. Such encounters with an unbound object are unlikely to occur with regularity outside of a tightly packed cluster. In particular, we are reluctant to consider the collision scenario as its hypothesis is non-falsifiable—there is, to our reckoning, no way to test whether the disk material was at one point a star or brown dwarf.

However, close encounters that produce new disk material might be expected in the case of a loosely bound binary system, such as may be the case with J0446 and J0949. Kaib et al. (2013) found that changes in the eccentricity of wide binary systems perturb the planetary systems they host for ages at least as young as the systems considered here, and well beyond. Such perturbations would also sculpt disk material. If the J0949 system is in fact bound, the observed excess and accretion in J0949B may be due to a past close encounter between J0949A and the remnants of the Kuiper belt analogue of J0949B that produced a new debris disk. One might hypothesize in this scenario that the observed accretion signature is from accretion of vaporized cometary material. However, the currently observed distance (1.10 ± 0.47 pc) is not close enough to stir up disk material in the same way.

Tidal disruption of a giant planet

In this scenario, the star is orbited by a large gas giant with a highly eccentric orbit (potentially due to planet-planet scattering), such that its periastron radius is less than the stellar Roche radius. Once it moved inside the Roche radius, the planet would be tidally disrupted, and the planetary material would move into a disk configuration.

However, this would require a giant planet at a very close radius. The Roche radius for J0808 and a planet with Neptune's density and radius is 2×10^{-4} AU, well inside the blackbody radius of the inner disk (as identified by Murphy et al., 2018). While it is plausible that such a situation might arise by chance around a single star, multiple occurrences of it would be exceedingly rare. Orbital disruption by a loosely bound companion in a binary system, alternatively, is a plausible mechanism for scattering a giant planet (Kaib et al., 2013) into a close enough approach to the host star to be tidally disrupted. This would suggest that Peter Pan disks formed by this mechanism are more likely to appear in binary star systems. There is a known correlation between binarity and the presence of a warm disk (Zuckerman, 2015); this would be a continuation of that correlation.

As the odds of multiple single star systems generating a disk by tidal disruption of a giant planet is low, one test of this hypothesis would be determining the occurrence frequency of Peter Pan disks, particularly in singlet systems. Additional sub-millimeter observations could also determine if the disk's gas and dust mass is consistent with a giant planet.

A disk due to a mass transfer binary

In this scenario, the M dwarf is the secondary in a binary system to a high-mass star which evolves. As this star exceeded its Roche lobe, gas from the star would

be transferred to the M dwarf, leaving behind a white dwarf/M dwarf binary system.

However, this scenario requires a "primary" star of high enough mass to evolve onto and off the main sequence in < 45 Myr, but low enough mass to evolve into a white dwarf, rather than producing a core-collapse supernova. As the main-sequence lifetime for a B1V star is ~ 45 Myr, this is physically impossible to explain the disks in Carina, Columba, and Tuc-Hor. However, it could potentially explain Peter Pan disks in even older groups, if those are ever identified.

An Evolved Debris Disk System with Large Grains

Recent observations of J0808 with ALMA (Flaherty et al., 2019) show optically-thin dust at 1.3 mm and no evidence of CO. This suggests that the system is not a true primordial disk, but rather a more evolved system.

Flaherty et al. (2019) discuss possible origins for the cold dust emission. In one scenario, Poynting-Robertson drag could pull large grains produced by planetesimal collisions inward to produce the large IR excess. In another, planetary-body collisions produce new dust, generating the substantial excess. Such a scenario has been argued as the source for infrared excess in field age ($\gtrsim 1$ Gyr) M dwarfs (Theissen & West, 2017). In either scenario, a disruption of the planetary system architecture could lead to planetesimals or planets falling into the host star, producing the observed accretion signature. However, this would require a recent planetary collision to produce the substantial amount of excess seen in the WISE data.

Slow Dissipation of Primordial Disks about Low-Mass Stars

The simplest explanation for the existence of Peter Pan disks is that, in general, M dwarfs simply dissipate their primordial disks less rapidly than higher mass stars.

This would extend the trend observed in stars more massive than M dwarfs, as disks around stars of masses $> 1.2 M_{\odot}$ dissipate in approximately half the time as stars with masses below this (e.g. Carpenter et al., 2006), likely due to their higher accretion rates (e.g. Calvet et al., 2005) and higher levels of X-ray photoevaporation (e.g. Owen et al., 2012). The low accretion rates identified in this work compared to other primordial disks around stars with similar masses (albeit with larger radii) would correspond to this difference, but on the low-mass end.

Using the observed primordial disk fraction of mid-late M dwarfs (spectral types later than M3.5) from Cody & Hillenbrand (2018), we estimate an e-folding timescale of ~ 9.3 Myr. Extrapolating to the ages of the groups considered here, we would expect an occurrence rate of Peter Pan disks of $\sim 1\%$ for Columba, and $\sim 0.8\%$ for Carina and Tucana-Horologium. It is likely that such systems have not been detected until now due to the lack of precise astrometry for late-type objects in the pre-*Gaia* era—one would expect that the low-mass ends of moving groups will be better characterized now that this data is available. Indeed, such progress is underway (e.g. Gagné & Faherty, 2018).

A long-lived primordial disk would be expected to exhibit cold gas, as well as dust. ALMA observations of J0808 (Flaherty et al., 2019) do not show any evidence of CO gas, the most common tracer. Flaherty et al. (2019) demonstrate that CO gas may photodissociate around M dwarfs on timescales less than the age of the system, suggesting that non-CO gas may still be present in the system. Additional observations are necessary to characterize the presence of non-CO gas (e.g. H_2O) in the system.

Alternatively, while Peter Pan disks *are* long-lived primordial disks, their lack of dissipation is *not* intrinsic to M-type primordial disks as a whole, but rather to *these specific* systems. For example, the systems might have been shielded from

high-energy radiation external to the system (e.g.), or their host stars produce less X-ray and UV radiation than is typical. While it would be difficult to characterize the birth environment of a $\sim$ 45-Myr moving group now, characterization of the activity of the hosts could provide insights into their activity earlier in their lifetimes.

4.8.4 Observational Methods of Testing Formation Mechanisms

Additional observations of Peter Pan disks could test several of these scenarios.

- *Radio/sub-mm obsevations*: Primordial disks are expected to have a substantial reservoir of cold material. Observations at sub-mm wavelengths in multiple bands would identify whether such a reservoir exists in these systems. Such observations would also enable estimation of the system's disk mass and gas content, which would directly test the tidal-disruption hypothesis—a disk more massive than the expected mass of a tidally disrupted giant planet would eliminate this possibility. If no gas is detected in the system, it could indicate a formation scenario closer to that described by Flaherty et al. (2019). Multiple bands are necessary to constrain the temperature of the emission, and to probe multiple molecules (e.g. CO and H_2O).

- *High-energy observations*: X-ray or UV spectroscopy of Peter Pan disks would yield information as to the composition of the accretion material. If the accretion material is the gas expected from a classical T Tauri star, that would provide support for the long-lived primordial disk hypothesis. An accretion material composition similar to vaporized exocometary material,

alternatively, would support the Flaherty et al. (2019) theory of an evolved disk, with substantial excesses in the WISE bands due to migration of large grains inward. Additionally, such observations might give a further clue as to the conditions that give rise to these systems.

Another driver of primordial disk dissipation is photoevaporation of the disk's gas content from far- and extreme-ultraviolet (FUV and EUV) radiation (e.g. Williams & Cieza, 2011). Studies of the low-mass population of the TW Hya association have shown an anti-correlation between X-ray luminosity and disk fraction as a function of spectral type; earlier M dwarfs have higher X-ray luminosities and a lower disk fraction than mid-late M dwarfs (Kastner et al., 2016). If Peter Pan disks are long-lived primordial disks, this observed anticorrelation with spectral type would provide an explanation for why they have not been detected around earlier spectral types.

- *High-resolution spectroscopy* Higher-resolution ($\gtrsim$ 7000) spectroscopy of a larger sample of optical Peter Pan disks would allow for the potential to firmly resolve accretion behavior in the spectral line (e.g. line asymmetries in Hβ Hartmann et al., 2016).

- *Mid-infrared spectroscopy*: Flaherty et al. (2019) note that observation of silica features could test the planetary-body collision hypothesis (Lisse et al., 2009). A monitoring campaign of such observations would also enable constraint of the variable excess detected in W1/W2.

- *Identification of additional examples*: The slowly-dispersing-primordial-disk and collisional-debris-disk hypotheses suggest that Peter Pan disks should be common. By identifying more systems that meet the age and infrared-excess criteria, we can test their frequency of occurrence, which would directly

test these hypotheses against the more exotic scenarios presented here (disk acquisition, planetary tidal disruption).

4.9 Summary

In this paper, we define the observational characteristics of a Peter Pan disk: a mid-M or later star or brown dwarf with a substantial, warm excess, at a stellar age > 20 Myr, and exhibiting ongoing accretion. We present four new identifications of potential Peter Pan disks, based on a crossmatch of *Gaia* DR2 with the Disk Detective input catalog and testing objects with the BANYAN Σ software. We presented high-cadence photometric observations of WISEA J0808, the prototypical Peter Pan disk, with the CTIO 0.9m telescope and TESS. We find that the star has some flare activity, and exhibits some dipping events, attributable to disk occultations. We also present high-cadence TESS photometry of 2MASS J0501, another Peter Pan disk, showing that it has a persistent starspot or starspot complex, and has active flare activity. Using the period from the TESS observations and a projected rotational velocity from the literature (Boucher et al., 2016), we find the star to have an inclination angle of $\sim 38°$. We present near-infrared spectroscopy of J0808 over six months, showing low-level accretion variable on 24-hour timescales. With these observations in mind, we discussed several potential formation mechanisms for these systems, before concluding that the two most likely mechanisms were long-lived primordial disks, and evolved dust disks with large grains drawn inward toward the host star to produce the observed WISE excess.

Flaherty et al. (2019) noted that J0808 was an oddity, given its substantial excess and ongoing accretion. The identification of four new candidate systems with similar characteristics, in addition to the four known Peter Pan disks, throws this categorization into question. It seems plausible that that the observed dearth

of disks of this sort is instead due to the limits of observation, rather than an actual dearth of such systems. As *Gaia* measures the astrometry of more low-mass stars, more low-mass moving group members will be identified, enabling further identification of such systems.

Despite the "drain-the-lake" approach to disk identification that Disk Detective adopts, M dwarf disks remain elusive. However, Peter Pan disks as a class would not necessarily have been identified without such an approach, as the systems identified thus far would not have been included in a typical WISE disk search. With the new resources that have become available since the launch of Disk Detective, such as Pan-STARRS (Chambers et al., 2016) and unWISE (Lang, 2014), updates to the project may significantly increase the yield of Peter Pan disks in the near future.

Chapter 5

Conclusions and Future Work

Circumstellar disks are key signposts of exoplanetary systems. While many have already been identified in full-sky searches with IRAS and AKARI, and in pointed searches with *Spitzer*, more are waiting to be identified in the AllWISE catalog. However, the colors of debris and protoplanetary disks in the WISE catalog are similar to those of other non-disk phenomena, and the large point spread function of the 22 μm WISE band produces blending of close sources. Visual inspection of all WISE excesses in all available bandpasses is necessary to confirm excess sources as disk candidates.

The Disk Detective project uses citizen science to provide this visual inspection. Via a website interface, participants search through WISE sources with infrared excesses indicative of circumstellar material, with the goal of eliminating false positives and revealing a plethora of new disks. In this thesis, we presented the results of two specific facets of the Disk Detective project: a large-scale statistical analysis of in-progress classifications to estimate the eventual yield of our disk search, and the discovery and characterization of WISEA J080822.18-644357.3, which we used to define a new class of long-lived accretion disk (Peter Pan disks).

5.1 Estimation of False-Positive Rates from Citizen Scientist Classification and Follow-Up Imaging

In Silverberg et al. (2018), we presented the results thus far of our website classification and imaging follow-up campaigns. We found that only $9.80\% \pm 0.08\%$ of subjects in the Disk Detective input catalog are classified as "None of the

Above/Good Candidate" by a majority of classifiers—90.20% of the subjects with completed classifications are false positives. A majority of classifiers selected "Multiple Objects in the Red Circle" for 68.87% of targets, making potential W4 blends the predominant form of false positive. As expected, these classifications depended on Galactic latitude and longitude—multiples are most common in the Galactic plane, and at the positions of the Large and Small Magellanic Clouds. Of the subjects that passed online classification, 86% became DDOIs after literature review.

We collected high-resolution images of 261 DDOIs with the Robo-AO instrument on the 1.5m telescope at Mount Palomar and the 2.5m Ireneé R. Du Pont Telescope at Las Campañas Observatory to identify background objects fainter than could be detected by the survey data used on the Disk Detective website, but bright enough to significantly affect the observed W4 excess. We found that 17 of the DDOIs were affected in this way, for a false positive rate of 6.5%. Combining these three methods of evaluation, we determined that only 7.9% of objects in the Disk Detective input catalog will become good candidates, suggesting a final yield of $\sim 21,600$ new disks. Based on our statistics, we find that surveys that do not visually inspect the WISE images and do not consider the effects of multiple objects within the W4 PSF will have lower limit false positive rates of $\sim 69\%$. Surveys that do inspect the WISE images but do not also collect high-resolution follow-up images will have false positive rates of $4 - 8\%$.

We applied the Disk Detective methodology to the M dwarf disk search of Theissen & West (2014), finding that all thirteen of their disk candidates with W4 signal sufficient for the Disk Detective methodology to apply were false positives. This further underscores the challenges of identifying M dwarf debris disks with WISE.

We presented 244 new disk candidates, vetted through visual inspection by citizen scientists and high-resolution follow-up imaging. Twelve of these appeared in comoving pairs. We identified WISEA J191845.28+371449.2 as a potential "extreme" debris disk. We also noted that 31 of these systems lie within 125 pc, making them good targets for adaptive-optics and coronagraphic imaging.

5.2 WISEA J080822.18-644357.3 and Peter Pan Disks

Using the BANYAN II software as applied to a list of DDOIs, we identified WISEA J080822.18-644357.3 as a likely member of the 45-Myr Carina association based on its position and proper motion. We identified the system as an M5.5V dwarf with a strong infrared excess around this target, indicative of an unexpectedly substantial disk given its age. We presented this discovery in Silverberg et al. (2016) and Chapter 3.

Subsequent follow-up observations by Murphy et al. (2018) confirmed the system's age, and demonstrated that the system exhibited a variable excess in the W1/2 bands and accretion activity onto the star, suggesting that the system was a primordial disk. However, Flaherty et al. (2019) detected continuum dust, but no CO gas, in the system, suggesting a gas-poor debris disk.

Using *Gaia* DR2 and the BANYAN Σ tool, we identified two WISE objects with kinematics and photometry consistent with Peter Pan disks—large infrared excess around M stars at ages $\sim$ 45 Myr. Further review showed that each of these was an apparent visual double—two stars within the 2MASS and WISE PSF—and that substantial infrared excess was present even after taking both stellar components into account. We obtained follow-up optical spectra of all four stars from the GMOS instrument at Gemini-South. All four stars have mid-M spectral types, Na I absorption profiles consistent with youth, and radial velocities

consistent with membership in Columba and Carina. J0949B shows the clearest evidence of accretion, but all four stars have Hα profiles suggestive of accretion. Further observation of these systems is necessary to isolate which star in each system the WISE excess is associated with (if not both). These systems suggest that Peter Pan disks may be more common than previously hypothesized.

We presented high-cadence optical photometry of J0808 with the 0.9m telescope at CTIO, and TESS. While a Lomb-Scargle periodogram of the CTIO data indicates a strong period, the actual light curve is aperiodic, as is the light curve of J0808 from TESS. We also find that while the CTIO light curve appears to have more "bursting" events, the TESS light curve exhibits more "dipping" events. We hypothesize that this is due to the nightly observing window of the CTIO data, as the dips in the TESS light curve are on timescales of half a day to days, coincident with the observing window. In addition, we find that the high-cadence light curve of J0501, another Peter Pan disk first discovered by Boucher et al. (2016), is dominated by periodicity characteristic of a persistent starspot. Using the observed 0.906-day period and the Boucher et al. (2016) projected rotational velocity, we find an inclination angle for the system of $i \approx 38°$.

We also present three near-IR spectra of J0808, collected over five months, which show variable accretion on the order of $-12 < \log \dot{M} < -10.8$, an order of magnitude lower than that found by Murphy et al. (2018). Using these observations, we define a class of "Peter Pan" disks, disks around M dwarfs that exhibit substantial excess in WISE bands and ongoing accretion at ages > 5 times the characteristic timescale for dissipation of such disks around solar-type stars. While there are several possibilities, we find that the most likely possibilities are a longer timescale for disk dissipation and planet formation around M dwarfs than previously hypothesized, and a "typical" debris disk with micron-sized grains pulled inward by Poynting-Robertson drag to produce the substantial excess shown.

The possibility of an extended timescale for disk dissipation around M dwarfs is intriguing, as it directly leads to a longer timescale for planet formation around M dwarfs than previously theorized. This could have significant effects on the eventual habitability of M dwarf exoplanets, as M dwarf activity (e.g. flares) diminishes as the stars age (e.g. Wright et al., 2018). If planets were to form at an older age, they would receive less energy from flares, which would imply lower planetary atmospheric erosion rates, different atmospheric chemistry, and potentially an atmosphere more favorable for habitability than that of a planet receiving more high-energy flares from a more active, younger M dwarf. A long-lived primordial disk could lead to eccentricity dampening of the orbits of forming planetesimals, and convergent migration (Ogihara & Ida, 2009), which could result in resonant chains of compact, near-circular orbits, as seen in TRAPPIST-1 (Gillon et al., 2017; Quarles et al., 2017).

5.3 Future Work: Peter Pan Disks, M Dwarfs, and a Relaunched Disk Detective

Disk Detective was originally designed to identify the most typically-discovered debris disks, those around main-sequence A stars. While it has been incredibly productive, this design choice resulted in the likely exclusion of other potentially interesting targets, such as M dwarf debris disks. Due to the intrinsic faintness of M dwarfs and the shallowness of the W4 bandpass, such systems are unlikely to meet the W4 SNR > 10 criterion imposed on the Disk Detective input catalog. In particular, the Disk Detective input catalog does not include AU Mic, the most notorious M dwarf debris disk, for multiple reasons, including not meeting the W4 SNR requirement.

In the five years since Disk Detective launched, several new data sets have

become available that, had they been available at site launch, would have significantly impacted the site's capabilities. In particular, with the advent of *Gaia* DR2, it is possible to include fast-moving nearby systems that did not have a good 2MASS cross-match in the AllWISE catalog. A *Gaia*-based 2MASS/AllWISE cross-match would include systems whose proper motion exceeds the 0.3″ cross-match radius used in AllWISE, such as AU Mic. Identifying targets using *Gaia* also allows an early approximate characterization of the star's spectral type and luminosity class, helping to weed out dust-producing M giants.

The release of data from Pan-STARRS has also provided optical images of the majority of the sky with excellent spatial resolution, improving on both SDSS and DSS, the two surveys used for optical wavelengths in Disk Detective. This would allow more accurate identification of multiple sources within the W4 PSF, and would enable a better characterization of how much of the W4 flux is due to background point sources.

To this end, I designed an updated Disk Detective, incorporating these components and other pitfalls identified through Disk Detective 1.0. This redesign differs from the original by:

- *Using the new Zooniverse Project Builder.* Since Disk Detective launch, Zooniverse has debuted a tool for quickly starting new projects. Using this tool will enable a rapid project launch.

- *Identifying sources via Gaia astrometry.* Rather than only using targets that have a 2MASS match in AllWISE, use *Gaia* DR2's matches to 2MASS and AllWISE to assemble targets, enabling study of high-proper-motion (> 0.3 mas/yr) sources.

- *Pre-selecting likely objects of high interest.* Begin by analyzing IR-excess objects in the M dwarf locus of a *Gaia* Hertzprung-Russell diagram, with

high likelihood of membership in > 20 Myr moving groups per BANYAN Σ, to rapidly identify likely Peter Pan disks; after these, analyze other M dwarf excess objects and moving group members. This ensures that Peter Pan disk candidates are identified first, followed by M dwarfs that may be members of newly-identified moving groups.

- *Replacing DSS2/SDSS with Pan-STARRS and Skymapper.* Rather than using the photographic plate scans of the Digitized Sky Survey, use Pan-STARRS DR1 and Skymapper Release 1.1 images. Skymapper and Pan-STARRS provide more wavelength coverage than DSS2, useful for estimating spectral types. Pan-STARRS images have typical seeing $< 1.2''$ (Chambers et al., 2016), improving on DSS2's $\sim 3''$ seeing. In conjunction, highlight both the W1 and W4 PSF on the website postage stamp images. Excess is determined from [W1]-[W4] color; if multiple sources are blended within the W1 PSF, the system could potentially exhibit an excess in addition to a low separation visual double.

- *Using unWISE coadds rather than AllWISE atlas images.* The AllWISE image atlas was blurred by convolving the images with a model PSF, increasing the nominal W1/W2/W3 PSF width from $6''$ to $8.5''$ (Lang, 2014), with a larger change at W4. unWISE (Lang, 2014) provides unblurred coadds that preserve the WISE images' spatial resolution. These images will enable better assessment of extended emission beyond the W4 PSF, likely due to ISM.

- *Lowering the W4 SNR threshold.* Requiring W4 SNR > 10 effectively imposes a magnitude limit [W4] ≈ 7.283 (based on the average SNR=10 magnitude across all AllWISE tiles), biasing the survey against intrinsically fainter M dwarfs. However, the vast majority of false positives in WISE are

due to multiple point sources within the W4 PSF (Silverberg et al., 2018), unrelated to the W4 SNR. Lowering the requirement to a still-robust W4 SNR>5, for a limiting magnitude [W4] ≈ 8.0, will include more faint targets in the search, while the other improvements should counterbalance any increase in false positives due to a lowered W4 SNR requirement.

- *Pre-evaluating targets via AI.* Disk Detective has used user classifications to train a convolutional neural network, which yields a probability that a given object is a good candidate. These results do not match the performance of by-eye inspection, but can be used to "pre-evaluate" IR excess candidates and prioritize high-probability objects for visual inspection, yielding better target lists faster than a random process.

These improvements will allow for rapid identification of likely high-priority disk candidates (e.g. Peter Pan disks, M dwarf debris disks), and allow for more robust characterization of targets prior to follow-up observations. These changes would also double the volume probed for disks in the AllWISE catalog, while improving full-sky survey data sensitivity. This relaunch is expected in August 2019.

Citizen science is a versatile method for carrying out analysis of large surveys. As astronomy increasingly becomes dominated by large surveys with correspondingly large datasets (e.g. TESS, LSST, WFIRST), judicious use of citizen science will be an invaluable way to analyze and characterize new data. Disk Detective has already yielded new and unexpected disk populations, and provided us with a plethora of targets for further observation and analysis; the ongoing work of citizen scientists analyzing these data will almost certainly provide more targets, and provide us further insights into the formation and evolution of exoplanets and circumstellar disks.

References

Abt, H. A. 2009, ApJS, 180, 117

Akeson, R. L., Ciardi, D. R., Millan-Gabet, R., et al. 2009, ApJ, 691, 1896

Alcala, J. M., Terranegra, L., Wichmann, R., et al. 1996, A&AS, 119, 7

Andrews, S. M., & Williams, J. P. 2005, ApJ, 631, 1134

Anglada, G., Amado, P. J., Ortiz, J. L., et al. 2017, ApJ, 850, L6

Anglada-Escudé, G., Amado, P. J., Barnes, J., et al. 2016, Nature, 536, 437

Aumann, H. H., Beichman, C. A., Gillett, F. C., et al. 1984, ApJ, 278, L23

Avenhaus, H., Schmid, H. M., & Meyer, M. R. 2012, A&A, 548, A105

Ballering, N. P., Rieke, G. H., Su, K. Y. L., & Montiel, E. 2013, ApJ, 775, 55

Baraffe, I., Homeier, D., Allard, F., & Chabrier, G. 2015, A&A, 577, A42

Baranec, C., Riddle, R., Law, N. M., et al. 2013, Journal of Vibration Engineering, 72, 50021

—. 2014, ApJ, 790, L8

Barclay, T., Pepper, J., & Quintana, E. V. 2018, ApJS, 239, 2

Barentsen, G., Vink, J. S., Drew, J. E., et al. 2011, MNRAS, 415, 103

Barrie, J. M. 1904, Peter Pan (Project Gutenberg)

Bell, C. P. M., Mamajek, E. E., & Naylor, T. 2015, MNRAS, 454, 593

Biller, B. A., Liu, M. C., Wahhaj, Z., et al. 2013, ApJ, 777, 160

Binks, A. 2016, in IAU Symposium, Vol. 314, Young Stars & Planets Near the Sun, ed. J. H. Kastner, B. Stelzer, & S. A. Metchev, 159–162

Binks, A. S., & Jeffries, R. D. 2017, MNRAS, 469, 579

Boccaletti, A., Thalmann, C., Lagrange, A.-M., et al. 2015, Nature, 526, 230

Bonfils, X., Gillon, M., Forveille, T., et al. 2011, A&A, 528, A111

Borucki, W. J., Koch, D., Basri, G., et al. 2010, Science, 327, 977

Boucher, A., Lafrenière, D., Gagné, J., et al. 2016, ApJ, 832, 50

Brandt, T. D., Kuzuhara, M., McElwain, M. W., et al. 2014, ApJ, 786, 1

Calvet, N., Briceño, C., Hernández, J., et al. 2005, AJ, 129, 935

Carpenter, J. M., Mamajek, E. E., Hillenbrand, L. A., & Meyer, M. R. 2006, ApJ, 651, L49

Carpenter, J. M., Bouwman, J., Mamajek, E. E., et al. 2009, ApJS, 181, 197

Chambers, K. C., Magnier, E. A., Metcalfe, N., et al. 2016, ArXiv e-prints, arXiv:1612.05560

Chen, C. H., Mittal, T., Kuchner, M., et al. 2014, ApJS, 211, 25

Chen, C. H., Pecaut, M., Mamajek, E. E., Su, K. Y. L., & Bitner, M. 2012, ApJ, 756, 133

Chen, P. S., Shan, H. G., & Zhang, P. 2016, New A, 44, 1

Clarke, A. J., Oudmaijer, R. D., & Lumsden, S. L. 2005, MNRAS, 363, 1111

Cody, A. M., & Hillenbrand, L. A. 2018, AJ, 156, 71

Cody, A. M., Stauffer, J., Baglin, A., et al. 2014, AJ, 147, 82

Collins, K. A., Kielkopf, J. F., Stassun, K. G., & Hessman, F. V. 2017, AJ, 153, 77

Corbally, C. J., & Straižys, V. 2009, Baltic Astronomy, 18, 1

Cotten, T. H., & Song, I. 2016, ApJS, 225, 15

Cruz-Saenz de Miera, F., Chavez, M., Bertone, E., & Vega, O. 2014, MNRAS, 437, 391

Currie, T., Daemgen, S., Debes, J., et al. 2014, ApJL, 780, L30

Currie, T., Lisse, C. M., Kuchner, M., et al. 2015, ApJL, 807, L7

Cushing, M. C., Vacca, W. D., & Rayner, J. T. 2004, PASP, 116, 362

Cutri, R. M., & et al. 2013, VizieR Online Data Catalog, 2328

Davenport, J. R. A., Hebb, L., & Hawley, S. L. 2015, ApJ, 806, 212

Davenport, J. R. A., Hawley, S. L., Hebb, L., et al. 2014, ApJ, 797, 122

Deacon, N. R., Schlieder, J. E., Olofsson, J., Johnston, K. G., & Henning, T. 2013, MNRAS, 434, 1117

Debes, J. H., Hoard, D. W., Farihi, J., et al. 2012, ApJ, 759, 37

Debes, J. H., Hoard, D. W., Kilic, M., et al. 2011, ApJ, 729, 4

Dressing, C. D., & Charbonneau, D. 2013, ApJ, 767, 95

Epchtein, N., de Batz, B., Capoani, L., et al. 1997, The Messenger, 87, 27

ESA, ed. 1997, ESA Special Publication, Vol. 1200, The HIPPARCOS and TYCHO catalogues. Astrometric and photometric star catalogues derived from the ESA HIPPARCOS Space Astrometry Mission

Espaillat, C., Calvet, N., D'Alessio, P., et al. 2007, ApJ, 670, L135

Espaillat, C., D'Alessio, P., Hernández, J., et al. 2010, ApJ, 717, 441

Esplin, T. L., Luhman, K. L., & Mamajek, E. E. 2014, ApJ, 784, 126

Esplin, T. L., Luhman, K. L., Miller, E. B., & Mamajek, E. E. 2018, AJ, 156, 75

Evans, II, N. J., Allen, L. E., Blake, G. A., et al. 2003, PASP, 115, 965

Evans, II, N. J., Dunham, M. M., Jørgensen, J. K., et al. 2009, ApJS, 181, 321

Fang, M., van Boekel, R., Wang, W., et al. 2009, A&A, 504, 461

Flaherty, K., Hughes, A. M., Mamajek, E. E., & Murphy, S. J. 2019, ApJ, 872, 92

Forbrich, J., Lada, C. J., Muench, A. A., & Teixeira, P. S. 2008, ApJ, 687, 1107

Foreman-Mackey, D., Conley, A., Meierjurgen Farr, W., et al. 2013, emcee: The MCMC Hammer, Astrophysics Source Code Library, , , ascl:1303.002

Gagné, J., & Faherty, J. K. 2018, ApJ, 862, 138

Gagné, J., Lafrenière, D., Doyon, R., Malo, L., & Artigau, É. 2014, ApJ, 783, 121

Gagné, J., Mamajek, E. E., Malo, L., et al. 2018, ApJ, 856, 23

Gaia Collaboration, Brown, A. G. A., Vallenari, A., et al. 2016, A&A, 595, A2

—. 2018, A&A, 616, A1

Gershberg, R. E. 1972, Ap&SS, 19, 75

Gillon, M., Triaud, A. H. M. J., Demory, B.-O., et al. 2017, Nature, 542, 456

Girard, T. M., van Altena, W. F., Zacharias, N., et al. 2011, AJ, 142, 15

Greaves, J. S. 2010, MNRAS, 409, L44

Guieu, S., Rebull, L. M., Stauffer, J. R., et al. 2010, ApJ, 720, 46

Hartmann, L., Herczeg, G., & Calvet, N. 2016, ARA&A, 54, 135

Hawley, S. L., Davenport, J. R. A., Kowalski, A. F., et al. 2014, ApJ, 797, 121

Heng, K., & Malik, M. 2013, MNRAS, 432, 2562

Hernández, J., Calvet, N., Hartmann, L., et al. 2005, AJ, 129, 856

Høg, E., Fabricius, C., Makarov, V. V., et al. 2000, A&A, 355, L27

Hoogerwerf, R. 2000, MNRAS, 313, 43

Horch, E. P., Gomez, S. C., Sherry, W. H., et al. 2011, AJ, 141, 45

Howard, A. W., Marcy, G. W., Bryson, S. T., et al. 2012, ApJS, 201, 15

Hube, D. P. 1981, A&AS, 44, 59

Irwin, J., Charbonneau, D., Nutzman, P., & Falco, E. 2009, in IAU Symposium, Vol. 253, Transiting Planets, ed. F. Pont, D. Sasselov, & M. J. Holman, 37–43

Ishihara, D., Onaka, T., Kataza, H., et al. 2010, A&A, 514, A1

Jayawardhana, R., Mohanty, S., & Basri, G. 2003, ApJ, 592, 282

Jenkins, J. M., Twicken, J. D., McCauliff, S., et al. 2016, in Proc. SPIE, Vol. 9913, Software and Cyberinfrastructure for Astronomy IV, 99133E

Kaib, N. A., Raymond, S. N., & Duncan, M. 2013, Nature, 493, 381

Kalas, P., Liu, M. C., & Matthews, B. C. 2004, Science, 303, 1990

Kalas, P., Graham, J. R., Chiang, E., et al. 2008, Science, 322, 1345

Kasper, M., Apai, D., Janson, M., & Brandner, W. 2007, A&A, 472, 321

Kastner, J. H., Principe, D. A., Punzi, K., et al. 2016, AJ, 152, 3

Kennedy, G. M., & Wyatt, M. C. 2010, MNRAS, 405, 1253

—. 2012, MNRAS, 426, 91

—. 2013, MNRAS, 433, 2334

Kenyon, S. J., & Bromley, B. C. 2002, ApJ, 577, L35

Kenyon, S. J., & Hartmann, L. 1995, ApJS, 101, 117

Kesseli, A. Y., West, A. A., Veyette, M., et al. 2017, The Astrophysical Journal Supplement Series, 230, 16

Kim, K. H., Watson, D. M., Manoj, P., et al. 2009, ApJ, 700, 1017

Koenig, X., Hillenbrand, L. A., Padgett, D. L., & DeFelippis, D. 2015, AJ, 150, 100

Koenig, X. P., Allen, L. E., Gutermuth, R. A., et al. 2008, ApJ, 688, 1142

Koenig, X. P., & Leisawitz, D. T. 2014, ApJ, 791, 131

Koenig, X. P., Leisawitz, D. T., Benford, D. J., et al. 2012, ApJ, 744, 130

Kohoutek, L., & Wehmeyer, R. 1999, A&AS, 134, 255

Kowalski, A. F., Hawley, S. L., Wisniewski, J. P., et al. 2013, ApJS, 207, 15

Kuchner, M. J., Silverberg, S. M., Bans, A. S., et al. 2016, ApJ, 830, 84

Lacy, C. H., Moffett, T. J., & Evans, D. S. 1976, ApJS, 30, 85

Lada, C. J. 1987, in IAU Symposium, Vol. 115, Star Forming Regions, ed. M. Peimbert & J. Jugaku, 1–17

Lagrange, A.-M., Bonnefoy, M., Chauvin, G., et al. 2010, Science, 329, 57

Lang, D. 2014, AJ, 147, 108

Lawson, K. D., Wisniewski, J. P., Bellm, E. C., Kowalski, A. F., & Shupe, D. L. 2019, arXiv e-prints, arXiv:1903.03240

Leonard, P. J. T., & Livio, M. 1995, ApJ, 447, L121

Lestrade, J.-F., Wyatt, M. C., Bertoldi, F., Menten, K. M., & Labaigt, G. 2009, A&A, 506, 1455

Lestrade, J.-F., Matthews, B. C., Sibthorpe, B., et al. 2012, A&A, 548, A86

Lindegren, L., Lammers, U., Bastian, U., et al. 2016, A&A, 595, A4

Lintott, C. J., Schawinski, K., Slosar, A., et al. 2008, MNRAS, 389, 1179

Lisse, C. M., Chen, C. H., Wyatt, M. C., et al. 2009, ApJ, 701, 2019

Liu, W. M., Padgett, D. L., Leisawitz, D., Fajardo-Acosta, S., & Koenig, X. P. 2011, ApJ, 733, L2

Liu, W. M., Padgett, D. L., Terebey, S., et al. 2014, AJ, 147, 133

Lomb, N. R. 1976, Ap&SS, 39, 447

López-Santiago, J., Montes, D., Crespo-Chacón, I., & Fernández-Figueroa, M. J. 2006, ApJ, 643, 1160

Luhman, K. L., Hernández, J., Downes, J. J., Hartmann, L., & Briceño, C. 2008, ApJ, 688, 362

Luhman, K. L., & Mamajek, E. E. 2012, ApJ, 758, 31

MacGregor, M. A., Weinberger, A. J., Wilner, D. J., Kowalski, A. F., & Cranmer, S. R. 2018, ApJ, 855, L2

Malo, L., Doyon, R., Lafrenière, D., et al. 2013, ApJ, 762, 88

Marois, C., Macintosh, B., Barman, T., et al. 2008, Science, 322, 1348

Marois, C., Zuckerman, B., Konopacky, Q. M., Macintosh, B., & Barman, T. 2010, Nature, 468, 1080

Marton, G., Tóth, L. V., Paladini, R., et al. 2016, MNRAS, 458, 3479

McClure, M. K., Furlan, E., Manoj, P., et al. 2010, ApJS, 188, 75

McDonald, I., Zijlstra, A. A., & Boyer, M. L. 2012, MNRAS, 427, 343

McDonald, I., Zijlstra, A. A., & Watson, R. A. 2017, MNRAS, 471, 770

Megeath, S. T., Gutermuth, R., Muzerolle, J., et al. 2012, AJ, 144, 192

Melis, C., Zuckerman, B., Rhee, J. H., et al. 2013, ApJ, 778, 12

Meng, H. Y. A., Su, K. Y. L., Rieke, G. H., et al. 2015, ApJ, 805, 77

Merrill, P. W., & Burwell, C. G. 1943, ApJ, 98, 153

—. 1950, ApJ, 112, 72

Morey, É., & Lestrade, J.-F. 2014, A&A, 565, A58

Murphy, S. J., Mamajek, E. E., & Bell, C. P. M. 2018, MNRAS, 476, 3290

Muzerolle, J., Hartmann, L., & Calvet, N. 1998, AJ, 116, 2965

Najita, J. R., Strom, S. E., & Muzerolle, J. 2007, MNRAS, 378, 369

Natta, A., Testi, L., Muzerolle, J., et al. 2004, A&A, 424, 603

Nesvold, E. R., & Kuchner, M. J. 2015, ApJ, 798, 83

Ogihara, M., & Ida, S. 2009, ApJ, 699, 824

Oh, S., Price-Whelan, A. M., Hogg, D. W., Morton, T. D., & Spergel, D. N. 2017, AJ, 153, 257

Osborn, H. P., Rodriguez, J. E., Kenworthy, M. A., et al. 2017, MNRAS, 471, 740

Owen, J. E., Clarke, C. J., & Ercolano, B. 2012, MNRAS, 422, 1880

Padgett, D. L., Cieza, L., Stapelfeldt, K. R., et al. 2006, ApJ, 645, 1283

Papovich, C., Dole, H., Egami, E., et al. 2004, ApJS, 154, 70

Patel, R. I., Metchev, S. A., & Heinze, A. 2014, ApJS, 212, 10

—. 2015, ApJS, 220, 21

Patel, R. I., Metchev, S. A., Heinze, A., & Trollo, J. 2017, AJ, 153, 54

Pecaut, M. J., & Mamajek, E. E. 2013, ApJS, 208, 9

—. 2016, MNRAS, 461, 794

Perryman, M. A. C., de Boer, K. S., Gilmore, G., et al. 2001, A&A, 369, 339

Pfalzner, S., Umbreit, S., & Henning, T. 2005, ApJ, 629, 526

Plavchan, P., Jura, M., & Lipscy, S. J. 2005, ApJ, 631, 1161

Plavchan, P., Werner, M. W., Chen, C. H., et al. 2009, ApJ, 698, 1068

Plavchan, P., Gao, P., Gagne, J., et al. 2017, in American Astronomical Society Meeting Abstracts, Vol. 229, American Astronomical Society Meeting Abstracts #229, 320.04

Quarles, B., Quintana, E. V., Lopez, E., Schlieder, J. E., & Barclay, T. 2017, ApJL, 842, L5

Rajpurohit, A. S., Reylé, C., Allard, F., et al. 2013, A&A, 556, A15

Rapson, V. A., Pipher, J. L., Gutermuth, R. A., et al. 2014, ApJ, 794, 124

Rayner, J. T., Cushing, M. C., & Vacca, W. D. 2009, ApJSS, 185, 289

Rebull, L. M., Hillenbrand, L. A., Strom, S. E., et al. 2000, AJ, 119, 3026

Rebull, L. M., Koenig, X. P., Padgett, D. L., et al. 2011, ApJS, 196, 4

Reiners, A. 2009, ApJL, 702, L119

Rheault, J.-P., Mondrik, N. P., DePoy, D. L., Marshall, J. L., & Suntzeff, N. B. 2014, in Proc. SPIE, Vol. 9147, Ground-based and Airborne Instrumentation for Astronomy V, 91475L

Riaz, B., & Gizis, J. E. 2008, ApJ, 681, 1584

Richert, A. J. W., Lyra, W., & Kuchner, M. J. 2018, ApJ, 856, 41

Ricker, G. R., Winn, J. N., Vanderspek, R., et al. 2014, in Proc. SPIE, Vol. 9143, Space Telescopes and Instrumentation 2014: Optical, Infrared, and Millimeter Wave, 914320

Rizzuto, A. C., Ireland, M. J., & Zucker, D. B. 2012, MNRAS, 421, L97

Rodríguez, E., López-González, M. J., & López de Coca, P. 2000, Astronomy and Astrophysics Supplement Series, 144, 469

Rojas, G., Gregorio-Hetem, J., & Hetem, A. 2008, MNRAS, 387, 1335

Sanchez, N., Inés Gómez de Castro, A., Lopez-Martinez, F., & López-Santiago, J. 2014, A&A, 572, A89

Scargle, J. D. 1982, ApJ, 263, 835

Schlawin, E., Herter, T. L., Henderson, C., et al. 2014, in Proc. SPIE, Vol. 9147, Ground-based and Airborne Instrumentation for Astronomy V, 91472H

Schlieder, J. E., Lépine, S., Rice, E., et al. 2012, AJ, 143, 114

Schneider, A., Melis, C., & Song, I. 2012a, ApJ, 754, 39

Schneider, A., Song, I., Melis, C., Zuckerman, B., & Bessell, M. 2012b, ApJ, 757, 163

Schneider, G., Grady, C. A., Hines, D. C., et al. 2014, AJ, 148, 59

Shkolnik, E. L., Allers, K. N., Kraus, A. L., Liu, M. C., & Flagg, L. 2017, AJ, 154, 69

Silverberg, S. M., Kuchner, M. J., Wisniewski, J. P., et al. 2016, ApJ, 830, L28

—. 2018, ApJ, 868, 43

Skrutskie, M. F., Cutri, R. M., Stiening, R., et al. 2006, AJ, 131, 1163

Smith, B. A., & Terrile, R. J. 1984, Science, 226, 1421

Stauffer, J., Cody, A. M., Baglin, A., et al. 2014, AJ, 147, 83

Strom, K. M., Strom, S. E., Edwards, S., Cabrit, S., & Skrutskie, M. F. 1989, AJ, 97, 1451

Su, K. Y. L., Rieke, G. H., Stansberry, J. A., et al. 2006, ApJ, 653, 675

Su, K. Y. L., Rieke, G. H., Stapelfeldt, K. R., et al. 2009, ApJ, 705, 314

Tabeshian, M., & Wiegert, P. A. 2017, ApJ, 847, 24

Theissen, C. A., & West, A. A. 2014, ApJ, 794, 146

—. 2017, AJ, 153, 165

Torres, C. A. O., Quast, G. R., da Silva, L., et al. 2006, A&A, 460, 695

Torres, C. A. O., Quast, G. R., de La Reza, R., et al. 2003, in Astrophysics and Space Science Library, Vol. 299, Astrophysics and Space Science Library, ed. J. Lépine & J. Gregorio-Hetem, 83

Torres, C. A. O., Quast, G. R., Melo, C. H. F., & Sterzik, M. F. 2008, Young Nearby Loose Associations, ed. B. Reipurth, 757

Urban, L. E., Rieke, G., Su, K., & Trilling, D. E. 2012, ApJ, 750, 98

Vacca, W. D., Cushing, M. C., & Rayner, J. T. 2003, PASP, 115, 389

van Dokkum, P. G. 2001, PASP, 113, 1420

van Leeuwen, F. 2007, A&A, 474, 653

Vega, O., Clemens, M. S., Bressan, A., et al. 2008, A&A, 484, 631

Vieira, S. L. A., Corradi, W. J. B., Alencar, S. H. P., et al. 2003, AJ, 126, 2971

Wahhaj, Z., Cieza, L., Koerner, D. W., et al. 2010, ApJ, 724, 835

White, R. J., & Basri, G. 2003, ApJ, 582, 1109

Williams, J. P., & Cieza, L. A. 2011, ARA&A, 49, 67

Wright, E. L., Eisenhardt, P. R. M., Mainzer, A. K., et al. 2010, AJ, 140, 1868

Wright, N. J., Newton, E. R., Williams, P. K. G., Drake, J. J., & Yadav, R. K. 2018, MNRAS, 479, 2351

Wu, C.-J., Wu, H., Lam, M.-I., et al. 2013, ApJS, 208, 29

Wyatt, M. C. 2008, ARA&A, 46, 339

Wyatt, M. C., & Jackson, A. P. 2016, Space Sci. Rev., 205, 231

Zuckerman, B. 2015, ApJ, 798, 86

Zuckerman, B., Melis, C., Rhee, J. H., Schneider, A., & Song, I. 2012, ApJ, 752, 58

Zuckerman, B., Rhee, J. H., Song, I., & Bessell, M. S. 2011, ApJ, 732, 61

Zuckerman, B., & Song, I. 2004, ARA&A, 42, 685

Appendix to "Follow-Up Imaging of Disk Candidates from the Disk Detective Citizen Science Project: New Discoveries and False-Positives in WISE Circumstellar Disk Surveys"

A.1 Changes to the Website Classification Scheme after Paper 1

Since Paper 1, we have made two key changes to the website classification setup; we changed the scheme for retiring subjects, and we corrected the online photometry to account for saturation effects at W1 and W2.

A.1.1 New Retirement Scheme

Visitors to the diskdetective.org site ("users") view "flipbooks" showing several images of the same source at different wavelengths. After they view the flipbooks, users answer a question, "What best describes the object you see?", by clicking on one or more of six buttons, labeled "Multiple objects in the Red Circle", "Object Moves off the Crosshairs", "Extended beyond circle in WISE Images" "Empty Circle in WISE images", "Not Round in DSS2 or 2MASS images" and "None of the Above/Good Candidate". With the exception of the "None of the Above" option, the user can choose more than one description per flipbook. After at least one of these classification buttons is chosen, a button labeled "Finish" becomes active; clicking this button records the user's choices and causes the next flipbook to appear.

To utilize this classification data requires a "retirement scheme," a set of rules for deciding when a given subject has received enough classifications that we can be reasonably sure of whether or not it is a good candidates. Prior to July 23, 2015, we used a very simple retirement scheme; we retired all subjects after 15 classifications. However, we realized that certain kinds of sources did not require so many independent classifications to make a confident decision about their nature. So on July 23, 2015, we put in place a new retirement scheme that allows us to progress more rapidly through the data.

To develop this new scheme, we experimented with several possible retirement rules by applying them to a set of subjects that already had fifteen classifications, to see if they would alter the final classification. We found that users were especially reliable at classifications as "Multiple objects in the Red Circle", or "Not Round in DSS2 or 2MASS images". Even if we used only the first five classifications of subjects in these categories, it did not change their ultimate classification. So we chose to implement a retirement rule that retires the subjects as either "Multiple objects..." or "Not Round..." when four out of the first five classifications are either "multi" or "oval" respectively. From the first year of classifications we know that almost 45% of our sources fit in one of these two categories. So we expected a substantial increase in efficiency from this rule, and indeed, though the number of active participants in the project remained stable roughly since July 2014, we have seen a noticeable increase in the retirement rate since implementing the new rule, so that 26% of our 278,121 subjects have now been retired.

A.1.2 Removal of WISE 1 Dropouts

A second improvement we made to the website was that we removed a list of problematic subjects from the online classification process. As Patel et al. (2014) and others have noted, bright sources can saturate the WISE detectors, causing systematic errors in the WISE photometry. These errors are worse at the WISE W1 and W2 bands. Since we chose objects for our input catalog using [W1]-[W4] colors, these photometric errors caused us to include some objects in our input catalog that had no true excess at W4 (22μm), only false deficits at W1. Using the saturation corrections in Patel et al. (2014), we found a list of 279 subjects that had been included in our search incorrectly because of saturation errors in their W1 photometry. On August 3, 2015, we removed these sources from the vetting process.

A.2 Deriving Brightness Thresholds for Contaminants

In this section, we derive a minimum brightness for background objects to produce a false positive excess detection in our system. We also show how these brightnesses propagate to the i, Y and H bands we use in our follow-up observations.

A.2.1 Minimum Contaminant Brightness in W4

Let us suppose that we have a target star with *no* circumstellar dust, whose spectrum is accurately approximated by the Rayleigh-Jeans law in the WISE bands. We will denote this target star's intrinsic magnitudes as m_t, and its intrinsic flux as $f_{m,t}$. Let us also suppose a background contaminant whose intrinsic magnitudes will be denoted m_c and whose flux will be denoted $f_{m,c}$. This background contaminant lies substantially inside the W4 PSF half-width at half-maximum,

such that the observed W4 magnitude $[W4]_{obs}$ is the magnitude of the combined light from the target and contaminant:

$$f_{W4,obs} = f_{W4,t} + f_{W4,c}, \tag{A1}$$

but outside the W1 PSF HWHM, such that $[W1]_{obs} = [W1]_t$.

Assuming that our target star has $[W1_t] - [W4_t] = 0$, we wish to know the minimum brightness $W4_c$ such that $[W1_{obs}] - [W4_{obs}] \geq 0.25$.

Making substitutions suggested by the above equalities, we have

$$W4_t - W4_{obs} \geq 0.25,$$

Using the equation for flux/magnitude conversion, this becomes

$$f_{W4,c} \geq 0.258925 f_{W4,t}. \tag{A2}$$

Converting this back into magnitude differences, we have

$$W4_c - W4_t \leq 1.467 \tag{A3}$$

We thus show that contaminants more than ~ 1.5 magnitudes dimmer than the target star in W4 will not produce a significant enough excess for the star to become a false positive entry in the Disk Detective Input Catalog. As such, with the greater depth probed by high-resolution imaging, we must quantitatively assess whether a detected background contaminant will produce a false positive, rather than qualitatively assessing it, as was done with the Web site-based classifications. (Binks, 2016)

Table A.1. W4 Colors of Selected Background Object Types

Characteristics	Colors $i - W4$	$Y_C - W4$	$H_C - W4$
M dwarf: $T_{\rm eff} = 3300{\rm K}, \log(g) = 5.0$	3.545	1.896	0.801
Class I YSO: $\lambda f_\lambda \sim \lambda^0$	2.94	2.05	1.82
ULIRG: $\lambda f_\lambda \sim \lambda^2$	10.25	8.67	7.48

A.2.2 Applying the Minimum Brightness to the i, Y, and H Bands

To determine if a potential background object is bright enough to produce a false positive excess in W4, we must know the difference in magnitude between such a contaminant and the target in the bands in which we conducted high-resolution follow-up observations. We assume for this exercise that the target's optical and near-IR SED is approximately identical to an idealized Vega—i.e. it is of zeroth magnitude in all bands. This sets the contaminating magnitude limit of 1.467. Below, we give examples of three typical contaminants, each with a W4 magnitude of 1.467: a background M dwarf and two different power-law spectra. Table A.1 lists the i, Y, and H magnitudes for these objects.

False Positive due to a Background M dwarf

The initial mass function of the neighborhood peaks at a spectral type of M2-M3.5, which corresponds to a stellar effective temperature of $T_{\rm eff} \simeq 3250 - 3400$ K. Accordingly, we select a model M dwarf atmosphere with $T_{\rm eff} = 3300$ K and $\log(g) = 5.0$ from the BT-Settl package of model atmospheres (Baraffe et al., 2015) as our contaminating M dwarf. The BT-Settl models have pre-computed magnitudes for many filter systems, which we use here to compute colors. This

model has a [H]-[W4] value of 0.801, corresponding to an H band contaminant delta-magnitude of 2.268 magnitudes. The [i]-[W4] value for this model is 3.545 magnitudes, yielding a magnitude difference in Robo-AO data of 5.012 magnitudes.

False Positive due to Background Sources with Power Law Spectra

Some objects are reasonably represented with a power-law spectrum $\lambda f_\lambda \sim \lambda^\alpha$. For these objects, colors can to first order be approximated as

$$[m_{\lambda_1}] - [m_{\lambda_2}] \sim 2.5 \log_{10} \left(\frac{f_{0,\lambda_1}}{f_{0,\lambda_2}} \right) - 2.5(\alpha - 1) \log_{10} \frac{\lambda_1}{\lambda_2}.$$

For the colors of interest in this paper, this corresponds to:

$$[\mathrm{H}] - [\mathrm{W4}] \sim 1.817 + 2.831\alpha,$$

$$[\mathrm{Y}] - [\mathrm{W4}] \sim 2.048 + 3.313\alpha,$$

and

$$[i] - [\mathrm{W4}] \sim 2.940 + 3.654\alpha.$$

Young stellar objects are defined by the value of α—a Class I YSO has slope $\alpha = 0$ (Lada, 1987; Kenyon & Hartmann, 1995); this spectrum also roughly approximates a heavily-reddened early-type star. If such an object were in the background of our images and bright enough to produce a false-positive, the delta-magnitude in the H band would be 3.284 and the Y band delta-magnitude would be 3.515. These could both likely be detected in our images. The i-band delta-magnitude would be 4.407, also likely detectable.

Also of interest is the case where $\alpha = 2$. This roughly corresponds to the SED of a luminous or ultra-luminous infrared galaxy, or (U)LIRG, which has an AGN component (Vega et al., 2008). In this case, however, the H-band delta-magnitude would be 8.946 and the Y-band delta-magnitude would be 10.141, while the i-band delta-magnitude would be 11.715. These are all clearly undetectable in our follow-up image data, and are thus treated instead with the prescription of Papovich et al. (2004) in Section 2.5.2.

A.3 Comments on Selected Disk Candidates

Below are brief comments on selected disk candidates presented in Section 2.7. Having noted previous identifications as disk candidates in Section 2.7, we primarily discuss characteristics of the subject's appearance, either in the images used on the Disk Detective website, or in the follow-up images.

- **J021327.01+421923.3** This system, which was previously identified by Cotten & Song (2016); McDonald et al. (2017), exhibits slight extension in the W4 image.

- **J023720.84+395345.8** This system is a known spectroscopic binary (Hube, 1981). The companion, an early-G main sequence star based on the binary mass function, has a projected angular separation of $<< 1''$, making it undetectable as a separate component in follow-up data. The SED indicates no significant effect on the 22 micron excess.

- **J025926.83+593531.6** We recover this system, a spectroscopic binary (Abt, 2009) which was previously identified as a source in the W5 region by Koenig et al. (2008). The secondary component has a minimum mass of 1.7326 $R_\odot$ based on the binary mass function, suggesting a possible A7V

star. The projected angular separation is $<< 1''$, making it undetectable as a separate component in follow-up data. The SED indicates no significant effect on the 22 micron excess.

- **J030854.20-185809.1** This system, a known A0V system, is best fit as a two-stellar-component system with a K dwarf component, as well as a 349 K disk. Further observation is necessary to confirm this additional component.

- **J034400.28+243324.6** This δ Scuti variable, which appears in Cotten & Song (2016); McDonald et al. (2017), exhibits slight extension at W4.

- **J041517.47+505124.0** This system, which appears in Marton et al. (2016), has been identified as a Be star previously (Merrill & Burwell, 1943) and more recently as having H-alpha in emission (Kohoutek & Wehmeyer, 1999). Further spectroscopic follow-up is necessary to determine the nature of this emission (i.e. whether the target is a classical Be star, rather than a debris disk host).

- **J043521.12-081730.0** This object exhibits slight extension at W4.

- **J051143.75+122012.5** This system exhibits slight extension at W4.

- **J051328.63-043910.6** This object is a component of a binary system. Its companion is $35''$ away from the source, too distant to affect the observed excess.

- **J052331.01-010423.6** This star exhibits eclipses from circumstellar material, per Osborn et al. (2017).

- **J053707.15+603636.4** This object, which appears in Cotten & Song (2016) exhibits slight extension at W4.

- **J054330.38+251724.4** This system has previously been identified as an H-alpha emitter (Kohoutek & Wehmeyer, 1999). Further spectroscopic follow-up is necessary to determine the nature of this emission.

- **J054733.26+521144.5** This system has previously been identified as an H-alpha emitter (Merrill & Burwell, 1950). Further spectroscopic follow-up is necessary to determine the nature of this emission.

- **J111714.49-594610.8** This target is a member of the Lower Centaurus Crux (LCC) of the Sco-Cen OB2 association, per Hoogerwerf (2000). Testing its kinematics with BANYAN Σ yields a 44.9% membership probability in LCC, and a 40.5% membership probability in Carina.

- **J111925.92-301922.9 and J165204.85+145827.2** We report the first detection of a disk around the α^2 CVn variable AWI0005cwg. We also note that AWI00004o8, identified in Paper 1, is also an α^2 CVn variable.

- **J114336.83-802900.5** This target exhibits slight extension at W4.

- **J132026.77-491325.4** This target is a known disk-hosting member of Sco-Cen (Chen et al., 2012). Re-evaluation with BANYAN Σ yields an 88.7% probability of membership in LCC.

- **J134909.18-541342.3** This target is a known disk-hosting member of Sco-Cen (Chen et al., 2012). Re-evaluation with BANYAN Σ yields a 42.1% membership probability in LCC, and a 49.5% membership probability in Upper Centaurus-Lepus (UCL).

- **J144458.63-280251.9** This target is a known multiple system (Horch et al., 2011) with an excess first detected by Cruz-Saenz de Miera et al. (2014). We do not resolve both components of the binary system.

- **J173254.69+404312.3** This target exhibits very slight extension at W4.
- **J173832.90+425112.9** This target is a known Cepheid variable.
- **J183311.41+025439.0** This object shows a faint background object in DSS2 survey data that does not appear in Robo-AO observations.
- **J185211.39+102422.6** This object shows a faint background object in DSS2 survey data that does not appear in Robo-AO observations.
- **J190901.24+110641.3** This target exhibits Hα in emission (Kohoutek & Wehmeyer, 1999).
- **J192136.46+220744.7** This object shows a faint background object in DSS2 survey data that does not appear in Robo-AO observations.
- **J192437.52+563454.9** This object shows a very faint background object in DSS2 survey data, which does not appear in the Robo-AO data for the system.
- **J210144.07+521717.6** This object is an emission-line star (Kohoutek & Wehmeyer, 1999).
- **J212952.96+525601.9** This object exhibits a slight asymmetrical extension at W4.
- **J215947.70-593411.9** This target is a known δ Scuti variable (Rodríguez et al., 2000).
- **J230112.67-585821.9** We note slight extension at W4.